Assessment of Fluidic Control Effectors using Computational Fluid Dynamics

Thesis submitted in accordance with the requirements of
the University of Liverpool for the degree of Doctor in Philosophy
by
George Hoholis

April 2016

Abstract

The work discussed in this thesis uses computational fluid dynamics to evaluate the performance of circulation control as a control effector for manoeuvring aircraft. As an outcome of this work, it has been shown that circulation control could potentially replace conventional control surfaces as a manoeuvre effector. Two test cases were simulated to validate the computational fluid dynamics solver used throughout this work. The first, a circulation control aerofoil, which demonstrated that the solver was capable of predicting the pressure distribution over the aerofoil surface and the boundary layer velocities near the slot. The level of grid refinement and the choice of turbulence model were also investigated showing that the results depended significantly on the model used. The second, a generic unmanned combat air vehicle which exhibits highly nonlinear flow topologies at high angles of attack. The integrated loads were well predicted while the flow remained attached. There were some discrepancies in the loads at higher angles of attack due to the unsteady nature of the flow however the overall flow topology was captured accurately throughout the angle of attack range of zero to twenty five degrees. This demonstrated that the vortical flow encountered by typical combat aircraft can be predicted.

Modifications were then made to the generic unmanned combat air vehicle used as a test case. The conventional control surfaces were replaced by circulation control and the performance of two operations was investigated. The two operations are, one for generating a rolling moment and the other for generating a yawing moment. The yawing moment operation was able to perform independently of the angle of attack, whilst the performance of the rolling moment operation dropped off significantly when trailing edge flow separation occurred. Two configurations were tested, one with a single slot and one with three

slots along the span. A increase in efficiency for the rolling moment operation was demonstrated by using multiple slots with a gap in between each.

A tabular model for a two dimensional aerofoil employing circulation control was constructed to investigate whether these types of models are suitable for predicting unsteady loads. All loads are expressed as combinations of functions depending on a selection of the input parameters, i.e. angle of attack. The effects of decoupling the input parameters from each other were investigated. At high angles the performance of the circulation control decreases. The stall angle also decreases as there is an increase in the control parameter for the circulation control. As a result of this, these two parameters must be coupled within the model to obtain accurate predictions of the integrated loads. Overall, the lift and pitching moment were predicted accurately with some hysteresis. The drag was over and underpredicted during rapid changes of the control parameter and there was a significant amount of hysteresis observed. A discussion of how a tabular model may be constructed for a full aircraft employing circulation control was also conducted.

Acknowledgements

I would like to acknowledge my supervisors Prof. Ken J. Badcock and Dr. Rene Steijl for all of their support. I would like express my apprecation to Dr. David Kennett, Dr. Vasileios Pastrikakis, Mr. Simone Colonia and the rest of the members of the Computational Fluid Dynamics Laboratory for useful discussions and for creating a pleasurable work environment. I am grateful for the funding provided by the Engineering and Physical Sciences Research Council (EPSRC) and BAE Systems which has made it possible for this work to be done. I would like to thank Dr. Gregory S. Jones and Mr. Keith B. Paschal for access to the wind tunnel results relating to the circulation control aerofoil, CC-E0020EJ. I would also like to thank all the members of the AVT-201 group for all the data and wind tunnel results relating to the SACCON.

Declaration

I confirm that the thesis is my own work, that I have not presented anyone else's work as my own and that full and appropriate acknowledgement has been given where reference has been made to the work of others.

George Hoholis

December 2015

List of Publications

Hoholis, GA, Steijl, R and Badcock, KJ, "The Application of Trailing Edge Circulation Control as a Roll Effector for Unmanned Combat Aerial Vehicles," *Advanced Aero Concepts, Design and Operations - Applied Aerodynamics Conference 2014, Royal Aeronautical Society, Bristol, United Kingdom*, 18-20 June, 2014

Hoholis, GA, Steijl, R and Badcock, KJ, "Circulation Control as a Roll Effector for Unmanned Combat Aerial Vehicles," *Accepted for publication by AIAA Journal of Aircraft*

Kennett, DJ, Hoholis, GA and Badcock, KJ, "Numerical Simulation of Control Surface Deflections over a Generic UCAV Configuration at Off-design Flow Conditions," *32nd AIAA Applied Aerodynamics Conference, 2014, Atlanta, Georgia*, 16-20 June, 2014

Kennett, DJ, Hoholis, GA and Badcock, KJ, "Numerical Simulation of Control Surface Deflections over a Generic UCAV Configuration at Off-design Flow Conditions," *NATO STO AVT-201 Report, Chapter 9, 2015*

Table of Contents

Abstract iii

Acknowledgements v

Declaration vii

List of Publications ix

List of Figures xv

List of Tables xx

List of Symbols xxiii

1 Introduction 1

1.1 Fluid Processes 2

1.1.1 Coanda Effect 2

1.2 Fluidic Thrust Vectoring 4

1.2.1 The Throat Shifting Method 4

1.2.2 The Shock Vector Control Method 5

1.2.3 The Counterflow Method 6

1.2.4 The Coflow Method 7

1.2.5 Complete Aircraft Configurations 8
1.3 Circulation Control 10
1.3.1 Early Research and Demonstrator Aircraft 10
1.3.2 Recent Concepts and use of CC as Manouevre Effectors 10
1.3.3 CFD Simulation 13
1.3.4 CC Applied to Swept Wings 15

2 Mathematical Formulation **17**

2.1 Reynolds Averaged Navier-Stokes Equations 17
2.1.1 Navier-Stokes Equations 17
2.1.2 Vector Form of Navier-Stokes Equations 19
2.1.3 Reynolds Averaging 20
2.2 Turbulence Modelling 21
2.2.1 Wilcox k-ω Model 21
2.2.2 Vortex Correction 22
2.2.3 Menter's SST 23
2.3 Numerical Method 25
2.3.1 Curvilinear Form 25
2.3.2 Steady State Solutions 26
2.3.3 Unsteady Simulations 27
2.4 Reservoir Boundary Condition 27
2.5 Unsteady Control of the Coanda Jet 28

3 Validation Test Cases **31**

3.1 Coanda Jet CFD Validation 31
3.1.1 Geometry and Wind Tunnel Details 31

3.1.2 Geometry Smoothing . . . 33
3.1.3 Grids and Computational Setup . . . 34
3.1.4 Flowfield Description . . . 35
3.1.5 Validation Data Comparisons . . . 37
3.1.6 Other Simulation Results . . . 40
3.1.7 Coanda Jet Validation Summary . . . 45
3.2 UCAV Validation Test Case . . . 48
3.2.1 Treatment of the Control Surfaces . . . 49
3.2.2 Grids and Computational Setup . . . 50
3.2.3 Results . . . 52
3.2.4 UCAV Validation Summary . . . 56

4 SACCON with Circulation Control **59**

4.1 2D Analysis in Preparation for CC Modifications . . . 60
4.2 Grids and Computational Setup . . . 60
4.3 Results . . . 62
4.4 Steady State Simulations Summary . . . 66
4.5 Unsteady Simulations and Dynamic Behaviour . . . 67
4.6 Unsteady Results . . . 68
4.6.1 Indicial Response . . . 69
4.6.2 Hysteresis . . . 71
4.6.3 Jet Separation . . . 74
4.6.4 Unsteady Simulation Summary . . . 76
4.7 SACCON with Circulation Control . . . 77
4.7.1 Grid and Computational Setup . . . 79

4.8 Results . . . 80
4.8.1 Yawing Moment Operation . . . 81
4.8.2 Rolling Moment Operation . . . 85
4.8.3 Comparison against Conventional Control Surfaces . . . 91
4.8.4 3-slot Configuration . . . 95
4.9 Summary and Conclusions . . . 98

5 Reduced Order Modelling: Tabular Method **101**
5.1 Circulation Control Aerofoil . . . 103
5.1.1 Sample Placement for the Nozzle Pressure Ratio Parameter . . . 104
5.1.2 Decoupling Nozzle Pressure Ratio from Angle of Attack . . . 106
5.1.3 Inclusion of Stability Derivatives . . . 109
5.2 Summary and Conclusions . . . 111
5.3 Tabular Method for the SACCON with CC . . . 112

6 Conclusions **115**

Bibliography **126**

List of Figures

1.1 Diagrams demonstrating the Coanda effect from the patent [2]. 3

1.2 Diagram of a fluidic thrust vectoring nozzle using a throat shifting method from [4]. . . . 5

1.3 Diagram of a fluidic thrust vectoring nozzle using the shock vector control method from [3]. 6

1.4 Diagram of a fluidic thrust vectoring nozzle using the counterflow method from [3]. 7

1.5 Diagram of setup used to investigate coflow fluidic thrust vectoring from [15]. 7

1.6 Diagram of a water tunnel setup used for experimental investigations from [18]. 9

1.7 The WVU CC technology demonstrator [24]. 11

1.8 The GACC wing [26]. 11

1.9 Diagram of Java planform with the CC devices and the conventional control surfaces [30]. 12

1.10 Test wing with the CC device installed and a close up of the device [29]. 13

1.11 Cross sectional geometry of the NCCR 1510-7067N [32]. 14

1.12 Streamlines on mach contours for a circulation control aerofoil using SA turbulence model [34]. 15

1.13 Diagram of the wind tunnel geometry from [38]. 16

2.1 Flow chart demonstrating the process used to control the jets during unsteady simulations. 29

3.1 Diagram and picture of the wind tunnel geometry from [35]. 32

3.2 Geometry smoothing process. 33

3.3 The finest grid used for the CC-EE0020EJ with close-ups of some key locations. 35

3.4 Plots of the flowfield for the CC-E0020EJ with the jet on. 36
3.5 Comparison of the C_p over the surface and the C_L for the grid refinement study. 37
3.6 Comparison of C_p from the CFD calculations and the experimental results. 39
3.8 Comparison of boundary layer velocites from the CFD calculations and the experimental results for $C_\mu =$ 0.047. 42
3.9 Comparison of boundary layer velocites from the CFD calculations and the experimental results for $C_\mu =$ 0.115. 43
3.10 Lift coefficient vs C_μ and NPR with close-ups of the slot with Mach contours at two points of interest. 44
3.11 C_L vs. α for different C_μ. 45
3.12 Velocity profiles at various points along the coanda surface for NPR=1.22330. 46
3.13 Diagrams of the SACCON planform indicating the reference lengths, location of pressure taps and control surfaces Ref. [45]. 48
3.14 Screenshot of the region between the wing (grey) and flap (blue) used as a blending region(red). 49
3.15 Grid topology at key locations for the SACCON. 51
3.16 Iso-surfaces of the λ_2 criterion coloured with C_p for the SACCON at various angles of attack. 53
3.17 Comparison of the computational and experimental integrated loads for the SACCON. . . 54
3.18 Comparison of the computational and experimental integrated loads for the SACCON. . . 55

4.1 CC modifications(red) and the blended flap(blue) for the 2D aerofoil section from the root of the wing with a close up of the trailing edge. 61
4.2 Plot showing the grid used for the aerofoil taken from the root of the SACCON's wing with close-ups of the trailing edge for both the modified and unmodified aerofoil. 62
4.3 Lift coefficient for the CC aerofoil at a range of NPR. 63

4.4 Comparison of the aerodynamic coefficients against angle of attack for the various aerofoils. 64

4.5 Comparison of the flowfield at the leading and trailing edges of the aerofoil for the blended flap and CC at various angles of attack. 65

4.6 Unsteady coanda jet at NPR=1.5 with the plenum chamber at freestream pressure at T=0. 69

4.7 Oscillations of the control parameters at a reduced frequency of 0.0314. 70

4.8 Oscillations of the control parameter at a reduced frequency of 0.1571. 71

4.9 Flowfield plots demonstrating the jet separation due to NPR oscillations. 72

4.10 Cases involving oscillations in the NPR for two NPR ranges and two reduced frequencies. 73

4.11 Flowfield plots demonstrating the jet separation due to AoA oscillations. 74

4.12 Cases involving oscillations in the AoA with a constant NPR of 1.5. 75

4.13 Screenshots of two key locations of the SACCON's trailing edge to show the modifications made for the CC device. 77

4.14 Screenshots of the full CAD model of the SACCON before and after the modifications. . . 78

4.15 The surface grid for the SACCON employing CC. The left half corresponds to the 3-slot configuration and the right half corresponds to the single slot configuration. 79

4.16 Yawing moment against NPR and C_μ for the SACCON with CC determined using CFD. 81

4.17 Drag coefficient vs. C_μ for the SACCON with CC determined using CFD. 82

4.18 Iso-surfaces of the λ_2 criterion coloured with C_p for the SACCON with CC using the upper and lower slots on the right wing at a NPR of 1.4 and 3. 83

4.19 Yawing moment vs. α and Yawing moment vs. β for the SACCON at various conditions. 84

4.20 Rolling moment and efficiency for the SACCON with CC at 0°. 85

4.21 3D view of the right wing with rectangles indicating where the subsequent close ups are. . 86

4.22 3D view at the root of the wing of the jet exiting the slot. 87

4.23 The slice is coloured using X-vorticity contours and the regions enclosed by black lines are regions identified as vortices by the λ_2 criterion. The surfaces in the 3D view are coloured using C_P contours and the streamtraces are coloured with X vorticity. 87
4.24 The slice is coloured using X-vorticity contours and the regions enclosed by black lines are regions identified as vortices by the λ_2 criterion. The surfaces in the 3D view are coloured using C_P contours and the streamtraces are coloured with X vorticity. 88
4.25 The slice is coloured using X-vorticity contours and the regions enclosed by black lines are regions identified as vortices by the λ_2 criterion. The surfaces in the 3D view are coloured using C_P contours and the streamtraces are coloured with X vorticity. 89
4.26 Iso-surfaces of the λ_2 criterion coloured with C_p for the SACCON with CC using the upper slot on the right wing and lower slot on the left wing at a range of NPRs. 90
4.27 Plot showing the contribution to the roll moment for a NPR of 1.2 and 1.6 for the case with the single slot CC. 91
4.28 Comparison of the loads from the experiments with LOB/LIB at $-20°$ and ROB/RIB at $20°$, the integrated loads from the CFD results with the same flap settings and the integrated loads from the CFD result of the SACCON with CC at a NPR of 1.20. 92
4.29 Comparison of the loads from the experiments with LOB/LIB at $-20°$ and ROB/RIB at $20°$, the integrated loads from the CFD results with the same flap settings and the integrated loads from the CFD result of the SACCON with CC at a NPR of 1.20. 93
4.30 Plot showing the contribution to the roll moment for a NPR of 1.2 for the case with the single slot CC. 94
4.31 Iso-surfaces of the λ_2 criterion coloured with C_p for the SACCON with CC using the upper slot on the right wing and the lower slot on the left wing at a NPR of 1.2. 95
4.32 Plot showing the contribution to the roll moment for $0°$ and $15°$ for the case with conventional control surfaces. 96

4.33 Iso-surfaces of the λ_2 criterion coloured with C_p for the SACCON with CC using the upper IB/OB slots on the right wing and the lower IB/OB slots on the left wing at a NPR of 1.2. 97

4.34 Plot showing the contribution to the roll moment for a NPR of 1.2 for the case with three slot CC. 98

5.1 Indicial response for an anlge of attack of 5° for the modified aerofoil from the root of the SACCON's wing with the jet turned off. 104

5.2 Lift coefficient vs. NPR interpolated using kriging for different numbers of points. 105

5.3 The aerodynamic coefficients and the damping derivatives at a Mach Number of 0.2. The points correspond to the discrete entries determined using CFD. 107

5.4 Comparison of the aerodynamic loads predicted by CFD and by tabular methods for sinusoidal oscillations of the AoA between 0° and 10° at a reduced frequency of 0.052 with a NPR of 1.5. 108

5.5 The aerodynamic coefficients and the damping derivatives at a Mach Number of 0.2. The points correspond to the discrete entries determined using CFD. 109

5.6 Comparison of the aerodynamic loads predicted by CFD and by tabular methods for sinusoidal oscillations of the NPR between 1.3 and 1.7 at a reduced frequency of 0.157 and sinusoidal oscillations of the AoA between between 0° and 10° at a reduced frequency of 0.052. 110

List of Tables

1.1 Turbulence models used by various papers. 15

3.1 Experimental results available from [36]. 33

3.2 Grids used for the refinement study to ensure grid-independent solutions. 34

3.3 Details of the Mach and Reynolds numbers for the wind tunnel experiments [36]. 36

3.4 Integrated loads from the CFD results. 38

4.1 Dynamic cases $\left(T = \frac{u_\infty t}{c}\right)$. 68

List of Symbols

a	Speed of sound
c	Chord length
c_{ref}	Reference chord
C_D	Drag coefficient
$CD_{k\omega}$	Constant for SST turbulence model
$C_{fg,sys}$	Thrust efficiency
C_l	Rolling moment coefficient
C_L	Lift coefficient
C_m	Pitching moment coefficient
C_n	Yawing moment coefficient
C_p	Pressure coefficient
C_z	Thrust vector coefficient
C_μ	Blowing coefficient
$\mathbf{C}_\mu$	Vector of blowing coefficient
d	Distance from field point to nearest wall
e	Specific energy
E	Total energy
F_1,F_2	Blending functions for SST turbulence model
$F_{i,p}$	Ideal isentropic thrust of primary flow
$F_{i,s}$	Ideal isentropic thrust of secondary flow
F_r	Nozzle resultant thrust
$F_{y,tv}$	Thrust vector force
$\mathbf{F}^i$,$\mathbf{G}^i$,$\mathbf{H}^i$	Inviscid flux vectors
$\mathbf{F}^v$,$\mathbf{G}^v$,$\mathbf{H}^v$	Viscous flux vectors
gc	Geometric centre of the upper and lower slots on the SACCON's wings
H	Total enthalpy
$\hat{\mathbf{j}}$	Unit vector in the y-direction
J	Jacobian determinant
k	turbulent kinetic energy per unit mass
$\hat{k}$	Thermal conductivity
L^*	Characteristic lengthscale
$\dot{m}_j$	Massflow of coanda jet
M_∞	Freestream Mach number
MRP	Vector of moment reference point for the SACCON
n	Number of discrete entries used for tabular models

p	Pressure
p_j	Pressure at the slot exit of the coanda jet
P_k	Production term for k
P_r	Prandtl number
P_rt	Turbulent Prandtl number
P_ω	Production term for ω
$\dot{q}$	Rate of volumetric heat addition per unit mass
q_i	Heat flux in $i = x, y, z$ directions
q_∞	Dynamic freestream pressure
r	Polar coordinate for coanda surface
R	Ratio of magnitude of mean strain-rate tensor to magnitude of mean rotation tensor
Re	Reynolds number
$\mathbf{R}\left(\mathbf{W}_{i,j,k}\right)$	Flux residuals
S	Mean strain-rate tensor
S	Wing area
t	Real time
T	Non-dimensional time
T	Temperature
T_t, j	Total temperature of coanda jet
u,v,w	Velocity components in x,y and z directions
u_j	Velocity of coanda jet
u_∞	Freestream velocity
$\bar{u}$,$\bar{v}$,$\bar{w}$	Mean velocity components in x,y and z directions
$u^{'}$,$v^{'}$,$w^{'}$	Velocity fluctuations in x,y and z directions
$\mathbf{U}$	Flow velocity vector
$V_{i,j,k}$	Cell volume
$w^{'}$	Velocity fluctuations in z direction
w_p	Massflow of primary flow
w_s	Massflow of secondary flow
$\mathbf{W}$	Vector of conserved variables

Greek Symbols

α	Angle of attack
α_1	Constant for turbulence models
β	Sideslip angle
β_1,β_2, β^*	Constants for turbulence models
γ	Specific heat ratio
γ_1,γ_2	Constantts for turbulence models
δ	Deflection angle
$\delta_{e,a,r}$	Deflection angle for elevon, aileron and rudder respectively
δ_{ij}	Kronecker delta
ζ,η,ξ	Curvilinear coordinates
η	Thrust vectoring efficiency
θ	Polar coordinate for coanda surface
κ	Constant for turbulence model
λ_2	Criterion used to identify vortical structures within flowfield
ρ	Density
σ_1,σ_2,σ_3,σ_{k1},σ_{k2},$\sigma_{\omega 1}$,$\sigma_{\omega 2}$	Constants for turbulence models
τ	Pseudo-time
τ_{ij}	Components of stress tensor $i, j = x, y, z$
μ	Laminar viscosity
μ_t	Turbulent eddy viscosity
ν	Kinematic viscosity
ν_t	Turbulent kinematic viscosity
ϕ,ϕ_1,ϕ_2	Representation of constants within blending function
ω	Specific dissipation rate
Ω	Mean rotation tensor

Acronyms

AoA	Angle of Attack
AVT	Applied Vehicle Technology
BART	Basic Aerodynamics Research Tunnel
CAD	Computer-Aided Design
CC	Circulation Control
CFD	Computational Fluid Dynamics
DACE	Design and Analysis of Computer Experiments
DLR	German Aerospace Center
DNS	Direct Numerical Simulation
DNW	German-Dutch Wind Tunnels
FLAVIIR	Flapless Air Vehicle Integrated Industrial Research
FTV	Fluidic Thrust Vecotring
GACC	General Aviation Circulation Control
GTRI	Georgia Research Institute of Technology
IB	InBoard
LDV	Laser Doppler Velocimetry
LIB	Left InBoard flap
LOB	Left OutBoard flap
MB	MidBoard
MRP	Moment Reference Point
NASA	National Aeronautics and Space Administration
NATO	North Atlantic Treaty Organisation
NPR	Nozzle Pressure Ratio
OB	OutBoard
ONR	Office of Naval Research
PIV	Particle Image Velocimetry
PMB	Parallel Multi-Block
RANS	Reynolds-Averaged Navier-Stokes
RIB	Right InBoard flap
ROB	Right OutBoard flap
ROM	Reduced Order Model
SA	Spalart-Allmaras
SACCON	Stability and Control CONfiguration
SST	Shear Stress Transport
STOL	Short Take-Off and Landing
UAV	Unmanned Aerial Vehicle
UCAV	Unmanned Combat Aerial Vehicle
URANS	Unsteady Reynolds-Averaged Navier-Stokes
VTOL	Vertical Take-Off and Landing
WVU	West Virginia University

Chapter 1

Introduction

Fluidic controls are manoeuvre effectors which use a flow control technique such as secondary fluidic injections, suction and the coanda effect to generate lift and control moments. Mechanical thrust vectoring, which uses deflection surfaces to change the direction of the thrust, has been used successfully on a few aircraft, including the F-18 HARV [1] and the F-22 Raptor. These systems can be heavy and complex, requiring additional maintenance. Fighter aircraft are capable of flying at very high angles of attack and have greatly improved short take-off and landing (STOL) capabilities. Conventional control surfaces such as ailerons have been used for roll control on fixed-wing aircraft since the early twentieth century. These also require many moving parts and at high angles of attack become ineffective due to flow separation at the trailing edge of the wings. In comparison to this, fluidic devices do not need large moving parts, potentially require little maintenance and should be able to operate at high angles of attack. The lack of mechanically moving parts can potentially reduce the weight of a wing and also reduce the radar cross section of the aircraft. The fluidic controls that are considered in this thesis are fluidic thrust vectoring and circulation control. Fluidic thrust vectoring varies the direction of the thrust from a fixed-geometry nozzle using flow control techniques. There are various methods which have been investigated and these are discussed further in the following section. The circulation control is intended as a replacement for conventional control surfaces, providing both high lift for take off and landing and control moments for manoeuvres. There is a lot of interest in these devices for use on Unmanned Aerial

Vehicles (UAV) as they can help to reduce the radar cross section of an aircraft and potentially its weight.

The work undertaken in this thesis aims to evaluate and develop computational fluid dynamics (CFD) modelling techniques applied to complete aircraft configurations employing flow control devices. This is done by applying these devices to a UAV configuration and predicting the performance of the devices. Comparisons were made with results for a UAV using conventional control surfaces which have been validated against wind tunnel data to ensure the accurate prediction of typical flow features that are encountered by this type of vehicle. This thesis starts by describing previous research carried out on the fluidic devices that were used. This is followed by a description of the CFD solver that was used for the simulation of the devices and the aircraft configuration. Validation test cases were then simulated and the results compared to available wind tunnel data. These include two-dimensional cases with fluidic devices, and three-dimensional cases of a UAV configuration with ailerons and elevons to allow evaluation of the fluidic controls. Circulation control is then applied to a cross-section of the UAV that is used to determine the size of the fluidic device required to match the performance of the conventional control surfaces. This aerofoil section is also used to investigate the behaviour of the device during forced oscillations of the control parameters. The UAV configuration is then modified and fitted with the circulation control and its ability to generate roll and yaw moments is investigated. Control moments about the pitch axis are generated using thrust vectoring for these types of configurations. A tabular model was developed to predict the integrated loads for the aerofoil employing circulation control. This can be used to predict the trajectory of the aircraft through a variety of manoeuvres and the rates at which these manoeuvres can be performed.

1.1 Fluid Processes

1.1.1 Coanda Effect

The coanda effect is the tendency of a fluid jet to be attracted to a nearby surface. It was named after Henri Coandă who was the first person noted to have used it in an aerospace application [2]. A

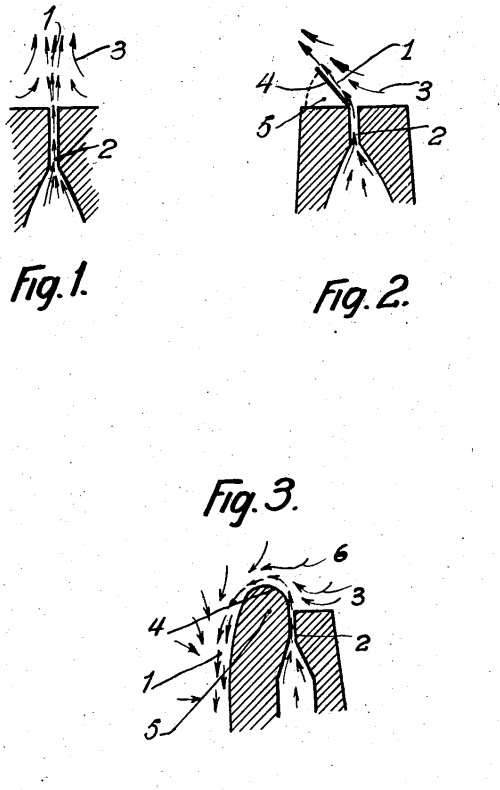

Figure 1.1: Diagrams demonstrating the Coanda effect from the patent [2].

diagram from the patent can be seen in Fig. 1.1. He observed that when injecting a sufficiently high speed fluid into another fluid a suction effect is produced at the point of injection. As a result of this the surrounding fluid is drawn in and entrained by the low pressure jet. By placing a surface on one side of the jet, an unbalancing effect is created which makes it more difficult for the jet to entrain the flow on the side of the surface. The jet is then deflected towards the surface. There have been investigations into the geometry of the surfaces used to determine appropriate shapes to prolong the jet attachment and the conditions under which jet attachment is achieved. The majority of the work was performed with specific applications in mind, leading to significant restrictions on the shapes and the conditions that were investigated. Some of the results are discussed in the following sections with a few of the relevant applications that make use of the coanda effect.

1.2 Fluidic Thrust Vectoring

There are several different types of fluidic thrust vectoring (FTV) that have been researched over the past few decades. A summary of the research conducted at NASA throughout the 1990's by Karen A. Deere [3] briefly discusses several of the concepts that have been tested experimentally and computationally. These concepts are split, according to how the thrust is vectored, into three main categories which are: shock vector control, throat shifting and counterflow. The two main parameters used to compare these methods are the thrust efficiency and the thrust-vectoring efficiency. The thrust efficiency is the resultant thrust of the nozzle divided by the sum of the ideal isentropic thrust of the primary and secondary flows, see equation 1.1. The thrust-vectoring efficiency is the deflection angle divided by the secondary mass flow as a percentage of the total mass flow, see equation 1.2.

$$C_{fg,sys} = \frac{F_r}{F_{i,p} + F_{i,s}} \tag{1.1}$$

$$\eta = \frac{\delta}{100\frac{w_s}{w_s+w_p}} \tag{1.2}$$

where $C_{fg,sys}$, F_r, $F_{i,p}$ and $F_{i,s}$ are the thrust efficiency, the resultant thrust, ideal isentropic thrust of the primary flow and ideal isentropic thrust of the secondary flow, respectively. η, δ, w_s and w_p are the thrust-vectoring efficiency, the deflection angle of the jet, the secondary massflow and the primary massflow, respectively.

1.2.1 The Throat Shifting Method

The throat shifting method uses a fluidic injection into the primary exhaust flow of the nozzle to skew the throat causing a deflection of the thrust, as illustrated in Fig. 1.2. The idea is that turning the jet before it becomes supersonic will increase the thrust efficiency. This concept has been tested both experimentally and computationally by Deere et al., Flamm et al. and Shin et al. [4–9]. The experiments

were done at the Jet-Exit Test Facility at NASA and the simulations were run using the PAB3D code.

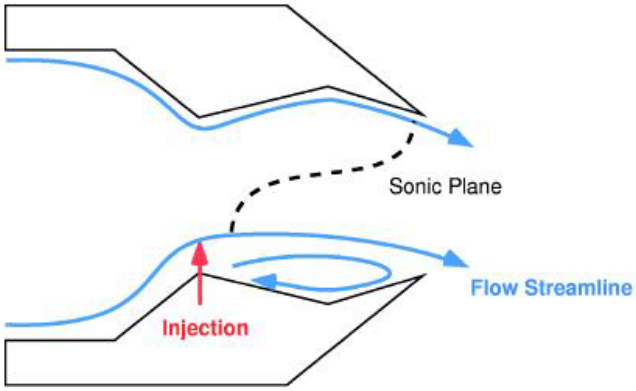

Figure 1.2: Diagram of a fluidic thrust vectoring nozzle using a throat shifting method from [4].

PAB3D was validated in [5] and shown to be able to predict the thrust-vector angle to within 0.3° at various secondary flow rates, and the thrust efficiency to within 2%. It was then used in [4, 6] to experiment with design parameters such as the injection angle and cavity convergence angle. Over 60 different variations of the nozzle were tested. Thrust efficiencies between 0.902 and 0.976 and thrust-vectoring efficiences of up to 3.7 degrees per percent of secondary mass flow were achieved. Further nozzle design and performance analysis was conducted in [7, 8]. These expanded on the range of design parameters tested to obtain a greater understanding of the parameter space and maximise the thrust efficiency and thrust-vectoring efficiency.

1.2.2 The Shock Vector Control Method

In the shock vector control method fluid is injected into the divergent part of the nozzle. This causes an oblique shock as the secondary flow obstructs the primary jet which is then turned, see Fig. 1.3. This method can produce large thrust-vector angles however there can be quite significant losses to the thrust efficiency as the flow goes through the shock.

An experimental investigation was conducted by Wing et al. [10], into the effects of the injection hole geometry and its location at a range of nozzle pressure ratios (NPR) and secondary injection mass

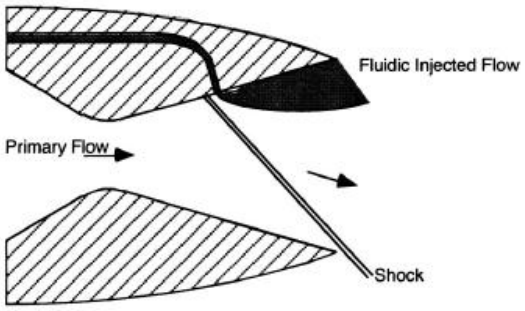

Figure 1.3: Diagram of a fluidic thrust vectoring nozzle using the shock vector control method from [3].

flow ratios. It was found that at overexpanded conditions the jet was vectored by up to 18°, whereas at the design NPR up to 13° of deflection was achieved. However the thrust efficiency was between 0.88 and 0.91 for the overexpanded jet and between 0.93 and 0.96 for the fully-expanded jet. Computational investigations of different nozzle geometries were performed by Mohammadi et al. and Deere [11, 12]. The first investigation looked at the aerodynamic effects on the thrust vectoring. It was found that the external flow reduced the effectiveness of the thrust vectoring by between 1.5° and 2.9°. The second investigation analysed the use of two injection slots and compared it to using only one injection slot. Using two secondary injections allowed them to achieve the same side force with less mass flow.

1.2.3 The Counterflow Method

In the counterflow method suction is applied at a slot adjacent to the primary exhaust flow which is surrounded by an aft collar. This creates a pressure drop near the collar which acts as a coanda surface vectoring the flow, see Fig. 1.4. Also, as this method does not use a secondary injection, it cannot be compared to the other methods using thrust-vectoring efficiency. There have been a few experimental and computational investigations of this method by Flamm and Hunter et al. [13, 14].

The experiments by Flamm [13] investigated three variations of the collar geometry, a range of NPR's from 3.5 to 10 and the suction slot height. The computational results from Hunter et al. [14] showed good agreement with the experiments at low suction, however there were differences in the attachment

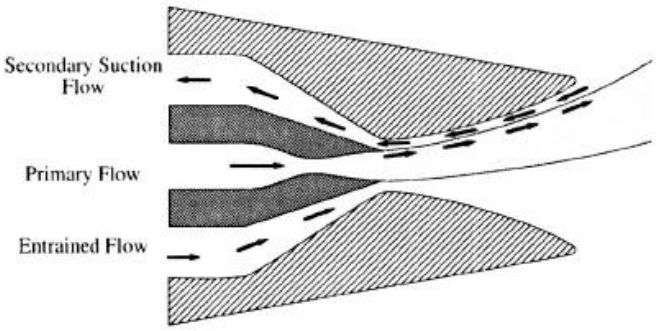

Figure 1.4: Diagram of a fluidic thrust vectoring nozzle using the counterflow method from [3].

behaviour of the exhaust flow. This method achieved thrust efficiencies of approximately 0.95 at almost all suction levels and vector angles up to 27.4°. Another observation that was made was that a counterflowing shear layer was not required for thrust-vectoring, certain parameters resulted in a co-flowing shear layer.

1.2.4 The Coflow Method

Another method of vectoring the jet similar to the counterflow method is the coflow method. In this method instead of suction between the jet and the coanda surface a secondary injection is used. This has been researched at the University of Manchester for use on UAVs by Mason et al. [15]. The parameters investigated were the effect of the slot height and the size of the coanda radius, see Fig. 1.5 for the experimental setup used.

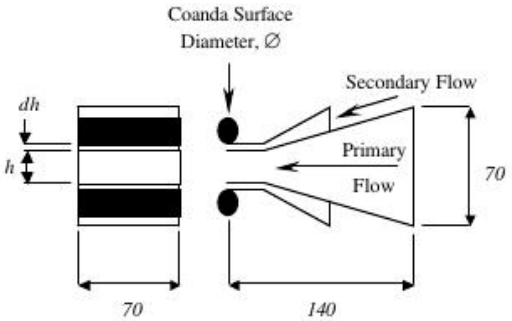

Figure 1.5: Diagram of setup used to investigate coflow fluidic thrust vectoring from [15].

The effectiveness of this method is calculated using the thrust vector coefficient which is the thrust

vector force divided by the resultant thrust, see equation 1.3.

$$C_z = \frac{F_{y,tv}}{F_r} \tag{1.3}$$

One of the observations made from this research was that a minimum secondary mass flow is required to cause initial vectoring. Then there is a linear relationship between the thrust vector coefficient and the momentum ratio of the secondary injection to the primary jet. Eventually a maximum deflection angle is reached and for any increase in the momentum ratio the thrust vector coefficient remains constant. The coflow method has been applied to a demonstrator UAV through the FLAVIIR research program and a successful test flight was made in November 2009 [16]. Some computational work was also performed on this configuration to explore the interaction between the thrust vectoring system and the flow around the UAV by Buonanno et al. [17]. The FTV was used for pitch control in this work, with the yawing moment not considered. The interaction with the surrounding flow was found to increase the effectiveness of the FTV. Both the pitching moment and lift coefficient were improved and the changes varied linearly with the angle of attack, however the increase in C_L was found to be negligible.

1.2.5 Complete Aircraft Configurations

There has been limited work done on complete aircraft configurations employing fluidic thrust vectoring. Some experimental investigations have been conducted in wind and water tunnels on the interaction of vectored jets with the vortices that form over delta wings by Jiang et al. and Wang et al. [18,19]. The wind tunnel experiments were performed to obtain force measurements while flow visualization and PIV were done in the water tunnel, see Fig. 1.6 for a diagram of their water tunnel setup.

Two different sweep angles were looked at, these were 50° and 65°, and were tested at stall and post-stall angles of attack. The effects of the nozzle geometry and position were also investigated by Wang et al. [19]. It was observed that the vortex breakdown was delayed with the jet in use and this was more pronounced for the sweep angle of 65°. They also found that using a rectangular nozzle instead of a

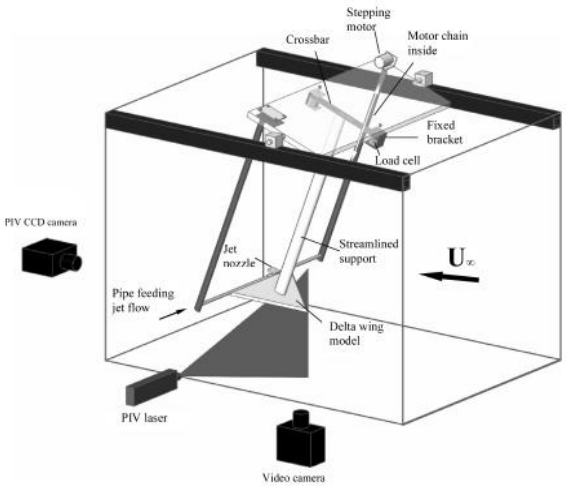

Figure 1.6: Diagram of a water tunnel setup used for experimental investigations from [18].

circular nozzle increases the effects of the jet-vortex interaction due to the differences in the entrainment of the surrounding flow.

Some computational work has also been done on the DEMON configuration within the FLAVIIR programme [17]. The purpose of this was to quantify the effects of the jet entrainment.

The incompressible RANS equations with Menter's SST turbulence model were used to obtain steady solutions on an unstructured mesh. The vectored jet was modelled by imposing the velocity and other flow properties at the engine output, located at the rear of the aircraft. Comparisons were made with a baseline model, not including any control surfaces or the FTV, that had been tested in a wind tunnel at Manchester. Relatively good agreement was obtained at angles of attack up to 15° for the lift and drag coefficients. Then an investigation of the effects of the vectored jet with the flow surrounding the UAV was conducted. It was found that the angle the jet was vectored by was increased by the external flow. Both the lift coefficient and pitching moment coefficient increased, and this increase had a linear relationship with the angle of attack. For the lift the increase was found to be negligible, however for the pitching moment a maximum increase of 0.02 was observed. Also the size of the increase seemed to be dependent on the Mach number of the vectored jet.

1.3 Circulation Control

1.3.1 Early Research and Demonstrator Aircraft

Most research into trailing edge circulation control done in the 1970's and 80's looked into providing high-lift and drag coefficients to develop fixed wing aircraft with short take-off and landing (STOL) capabilities [20, 21]. They wanted to develop a system that did not effect the wing structure, could be powered by bleeding air from the engine and did not require external modifications. For this reason circulation control was a very promising concept at the time as it required only a small modification to the trailing edge of the wing and could provide relatively high C_L without using too much air from the engine. The concept was applied to a 1/5 scale T-2C model and was shown to be capable of doubling the lift coefficient and increasing the drag coefficient by a factor of 2.4 with a blowing coefficient of less than 0.16. Other full sized demonstrator aircraft such as the WVU CC demonstrator, see Fig. 1.7, designed at West Virginia University [22] and the US Navy A-6A [23] were built and flown to show the effectiveness of this concept. A lot of the research during this time focused on determining the relationship between the lift generated and the coanda radius or the secondary injection's momentum [24]. The effects of the slot height relative to the coanda radius and the jet to freestream velocity ratio were also considered to be important parameters.

1.3.2 Recent Concepts and use of CC as Manouevre Effectors

The General Aviation Circulation Control (GACC) wing, see Fig. 1.8, designed by NASA introduced the use of two slots, one on the upperside of the coanda surface and one on the lower, see references [25,26]. The purpose of this was that during cruise conditions both slots could be used at the same time to reduce the drag penalty of the bluff trailing edge. Also using only the lower slot allows for negative lift to be generated. This aerofoil was also used as the basis of some computational work to understand some of the issues of simulating flow control devices by Swanson et al. [27]. These issues included the effects of grid resolution, boundary conditons, initial conditions and the unsteadiness of the flow.

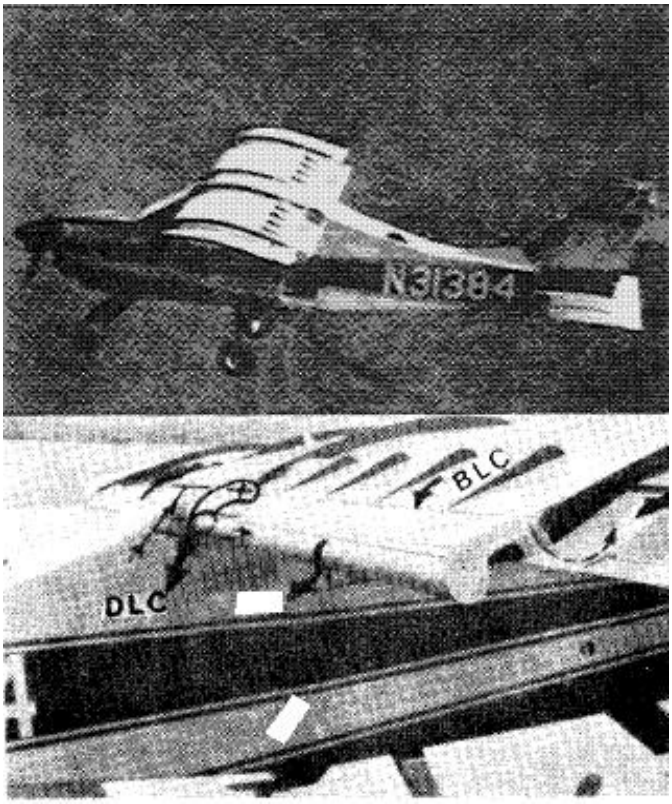

Figure 1.7: The WVU CC technology demonstrator [24].

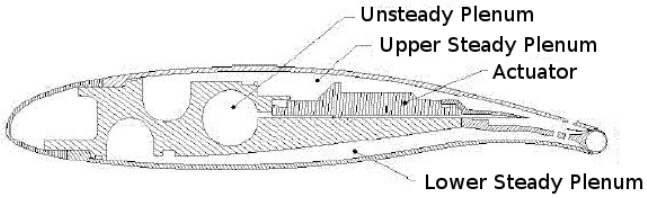

Figure 1.8: The GACC wing [26].

Following this work, there has been some recent research at the University of Manchester and Cranfield University into using circulation control on flapless aircraft to replace the conventional control surfaces (ailerons) as a means of aircraft control [28–30]. These papers are a result of the FLAVIIR research programme, which built an unmanned air vehicle (UAV) to demonstrate new technologies such as circulation control and fluidic thrust vectoring. The circulation control is used to provide roll and pitch control. It was shown that CC effects the control moments of an aerofoil in a similar way to flaps and modifications

to a datasheet method for flaps were made to determine sizing requirements and performance of CC devices by Wilde et al. [30]. The devices are applied to the Java planform, see Fig. 1.9, based on the Boeing X-45A, and compared to conventional control surfaces.

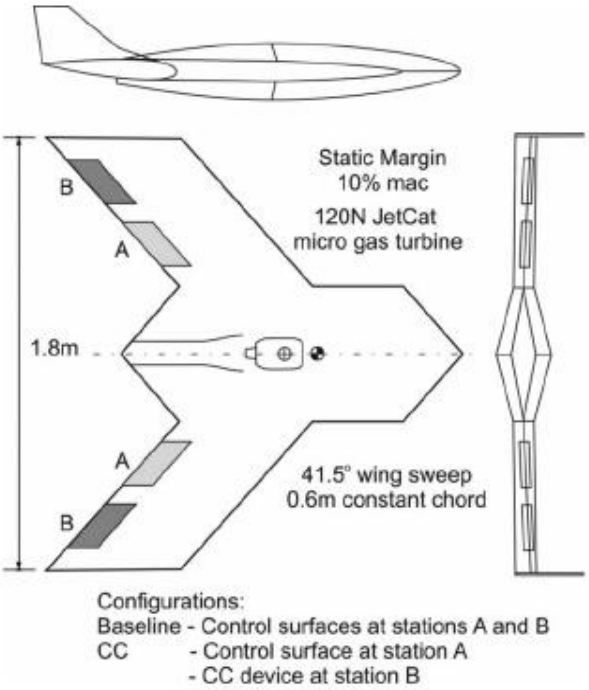

Figure 1.9: Diagram of Java planform with the CC devices and the conventional control surfaces [30].

The CC devices were then applied to the DEMON UAV, which had a successful test flight in November 2009. The sizing and ground testing of the devices is described by Crowther [28]. Another important observation made from this work was that one of the main design drivers was the mass flow requirement rather than the drag penalty relating to the size of the coanda radius. This is because it can be made sufficiently small to create a negligible increase in drag and still provide sufficient lift augmentation. Wind tunnel tests of a wing that would be used on the DEMON are described by Cook et al. [29] to demonstrate that the CC device was as efficient as a flap of a similar width, see Fig. 1.10.

A close-up of the CC device can be seen in the lower portion of the image. The cross-section of this portion has a similar design to that of Fig. 1.8, excluding the unsteady plenum.

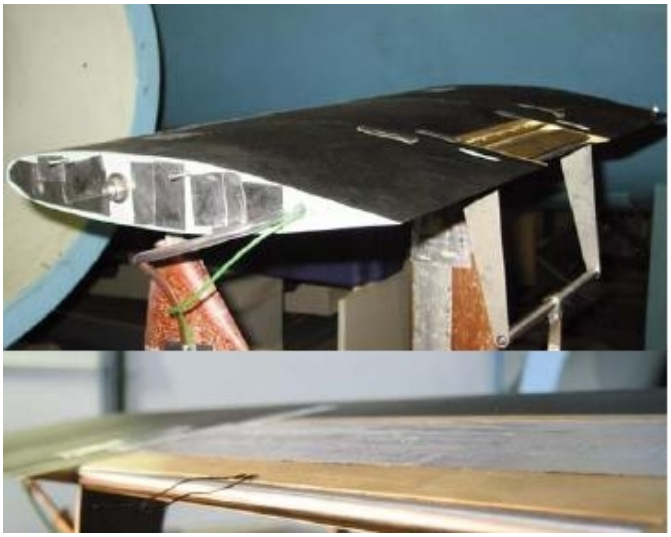

Figure 1.10: Test wing with the CC device installed and a close up of the device [29].

1.3.3 CFD Simulation

There are several difficulties associated with the simulation of these types of flows, such as predicting the separation point on the trailing edge and accurately simulating the airflow at the slot exit [31]. A circulation control workshop held by NASA and ONR in March 2004 looked at applications, experiments and computational work relating to circulation control. The proceedings of this workshop [32] include 30 papers, several of which relate to wind tunnel results and CFD of circulation control aerofoils. One of the aerofoil shapes used was the NCCR 1510-7067N, an elliptical aerofoil with a thickness ratio of 15 percent, see Fig. 1.11.

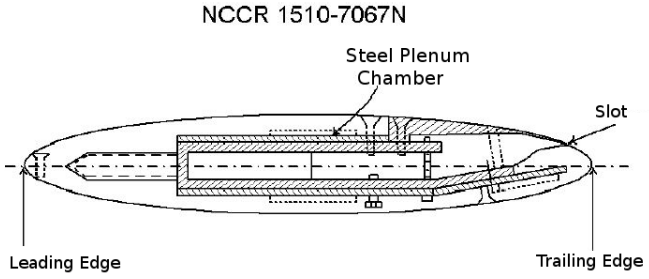

Figure 1.11: Cross sectional geometry of the NCCR 1510-7067N [32].

Turbulence Models	Papers which have used them
Spalart-Allmaras	[27, 33, 34]
Menter's Shear Stress Transport	[27, 33–36]
k-ζ	[27]
Large-Eddy Simulations	[34, 37]

Table 1.1: Turbulence models used by various papers.

A lot of the experimental work done on this aerofoil lacked detailed flowfield data which made comparison with CFD solutions difficult. Due to the small size of the slot, obtaining flowfield data was not feasible. The reasons for discrepancies between the experimental pressure distributions and computational ones could not be explained adequately. The results from the workshop suggested that CFD could not consistently predict the performance of CC aerofoils and wings. A large number of CFD codes, turbulence models and geometries were used, making it difficult to determine where the inadequacies in the prediction methods were. An overview of the CFD validation experiments and a general process for validating CFD codes is described by Jones et al. [31]. Several issues were identified within this paper, with the most important being the measurement of the manufactured wind tunnel geometry, as the spanwise uniformity of the slot can be affected by the plenum pressure. Also noted was the need for velocity profile measurements to allow the discrepancies between CFD solutions and experimental work to be explained. Due to the small size of the slot, obtaining flowfield data was not feasible. It has been found that computational results are very dependent on the turbulence model used and the comparisons deteriorate at higher blowing rates. As most circulation control experiments have not been documented properly for CFD validation, it is difficult to determine whether the turbulence modelling or the loss of two-dimensionality is responsible for the lack of agreement as blowing rates increase. The different turbulence models listed in Table 1.1 have been tried out for these flows, with no one model providing accurate predictions for all the flow features.

Several of these papers also apply rotation and curvature corrections to the SA and SST turbulence

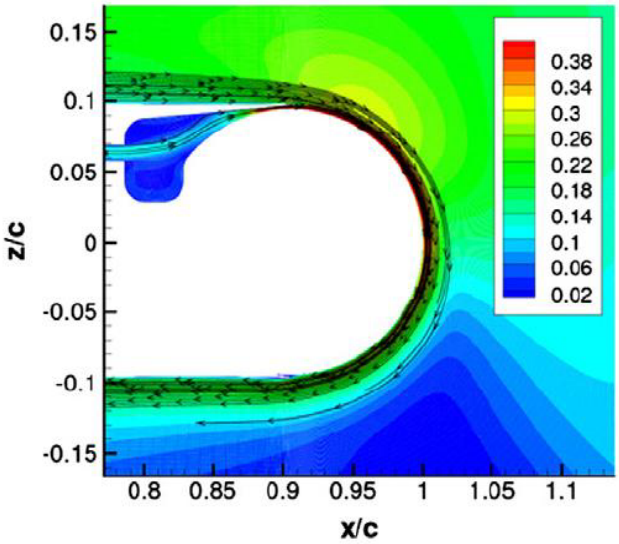

Figure 1.12: Streamlines on mach contours for a circulation control aerofoil using SA turbulence model [34].

models. In all those cases they find that this improves the comparison with measurements. Another observation which most of the papers agree on is that as the blowing rate increases the coanda jet remains attached for too long when using the SA and SST turbulence models. This could result in nonphysical solutions, such as the jet wrapping all the way around onto the bottom surface of the aerofoil see Fig. 1.12.

1.3.4 CC Applied to Swept Wings

There is only one experiment that was found for circulation control applied to swept wings by Wood [38]. The application was in the field of rotors, for improving VTOL capabilities. The purpose of this work was to examine the effects of the sweep angle on a circulation control wing and to demonstrate that the performance of three-dimensional rotors can be estimated using two-dimensional databases. It was observed that no first-order effects of sweep were apparent in the degree of mixing between the trailing-edge jet and the upper surface boundary layer. A 20% thick ellipse was used as an aerofoil section, see Fig. 1.13 for a diagram of the wind tunnel geometry. The experiments were conducted for angles of attack from $-5°$ up to $5°$ and for sweep angles up to $45°$. No effects of the sweep on the interaction

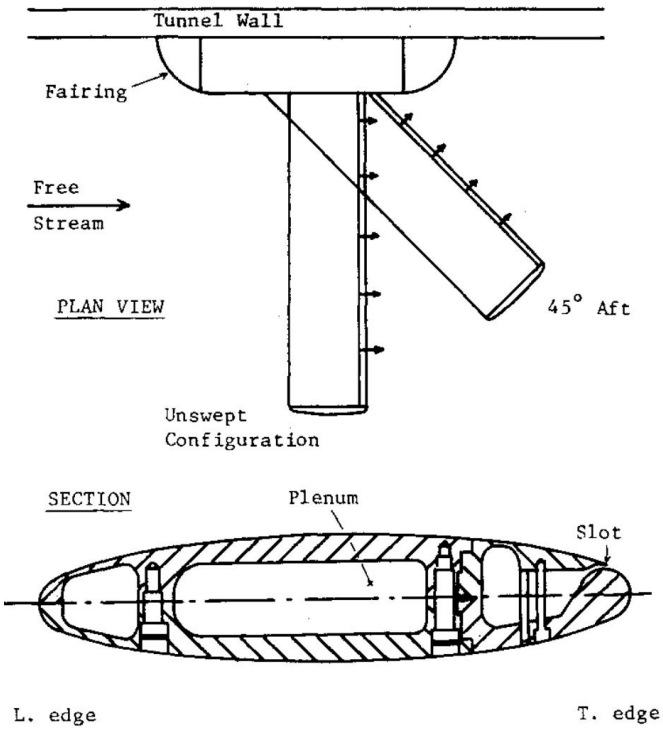

Figure 1.13: Diagram of the wind tunnel geometry from [38].

of the jet and boundary layer were observed within the parameter range tested. The effect of the flow separation over the wing as a result of the high angle of attack on the performance of the CC was not investigated. The lack of high angle of attack results and the choice of aerofoil section limit the usefulness of the results with respect to UAVs.

Chapter 2

Mathematical Formulation

The CFD solver that was used throughout this thesis is the PMB code which has been developed over the past twenty years at the Universities of Liverpool and Glasgow [39]. This work uses the PMB code to solve the RANS equations for steady-state and unsteady time accurate simulations. This section discusses some of the relevant aspects of the RANS equations and the CFD code.

2.1 Reynolds Averaged Navier-Stokes Equations

2.1.1 Navier-Stokes Equations

The Navier-Stokes equations are the starting point for the RANS equations. These equations can be derived from the momentum, mass and energy conservation principles.

The momentum equations can be derived from Newton's second law. They are written in the following form in Cartesian coordinates:

$$\frac{\partial(\rho u)}{\partial t} + \frac{\partial(\rho uu)}{\partial x} + \frac{\partial(\rho uv)}{\partial y} + \frac{\partial(\rho uw)}{\partial z} = -\frac{\partial p}{\partial x} + \frac{\partial \tau_{xx}}{\partial x} + \frac{\partial \tau_{xy}}{\partial y} + \frac{\partial \tau_{xz}}{\partial z} \tag{2.1}$$

$$\frac{\partial(\rho v)}{\partial t} + \frac{\partial(\rho uv)}{\partial x} + \frac{\partial(\rho vv)}{\partial y} + \frac{\partial(\rho vw)}{\partial z} = -\frac{\partial p}{\partial y} + \frac{\partial \tau_{xy}}{\partial x} + \frac{\partial \tau_{yy}}{\partial y} + \frac{\partial \tau_{yz}}{\partial z} \tag{2.2}$$

$$\frac{\partial(\rho w)}{\partial t} + \frac{\partial(\rho uw)}{\partial x} + \frac{\partial(\rho vw)}{\partial y} + \frac{\partial(\rho ww)}{\partial z} = -\frac{\partial p}{\partial z} + \frac{\partial \tau_{xz}}{\partial x} + \frac{\partial \tau_{yz}}{\partial y} + \frac{\partial \tau_{zz}}{\partial z} \tag{2.3}$$

where p is pressure, ρ is density, t is time, u,v and w and velocity components in the x,y and z directions and τ_{ij} are components of the stress tensor. Conservation of mass is used to derive the continuity equation

which is:

$$\frac{\partial \rho}{\partial t} + \frac{\partial(\rho u)}{\partial x} + \frac{\partial(\rho v)}{\partial y} + \frac{\partial(\rho w)}{\partial z} = 0. \tag{2.4}$$

The conservation of energy is used to derive the energy equation which is:

$$\begin{aligned}\frac{\partial}{\partial t}\left[\rho\left(e+\frac{U^2}{2}\right)\right] + \bigtriangledown \cdot \left[\rho\left(e+\frac{U^2}{2}\right)\mathbf{U}\right] = \rho\dot{q} + \frac{\partial}{\partial x}\left(\hat{k}\frac{\partial T}{\partial x}\right) + \frac{\partial}{\partial y}\left(\hat{k}\frac{\partial T}{\partial y}\right) + \frac{\partial}{\partial z}\left(\hat{k}\frac{\partial T}{\partial z}\right) - \frac{\partial(up)}{\partial x} \\ - \frac{\partial(vp)}{\partial y} - \frac{\partial(wp)}{\partial z} - \frac{\partial(u\tau_{xx})}{\partial x} - \frac{\partial(u\tau_{xy})}{\partial x} - \frac{\partial(u\tau_{xz})}{\partial x} - \frac{\partial(u\tau_{xy})}{\partial y} \\ - \frac{\partial(u\tau_{yy})}{\partial y} - \frac{\partial(u\tau_{yz})}{\partial y} - \frac{\partial(u\tau_{xz})}{\partial z} - \frac{\partial(u\tau_{yz})}{\partial z} - \frac{\partial(u\tau_{zz})}{\partial z}\end{aligned} \tag{2.5}$$

where T is the temperature, e is the specific energy, $\mathbf{U}$ is the velocity vector, $\dot{q}$ is the rate of volumetric heat addition per unit mass and $\hat{k}$ is the thermal conductivity. The total energy, E, is given by:

$$E = e + \frac{u^2 + v^2 + w^2}{2}. \tag{2.6}$$

The total enthalpy, H, is:

$$H = E + \frac{p}{\rho}. \tag{2.7}$$

For a Newtonian Fluid the stress tensor components are described using the expressions:

$$\begin{aligned}\tau_{xx} &= -\mu\left[2\frac{\partial u}{\partial x} - \frac{2}{3}\left(\frac{\partial u}{\partial x} + \frac{\partial v}{\partial y} + \frac{\partial w}{\partial z}\right)\right] \\ \tau_{yy} &= -\mu\left[2\frac{\partial v}{\partial y} - \frac{2}{3}\left(\frac{\partial u}{\partial x} + \frac{\partial v}{\partial y} + \frac{\partial w}{\partial z}\right)\right] \\ \tau_{zz} &= -\mu\left[2\frac{\partial w}{\partial z} - \frac{2}{3}\left(\frac{\partial u}{\partial x} + \frac{\partial v}{\partial y} + \frac{\partial w}{\partial z}\right)\right] \\ \tau_{xy} &= -\mu\left(\frac{\partial u}{\partial y} + \frac{\partial v}{\partial x}\right) \\ \tau_{xz} &= -\mu\left(\frac{\partial u}{\partial z} + \frac{\partial w}{\partial x}\right) \\ \tau_{yz} &= -\mu\left(\frac{\partial v}{\partial z} + \frac{\partial w}{\partial y}\right).\end{aligned} \tag{2.8}$$

where μ is the laminar viscosity which is determined using Sutherland's law as follows:

$$\frac{\mu}{\mu_0} = \left(\frac{T}{T_0}\right)^{\frac{3}{2}} \frac{T_0 + 110}{T + 110}. \tag{2.9}$$

The reference values, μ_0 and T_0, are specified as $1.7894 \times 10^{-5} kg/ms$ and $288.16K$ respectively.

The components of the heat flux vector are determined using Fourier's Law:

$$\begin{aligned} q_x &= -\hat{k}\frac{\partial T}{\partial x} = -\frac{1}{(\gamma-1)M_\infty^2}\frac{\mu}{P_r}\frac{\partial T}{\partial x} \\ q_y &= -\hat{k}\frac{\partial T}{\partial y} = -\frac{1}{(\gamma-1)M_\infty^2}\frac{\mu}{P_r}\frac{\partial T}{\partial y} \\ q_z &= -\hat{k}\frac{\partial T}{\partial z} = -\frac{1}{(\gamma-1)M_\infty^2}\frac{\mu}{P_r}\frac{\partial T}{\partial z} \end{aligned} \tag{2.10}$$

where γ is the specific heat capacity ratio, M_∞ is the freestream Mach number and P_r is the Prandtl number.

2.1.2 Vector Form of Navier-Stokes Equations

The Navier-Stokes equations can be written in vector form as:

$$\frac{\partial \mathbf{W}}{\partial t} + \frac{\partial(\mathbf{F}^i + \mathbf{F}^v)}{\partial x} + \frac{\partial(\mathbf{G}^i + \mathbf{G}^v)}{\partial y} + \frac{\partial(\mathbf{H}^i + \mathbf{H}^v)}{\partial z} = 0, \tag{2.11}$$

where $\mathbf{W}$ is a column vector of the conserved variables:

$$\mathbf{W} = [\rho, \rho u, \rho v, \rho w, \rho E]^T, \tag{2.12}$$

$\mathbf{F}^i$, $\mathbf{G}^i$ and $\mathbf{H}^i$ are the inviscid flux vectors:

$$\begin{aligned} \mathbf{F}^i &= \left[\rho u, \rho u^2 + p, \rho uv, \rho uw, u(\rho E + p)\right]^T \\ \mathbf{G}^i &= \left[\rho v, \rho uv, \rho v^2 + p, \rho vw, v(\rho E + p)\right]^T \\ \mathbf{H}^i &= \left[\rho w, \rho uw, \rho vw, \rho w^2 + p, w(\rho E + p)\right]^T \end{aligned} \tag{2.13}$$

and $\mathbf{F}^v$, $\mathbf{G}^v$ and $\mathbf{H}^v$ are the viscous flux vectors:

$$\begin{aligned}
\mathbf{F}^v &= [0, \tau_{xx}, \tau_{xy}, \tau_{xz}, u\tau_{xx} + v\tau_{xy} + w\tau_{xz} + q_x]^T \\
\mathbf{G}^v &= [0, \tau_{xy}, \tau_{yy}, \tau_{yz}, u\tau_{xy} + v\tau_{yy} + w\tau_{yz} + q_y]^T \\
\mathbf{H}^v &= [0, \tau_{xz}, \tau_{yz}, \tau_{zz}, u\tau_{xz} + v\tau_{yz} + w\tau_{zz} + q_z]^T .
\end{aligned} \tag{2.14}$$

It is this form of the Navier-Stokes equations that is solved using the PMB code. These equations are non-dimensionalised, so that all variables are approximately of order 1, in the following way:

$$\begin{aligned}
\hat{x} &= \frac{x}{L^*} & \hat{y} &= \frac{y}{L^*} & \hat{z} &= \frac{z}{L^*} \\
\hat{u} &= \frac{u}{M_\infty} & \hat{v} &= \frac{v}{M_\infty} & \hat{w} &= \frac{w}{M_\infty} \\
& & \hat{\rho} &= \frac{\rho}{\rho_\infty} & \hat{p} &= \frac{1}{\gamma M_\infty^2}
\end{aligned} \tag{2.15}$$

where the variables with the hat are the non-dimensional variables and L^* is a characteristic lengthscale. To determine the Reynolds stress tensor components τ_{ij} the Boussinesq approximation is used. This states that the Reynolds stress tensor is proportional to the strain-rate tensor of the mean flow as follows:

$$\tau_{ij} = 2\mu_t S_{ij} - \frac{2}{3}\rho k \delta_{ij} \tag{2.16}$$

2.1.3 Reynolds Averaging

Direct numerical simulation of the full Navier-Stokes equations requires a large amount of computational power, and is not feasible for complete aircraft configurations at flight Reynolds numbers. Because of this, the turbulent nature of the flow is approximated. This is done by separating the variables into two parts, the mean component and the fluctuations due to the turbulence:

$$\begin{aligned}
u &= \bar{u} + u' & v &= \bar{v} + v' & w &= \bar{w} + w' \\
& & \rho &= \bar{\rho} + \rho' & p &= \bar{p} + p' .
\end{aligned} \tag{2.17}$$

Aside from the Reynolds stress tensor and heat flux equations, 2.8 and 2.10 respectively, the Navier-Stokes equations remain unaltered by this change of variables. The expressions for the stress tensor components are obtained after substituting the new variables into equation 2.8 and simplifying. For τ_{xx} it is:

$$\tau_{xx} = -\left(\mu + \mu_t\right)\left[2\frac{\partial u}{\partial x} - \frac{2}{3}\left(\frac{\partial u}{\partial x} + \frac{\partial v}{\partial y} + \frac{\partial w}{\partial z}\right)\right] \tag{2.18}$$

where μ_t is the turbulent eddy viscosity and is determined using a turbulence model. The expressions for the other stress tensor components can be determined in a similar way to include the turbulent part. For the heat flux components the following expression is obtained, for q_x, after this procedure:

$$q_x = -\frac{1}{(\gamma - 1)M_\infty^2}\left(\frac{\mu}{P_r} + \frac{\mu_t}{P_{rt}}\right)\frac{\partial T}{\partial x} \tag{2.19}$$

where P_{rt} is the turbulent Prandtl number. Similar expressions including P_{rt} are obtained for q_y and q_z. For compressible flows a Favre averaging is used, this is decribed in more detail in reference [40].

2.2 Turbulence Modelling

The two turbulence models that are used in this thesis are the Wilcox k-ω model and Menter's SST model. These two models were chosen because they have been shown to be suitable for aerospace applications [39]. The suitability of the models for the work performed in this thesis is discussed with the relevant results. The equations governing the two models can be seen in the following sections.

2.2.1 Wilcox k-ω Model

The main turbulence model that was used throughout this thesis is the Wilcox k-ω model. This is a two equation model that has been formulated by Wilcox [41]. The turbulent eddy viscosity is determined by:

$$\mu_t = \frac{\rho k}{\omega} \tag{2.20}$$

where k is the turbulent kinetic energy per unit mass and ω is the specific dissipation rate. The equations used to determine these variables are:

$$\frac{\partial(\rho k)}{\partial t} + \frac{\partial(\rho u_j k)}{\partial x_j} - \frac{\partial}{\partial x_j}\left[(\mu + \sigma_1 \mu_t)\frac{\partial k}{\partial x_j}\right] = P_k - \beta_1 \rho k \omega \tag{2.21}$$

$$\frac{\partial(\rho \omega)}{\partial t} + \frac{\partial(\rho u_j \omega)}{\partial x_j} - \frac{\partial}{\partial x_j}\left[(\mu + \sigma_2 \mu_t)\frac{\partial \omega}{\partial x_j}\right] = P_\omega - \beta_2 \rho \omega^2 \tag{2.22}$$

where P_k and P_ω are production terms for k and ω, respectively. These are given by the following:

$$P_k = \tau_{ij}\frac{\partial u_i}{\partial x_j} \qquad P_\omega = \alpha_1 \frac{\omega}{k} P_k. \tag{2.23}$$

where τ_{ij} has the following form:

$$\tau_{ij} = \mu_t \left(2S_{ij} - \frac{2}{3}\frac{\partial u_k}{\partial x_k}\delta_{ij}\right) - \frac{2}{3}\rho k \delta_{ij} \tag{2.24}$$

The values used for the constants are as follows:

$$\alpha_1 = \frac{5}{9} \qquad \beta_1 = \frac{9}{100} \qquad \beta_2 = \frac{3}{40} \qquad \sigma_1 = \sigma_2 = \frac{1}{2}. \tag{2.25}$$

The values for these constants have been tuned to match the results of DNS simulations and experimental results of turbulent flows [41].

k and ω are non-dimensionalised within the solver in the following way:

$$\hat{k} = \frac{kRe}{M_\infty^2} \qquad \hat{\omega} = \frac{\omega L^*}{M_\infty} \tag{2.26}$$

2.2.2 Vortex Correction

A modification to the Wilcox k-ω model was introduced by Brandsma et al. [42] to improve the prediction for flows dominated by vortices. In the original Wilcox k-ω model the production of k and

ω do not take into account the rotation rate and depend only on the mean strain-rate of the flow. As a result of this the regions of high vorticity are not taken into account causing an over-production of turbulent kinetic energy in the vortex core.

To improve the predictions within the vortex core a correction term for the production of the dissipation rate is used. So that this can be applied to the appropriate regions of the flow, a sensor is used to separate the vortex cores from the shear layers. This is defined as the ratio of magnitude of the mean strain-rate tensor to the magnitude of the mean rotation tensor:

$$R = \frac{S}{\Omega} \tag{2.27}$$

In the shear layers, the two tensors are approximately equal, so that $R \approx 1$. In contrast to this, in the vortex cores where the flow approaches a rotational state, $R \ll 1$. The correction to the production of the dissipation rate is then:

$$P_{\omega,modified} = \frac{P_{\omega,original}}{min(R^2, 1)} \tag{2.28}$$

2.2.3 Menter's SST

Another turbulence model that was used for this work is the Menter's SST model [43]. This model combines the Wilcox k-ω model with the standard k-ϵ model. The k-ω model is used in the inner region of the boundary layer and gradually switched to the k-ϵ model in the outer region. The turbulent eddy viscosity for this model is determined by:

$$\mu_t = \frac{\rho \alpha_1 k}{max(\alpha_1 \omega, \Omega F_2)} \tag{2.29}$$

The equations for k and ω are as follows:

$$\frac{\partial(\rho k)}{\partial t} + \frac{\partial(\rho u_j k)}{\partial x_j} - \frac{\partial}{\partial x_j}\left[(\mu + \sigma_k \mu_t)\frac{\partial k}{\partial x_j}\right] = P_k - \beta^* \rho k \omega \tag{2.30}$$

$$\frac{\partial(\rho \omega)}{\partial t} + \frac{\partial(\rho u_j \omega)}{\partial x_j} - \frac{\partial}{\partial x_j}\left[(\mu + \sigma_\omega \mu_t)\frac{\partial \omega}{\partial x_j}\right] = \frac{\gamma}{\nu_t} P_\omega - \beta_2 \rho \omega^2 + 2(1 - F_1)\frac{\rho \sigma_{\omega 2}}{\omega}\frac{\partial k}{\partial x_j}\frac{\partial \omega}{\partial x_j} \tag{2.31}$$

where P_k and P_ω have the same form as for the Wilcox k-ω model. The other constants are blends of the inner and outer constants using the following:

$$\phi = F_1 \phi_1 + (1 - F_1)\phi_2 \tag{2.32}$$

where ϕ_1 and ϕ_2 represent the inner and outer constants, respectively. The additional functions and arguments are given by:

$$\begin{gathered} F_1 = tanh(arg_1^4) \qquad F_2 = tanh(arg_2^2) \\ arg_1 = min\left[max\left(\frac{\sqrt{k}}{\beta^* \omega d}, \frac{500\nu}{d^2 \omega}\right), \frac{4\rho \sigma_3 k}{CD_{k\omega} d^2}\right] \qquad arg_2 = max\left(\frac{2\sqrt{k}}{\beta^* \omega d}, \frac{500\nu}{d^2 \omega}\right) \\ CD_{k\omega} = max\left(2\rho\sigma_3 \frac{1}{\omega}\frac{\partial k}{\partial x_j}\frac{\partial \omega}{\partial x_j}, 10^{-20}\right) \qquad \nu_t = \frac{\mu_t}{\rho}. \end{gathered} \tag{2.33}$$

where d is the distance from the field point to the nearest wall. The various constants are given by:

$$\begin{gathered} \gamma_1 = \frac{\beta_1}{\beta^*} - \frac{\sigma_{\omega 1}\kappa^2}{\sqrt{\beta^*}} \qquad \gamma_2 = \frac{\beta_2}{\beta^*} - \frac{\sigma_{\omega 2}\kappa^2}{\sqrt{\beta^*}} \\ \sigma_{k1} = 0.85 \qquad \sigma_{\omega 1} = 0.5 \qquad \beta_1 = 0.075 \\ \sigma_{k2} = 1.00 \qquad \sigma_{\omega 2} = 0.856 \qquad \beta_2 = 0.0828 \\ \beta^* = 0.09 \qquad \kappa = 0.41 \qquad \alpha_1 = 0.31 \end{gathered} \tag{2.34}$$

These constants have been chosen to match the predictions of turbulent flows which have been researched thoroughly [43].

2.3 Numerical Method

2.3.1 Curvilinear Form

For the types of problems that will be solved a variety of geometries will be used. Therefore it is simpler to solve the equations in the curvilinear form. The transformation is done in the following way:

$$\xi = \xi(x, y, z) \tag{2.35}$$

$$\eta = \eta(x, y, z) \tag{2.36}$$

$$\zeta = \zeta(x, y, z) \tag{2.37}$$

The Jacobian determinant of the transformation is:

$$J = \left| \frac{\partial(\xi, \eta, \zeta)}{\partial(x, y, z)} \right|. \tag{2.38}$$

Equation 2.11 then becomes:

$$\frac{\partial \hat{\mathbf{W}}}{\partial t} + \frac{\partial(\hat{\mathbf{F}}^i + \hat{\mathbf{F}}^v)}{\partial \xi} + \frac{\partial(\hat{\mathbf{G}}^i + \hat{\mathbf{G}}^v)}{\partial \eta} + \frac{\partial(\hat{\mathbf{H}}^i + \hat{\mathbf{H}}^v)}{\partial \zeta} = 0 \tag{2.39}$$

where:

$$\hat{\mathbf{W}} = \frac{1}{J}\mathbf{W} \tag{2.40}$$

$$\hat{\mathbf{F}}^i = \frac{1}{J}\left(\xi_x \mathbf{F}^i + \xi_y \mathbf{G}^i + \xi_z \mathbf{H}^i\right) \tag{2.41}$$

$$\hat{\mathbf{F}}^v = \frac{1}{J}\left(\xi_x \mathbf{F}^v + \xi_y \mathbf{G}^v + \xi_z \mathbf{H}^v\right) \tag{2.42}$$

$$\hat{\mathbf{G}}^i = \frac{1}{J}\left(\eta_x \mathbf{F}^i + \eta_y \mathbf{G}^i + \eta_z \mathbf{H}^i\right) \tag{2.43}$$

$$\hat{\mathbf{G}}^v = \frac{1}{J}\left(\eta_x \mathbf{F}^v + \eta_y \mathbf{G}^v + \eta_z \mathbf{H}^v\right) \tag{2.44}$$

$$\hat{\mathbf{H}}^i = \frac{1}{J}\left(\zeta_x \mathbf{F}^i + \zeta_y \mathbf{G}^i + \zeta_z \mathbf{H}^i\right) \tag{2.45}$$

$$\hat{\mathbf{H}}^v = \frac{1}{J}\left(\zeta_x \mathbf{F}^v + \zeta_y \mathbf{G}^v + \zeta_z \mathbf{H}^v\right) \tag{2.46}$$

2.3.2 Steady State Solutions

To solve this system of equations numerically the computational domain is divided into a number of non-overlapping hexahedral cells. This was done by using the grid generation software package, ANSYS ICEM, to construct structured multi-block grids which are read by the solver. A cell-centred method was used to solve the equations for each cell, and using a finite volume formulation the equations are discretised as follows:

$$\frac{d}{dt}\left(\mathbf{W}_{i,j,k} V_{i,j,k}\right) + \mathbf{R}\left(\mathbf{W}_{i,j,k}\right) = 0 \tag{2.47}$$

where $\mathbf{W}_{i,j,k}$ are the flux variables, $V_{i,j,k}$ is the cell volume and $\mathbf{R}\left(\mathbf{W}_{i,j,k}\right)$ are the flux residuals. The fluxes are determined using Osher's Approximate Riemann Solver. MUSCL interpolation, with the Van Albdada Limiter, is used to obtain third order accuracy. For the boundary conditions, halo cells, which are extrapolated from the block interior are used. At solid walls a no-slip velocity condition is used and undisturbed freestream conditions are imposed at the farfield. Therefore, the farfield must be far enough from the geometry so that any disturbances have dissipated and the difference between the flow conditions and the undisturbed freestream becomes negligible. This varies depending on the application, in this thesis, the distance is chosen so that the wake caused by the aerofoil or aircraft has dissipated. An implicit time-marching scheme is then used to obtain a steady-state solution:

$$\frac{\mathbf{W}^{n+1}_{i,j,k} - \mathbf{W}^{n}_{i,j,k}}{\Delta t} + \frac{\mathbf{R}\left(\mathbf{W}^{n+1}_{i,j,k}\right)}{V_{i,j,k}} = 0 \tag{2.48}$$

Equation 2.48 is a system of non-linear algebraic equations. To simplify the procedure the flux residual is linearised in pseudo time to obtain a system of linear equations. These are then solved using a Generalised Conjugate Gradient method. Further details can be found about the solution procedure here [39].

2.3.3 Unsteady Simulations

For time-accurate simulations an implicit dual-time method is used [44]. For each real timestep the solution is marched forward in pseudo-time to achieve convergence. For the time derivative, a three-level discretisation is used resulting in the following equation:

$$\frac{3\mathbf{W}_{i,j,k}^{n+1} - 4\mathbf{W}_{i,j,k}^{n} + \mathbf{W}_{i,j,k}^{n-1}}{2\Delta t} + \frac{\mathbf{R}\left(w_{i,j,k}^{k_m}, q_{i,j,k}^{k_t}\right)}{V_{i,j,k}} = 0 \tag{2.49}$$

where $\mathbf{R}\left(w_{i,j,k}^{k_m}, q_{i,j,k}^{k_t}\right)$ is the spatial discretisation used in the steady-state, with $w_{i,j,k}$ and $q_{i,j,k}$ being the vector form of the values of W and Q in the surrounding cells. The same process is used for the turbulence equations. The result of this is a coupled system of non-linear equations. This system is solved by introducing an interation through pseudo-time:

$$\frac{\mathbf{W}_{i,j,k}^{n+1,k+1} - \mathbf{W}_{i,j,k}^{n+1,k}}{\Delta\tau} + \frac{1}{V_{i,j,k}}\left(\frac{3\mathbf{W}_{i,j,k}^{n+1} - 4\mathbf{W}_{i,j,k}^{n} + \mathbf{W}_{i,j,k}^{n-1}}{2\Delta t} + \frac{\mathbf{R}\left(w_{i,j,k}^{k_m}, q_{i,j,k}^{k_t}\right)}{V_{i,j,k}}\right) = 0 \tag{2.50}$$

with a similar formulation for the turbulence equations. These equations are then linearised and solved using the same process mentioned in the previous section.

2.4 Reservoir Boundary Condition

For the purpose of modelling the devices, a reservoir boundary condition was implemented into PMB. This was applied to the back wall of a plenum chamber, the flow within the chamber up to the slot exit was then determined by the solver, allowing the boundary layer to develop as part of the calculation. The user specifies a NPR as part of the input file used to run a simulation. The velocities and the turbulence variables for the halo cells are extrapolated from the interior. The pressure and density for the halo cells are then determined using the isentropic flow equations as follows:

$$\rho = NPR^{\frac{1}{\gamma}}\left(1 + (\gamma - 1)K\right)^{\frac{-1}{\gamma - 1}} \tag{2.51}$$

$$p = \frac{NPR\,(1 + (\gamma - 1)K)^{\frac{-\gamma}{\gamma - 1}}}{\gamma M^2} \tag{2.52}$$

where K is:

$$K = \frac{1}{2}\,(|U|M)^2 \tag{2.53}$$

2.5 Unsteady Control of the Coanda Jet

During unsteady simulations the capability to turn off the jet is required. For an aircraft there will be a minimum of four slots, upper and lower on the left and right wings. This required several modifications, which are discussed subsequently, to existing functions within PMB. A flow diagram of the process is shown in Fig. 2.1.

An input file is constructed by the user containing the boundary condition codes of the plenum blocks with the number of the block which it is connected to and the number of the face that is connected to the plenum block. At the beginning of each time step the boundary conditions of the block faces are altered to facilitate the required setup, i.e. which jets are in use and which have been switched off. When a particular jet is not being used, which corresponds to a input of negative one in the unsteady input file, the flow in the block is not updated and the block is not included in the calculation of the loads. The block which is part of the external flow has the face which was connected to the plenum chamber changed to a solid boundary condition. When a jet is in use, the required block is included in the flow update and the calculations of the loads. The block which is part of the external flow has its connectivity with the plenum block restored. All other aspects of the CFD simulation are performed as usual, except for the calculation of the loads which also excludes the plenum blocks which are not being used.

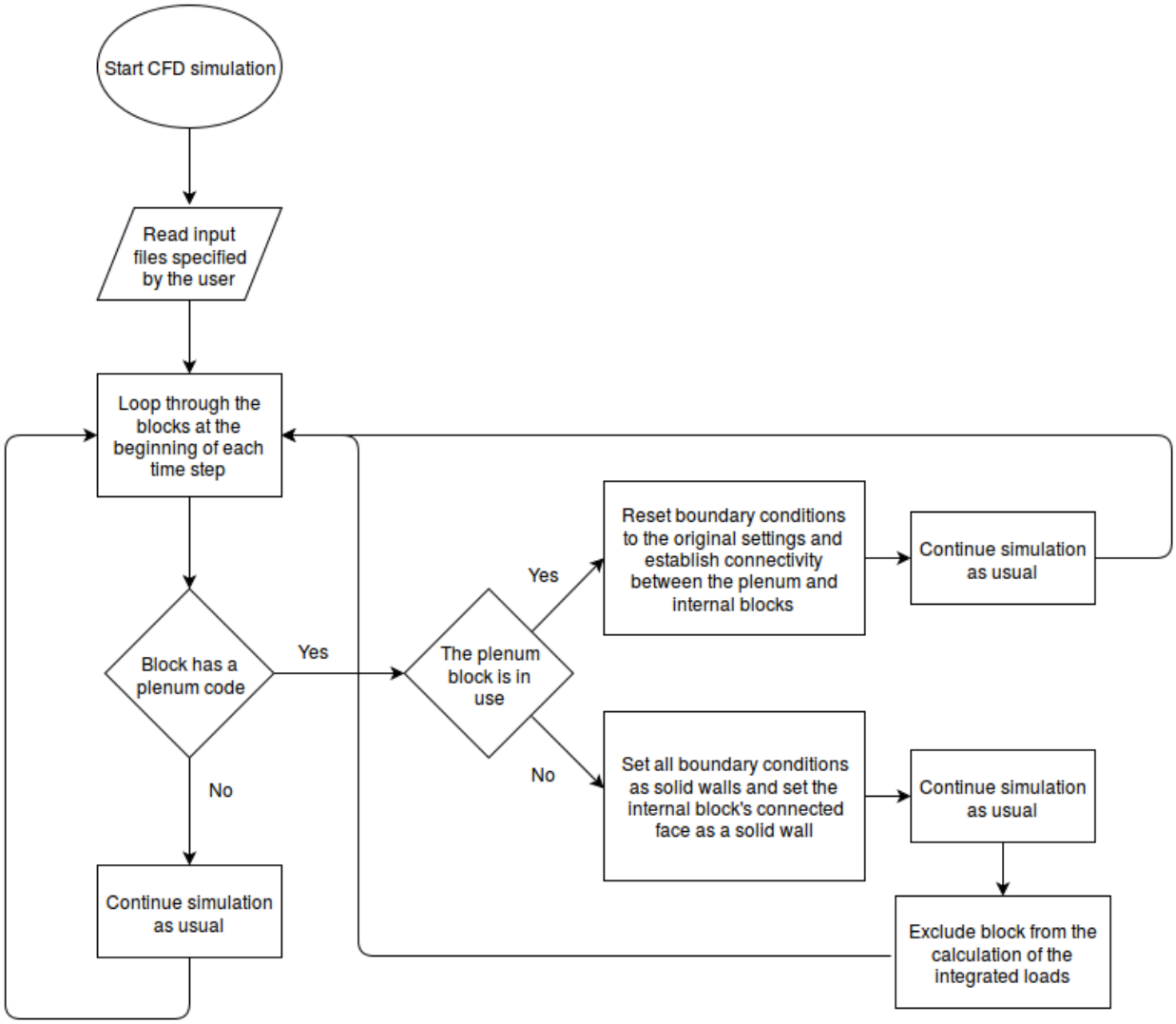

Figure 2.1: Flow chart demonstrating the process used to control the jets during unsteady simulations.

Chapter 3

Validation Test Cases

3.1 Coanda Jet CFD Validation

3.1.1 Geometry and Wind Tunnel Details

The CC-E0020EJ circulation control aerofoil has been designed at the Georgia Institute of Technology (GTRI) for CFD validation purposes. A simple geometry with a large trailing edge radius was chosen to make it easier to obtain accurate experimental data on the coanda surface. The aerofoil has a chord length of 8.6 inches, with an elliptical forebody, straight afterbody and thickness to chord ratio of 20%. A first series of tests was done at the GTRI model test facility. The emphasis of these tests was the performance of the aerofoil and the effect of the slot height. The trailing edge radius is 9.44% of the chord length and the final slot height that was decided on is 0.02 inches, corresponding to a slot height to coanda radius ratio of 0.024, and the slot lip is 0.01 inches. See reference [35] for more details on the construction of the geometry and the wind tunnel experiments. The aerofoil has upper and lower CC slots, with the lower one sealed off for the wind tunnel experiments. A 2D section of the geometry can be seen in Fig. 3.1a and the aerofoil mounted in the wind tunnel in Fig. 3.1b.

A second series of tests was done at NASA's BART installation, which has a test section with a width of 40 inches and a height of 28 inches. These focused on flow characteristics for CFD validation. Measurements of the mean-velocity and turbulence profiles at the slot exit were taken outside the wind tunnel (zero freestream velocity) using a hot-wire with a nozzle pressure ratio of 1.10 and 1.21. Wind

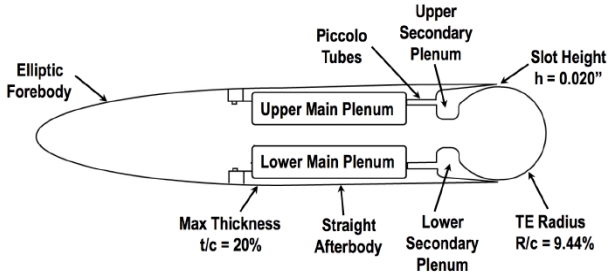

(a) A 2D section of the wind tunnel geometry.

(b) The aerofoil mounted in the wind tunnel.

Figure 3.1: Diagram and picture of the wind tunnel geometry from [35].

tunnel experiments were conducted at nozzle pressure ratios of 1.081 and 1.208. Surface pressure coefficients, aerodynamic loads and the massflow through the slot were recorded from this set of wind tunnel experiments. The aerofoil is 30 inches wide and was mounted upright in the wind tunnel, spanning the whole height. The pressure taps were located at the midspan of the model, which, due to the setup was 13 inches from the floor and 15 inches from the ceiling.

A few issues were observed from the first two sets of wind tunnel experiments and the CFD solutions that were done alongside them. This led to the internal geometry of the aerofoil being modified to eliminate recirculation zones within the secondary plenum chamber to simplify the internal flow in an attempt to reduce possible sources of discrepancy between experimental results and CFD results [36]. Also measurements of the outer geometry and the end of the second plenum were made. These consist of about 1450 points that have not been smoothed. Three different test cases were run, with low, mid and high levels of blowing which correspond to blowing coefficients of approximately 0.047, 0.115 and 0.150 respectively, where

$$C_\mu = \frac{\dot{m}_j u_j}{q_\infty S} \tag{3.1}$$

with

$$u_j = \sqrt{\frac{2}{\gamma - 1}\gamma R T_{t,j}(1 - (\frac{p_j}{p_{t,j}})^{\frac{\gamma-1}{\gamma}})} \tag{3.2}$$

and the massflow rate, $\dot{m}_j$, is recorded during the experiment.

Table 3.1 summarises the available data from the experimental results for the aerofoil with the simplified internal geometry for each of the cases run.

	Chordwise C_p	Spanwise C_p	LDV Upper/lower surface velocity profiles
$C_\mu \approx 0.047$	Yes	Yes	Yes
$C_\mu \approx 0.115$	Yes	Yes	Yes
$C_\mu \approx 0.150$	Yes	Yes	No

Table 3.1: Experimental results available from [36].

The second data set was used for comparison as it is more recent and the measured geometry, as opposed to the ideal geometry, is known.

3.1.2 Geometry Smoothing

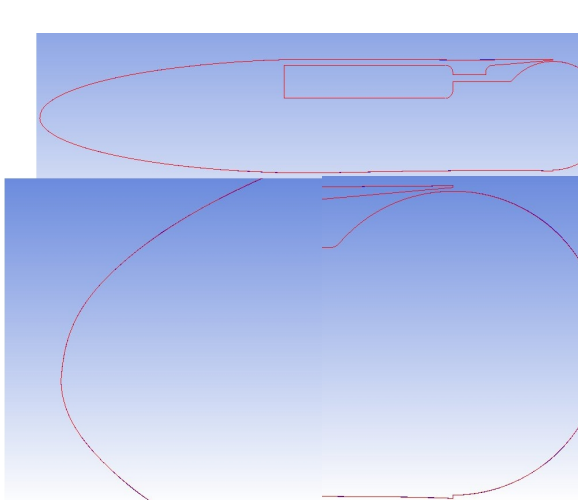

(a) The smoothed geometry, red, and the measure ometry, blue, overlapping each other with close-u the critical areas.

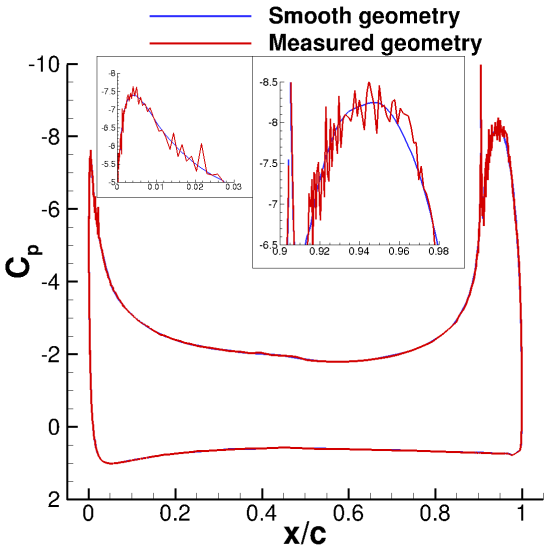

(b) Pressure distribution for NPR=1.22330 using measured and smoothed geometry with a close-up of some of the critical areas.

Figure 3.2: Geometry smoothing process.

The initial geometry resulted in an oscillatory pressure distribution over the surface of the aerofoil due to the discontinuities caused by the numerical representation of the surface. To correct this, the geometry was smoothed by using only a portion of the measured points. This maintains the aerofoil shape but removes any bumps occurring on the surface as a result of the numerical representation. See Fig. 3.2b for the pressure distribution using both these geometries, a close-up of the critical regions, the leading and trailing edge suction peaks can also be seen. Fig. 3.2a shows the two geometries overlapping each other, demonstrating that the difference between the two geometries cannot be seen.

3.1.3 Grids and Computational Setup

A set of multi-block grids was generated using the ANSYS ICEM software package. A short description of the grids will follow with the coarser grids being constructed by reducing the cells along each block edge by various factors, see table 3.2.

Grid	Characteristic Number of Cells Along Each Edge	Total Cells
Fine	100	287,200
Medium	80	183,808
Coarse	60	103,392
Extra Coarse	50	71,800

Table 3.2: Grids used for the refinement study to ensure grid-independent solutions.

A C-grid topology was used at both the leading and trailing edges. The first cell spacing normal to the aerofoil surface was 1×10^{-5} of the chord, ensuring a y^+ of less than 1. Around the coanda surface and at the slot exit, the first cell spacing was half of that. The farfield is 10 chord lengths away in every direction. See Fig. 3.3 for the overall topology and close-ups of some of the key locations.

The Mach number and Reynolds numbers in the wind tunnel varied slightly for each run, see table 3.3 for details, which were replicated in the CFD simulation. The turbulence models used were the Wilcox k-ω and Menter's SST. All the simulations were run as steady-state calculations unless mentioned otherwise.

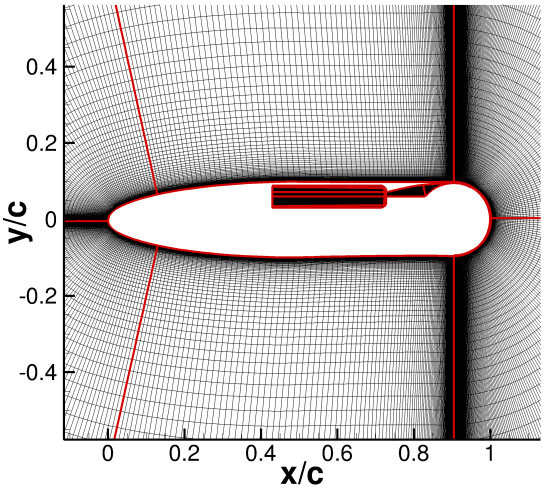

(a) Overall topology.

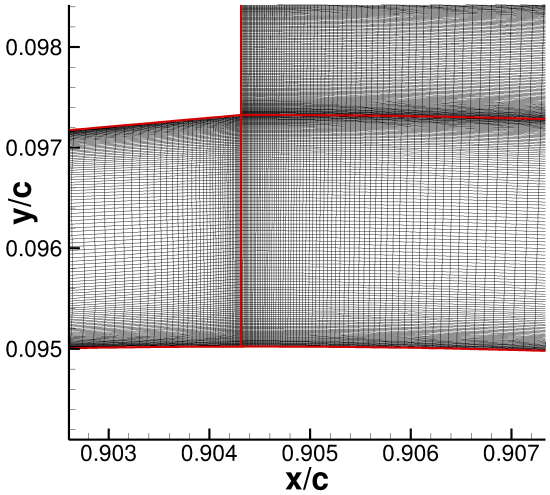

(b) Slot exit.

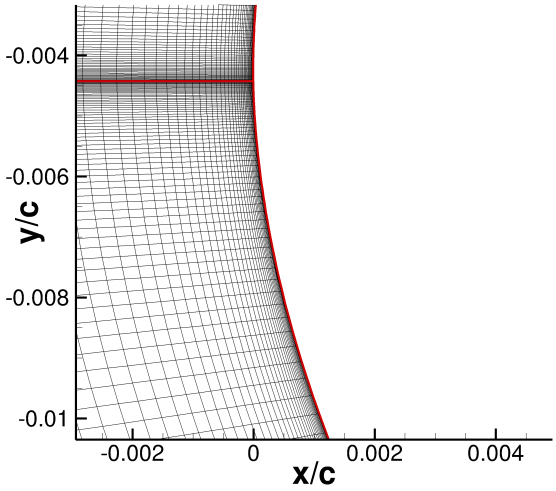

(c) Leading edge.

Figure 3.3: The finest grid used for the CC-EE0020EJ with close-ups of some key locations.

3.1.4 Flowfield Description

The effects of the jet on the overall flowfield can be seen in Fig. 3.4a. The coanda jet wraps around the trailing edge while mixing with the surrounding flow and separating once it has lost its momentum. Increasing the NPR moves this point further along the coanda surface and eventually onto the bottom

	low blowing case	mid blowing case	high blowing case
freestream Mach number	0.10049	0.10057	0.10069
nozzle pressure ratio	1.08755	1.22330	1.30329
Reynold's number	488,000	487,000	508,800

Table 3.3: Details of the Mach and Reynolds numbers for the wind tunnel experiments [36].

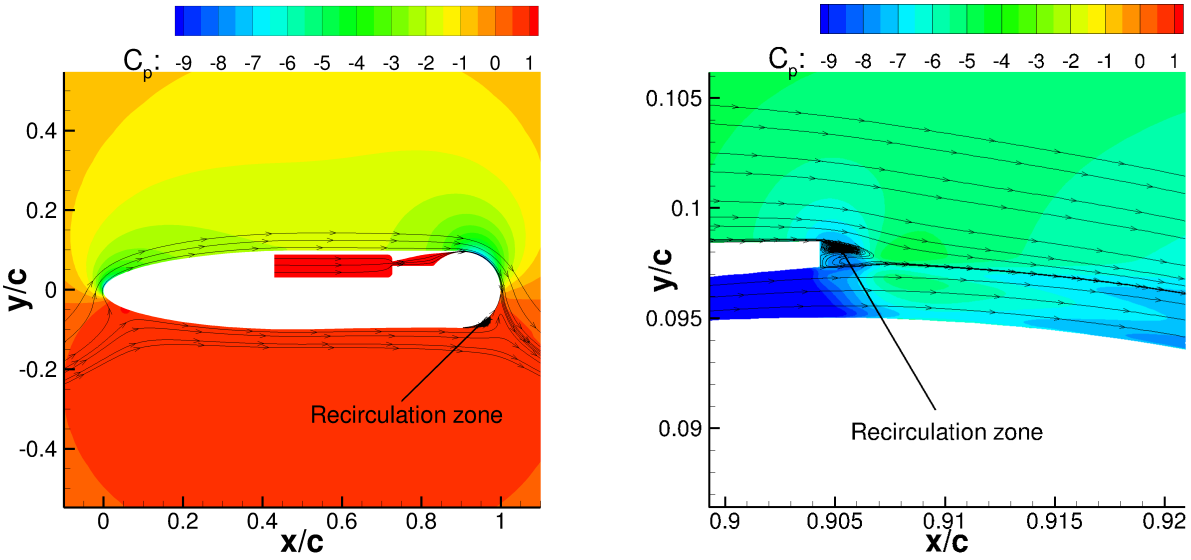

(a) Overall flowfield for the CC-E0020EJ at a NPR of 1.22330 using the Wilcox k-ω model.

(b) Flowfield around the slot for the CC-E0020EJ at a NPR of 1.22330 using the Wilcox k-ω model.

Figure 3.4: Plots of the flowfield for the CC-E0020EJ with the jet on.

surface of the aerofoil. A low pressure region is created behind the trailing edge as a result of this. This causes the flow over the upper surface to accelerate decreasing the pressure coefficient above the aerfoil. There are two recirculation zones. One occurs as a result of the thickness of the slot lip, this can be seen in Fig. 3.4b. The other, is adjacent to the sealed off lower slot and decreases in size as the NPR is increased. The leading edge stagnation point moves downstream along the lower surface creating a suction peak at the leading edge. Increasing the NPR causes the stagnation point to move further downstream, increasing the strength of the suction peak.

3.1.5 Validation Data Comparisons

For the grid refinement study (table 3.2), see Fig. 3.5, only the Wilcox k-ω turbulence model with the middle NPR are presented. Menter's SST model was also used with higher blowing rates to ensure that the solutions are grid-independent at all the blowing rates. All the grids produce a similar C_p distribution with the finer grids predicting slightly lower suction over the coanda surface, Fig. 3.5a. However, the surface pressures just after the slot are effected slighty by the level of refinement, with the finest grid predicting small oscillations. The result of this is slightly lower upper surface velocities, a smaller leading edge suction peak and the stagnation point has not moved as far along the lower surface. For the medium and fine grids there is a unsteadiness in the CFD solution which is suggested in the lift coefficient, Fig. 3.5b. This is most likely caused by the separation bubble present at the lower sealed slot, the separation bubble can be seen in later plots, Figs. 3.7a or 3.7b. The rest of the results presented will be with the coarse grid as the convergence rate is much better and the improvement in the solution is negligible using the finer grids.

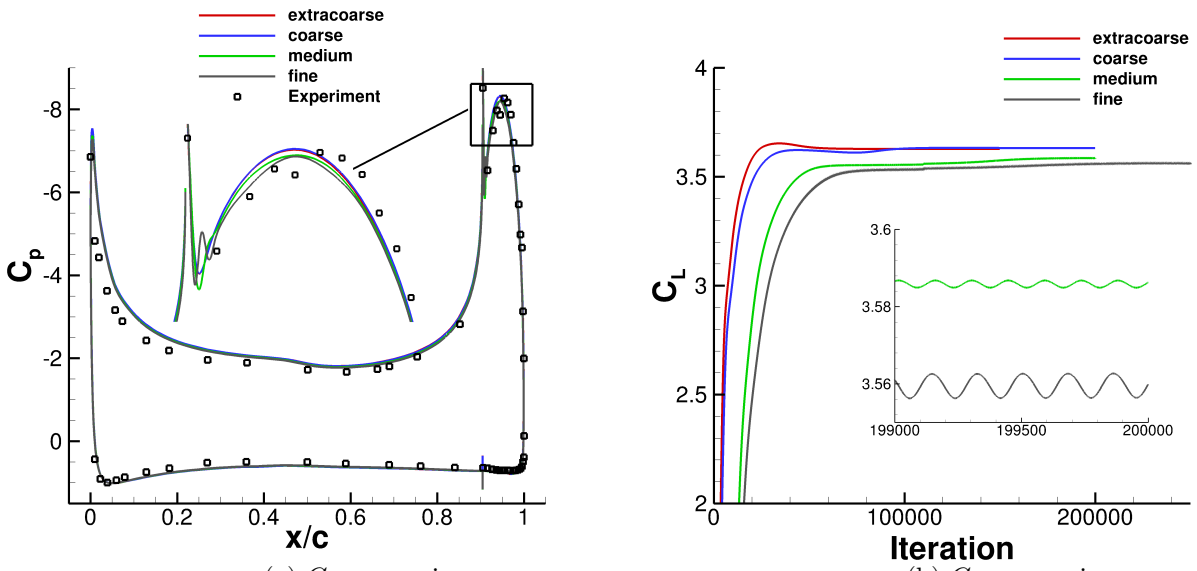

(a) C_p comparison.

(b) C_L comparison.

Figure 3.5: Comparison of the C_p over the surface and the C_L for the grid refinement study.

The integrated loads from the CFD results are given in table 3.4. There are no recorded loads aside from C_μ from the experimental data to compare with. There are loads from the initial set of wind tunnel experiments, but due to geometry differences and differences in the test conditions they are not used. The differences include a different plenum chamber, slightly different blowing rates and other possible minor changes to the external geometry caused by the changes to the plenum chamber. In the experiment, C_μ is estimated by assuming the pressure at the slot is the freestream pressure and using the isentropic flow equations to determine the velocity of the jet at the slot. As can be seen from the table, the discrepancy between the experimental blowing coefficient and the one predicted by the CFD increases for the higher blowing rates. This is because increasing the NPR causes a lower pressure at the slot, increasing the difference between the jet velocity predicted by the isentropic flow equations and the CFD. Further details from the experiment, such as the pressure at the slot exit, are needed to quantify the differences observed in the blowing coefficient.

NPR	Turbulence Model	C_L	C_D	C_μ	C_μ from experiments
low	k-ω	1.744	0.04365	0.05219	0.04680
	SST	1.772	0.04285	0.05288	
middle	k-ω	3.632	0.07474	0.12187	0.11411
	SST	3.959	0.08243	0.12447	
high	k-ω	4.490	0.09547	0.15729	0.14980
	SST	5.093	0.11468	0.16263	

Table 3.4: Integrated loads from the CFD results.

For a comparison of the C_p distribution with measurements see Fig. 3.6. At the lowest NPR the choice of turbulence model makes little difference to the result, Fig. 3.6a. Both show good agreement with the experimental results with a slight over prediction of the suction on the upper surface and higher pressure on the lower surface. This could be due to the walls of the wind tunnels preventing the streamlines from curving around the aerofoil as much as they would in free air. At the middle NPR the SST model is predicting more suction over the coanda surface and this difference increases at the highest NPR. The Wilcox k-ω model produces more turbulent eddy viscosity in the shear layer between the jet

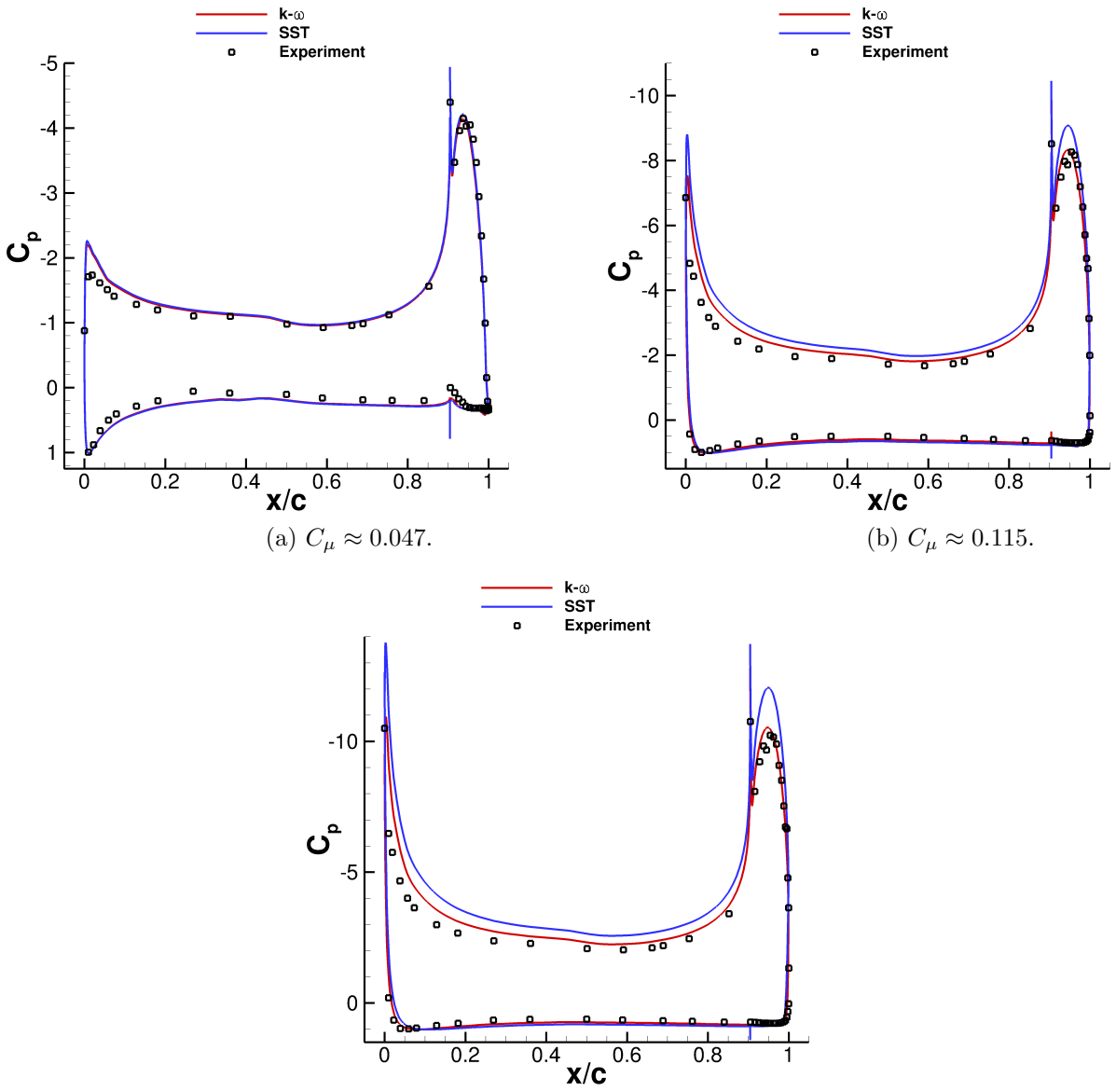

(a) $C_\mu \approx 0.047$.

(b) $C_\mu \approx 0.115$.

(c) $C_\mu \approx 0.150$.

Figure 3.6: Comparison of C_p from the CFD calculations and the experimental results.

and the freestream flow, Fig. 3.7c. This increases the rate of the mixing process between the jet and the surrounding flow, causing it to separate at an earlier point on the trailing edge. The jet remains attached longer with the SST model, this lowers the pressure over the rest of the surface which also has the secondary effect of increasing the C_μ as the velocity of the jet increases due to pressure drop around

the slot increasing the difference further. The Wilcox k-ω model shows relatively good agreement with the experiment over the coanda surface but overpredicts the leading edge suction peak and the location of the stagnation point. Angle of attack corrections are available from the first set of results [35] which were calculated using a CFD method, these were not used in this work due to the way in which they were derived. This was done by adjusting the NPR in the CFD simulation until the pressure distribution over the coanda surface agreed with the experimental results. Then the aerofoil was rotated until there was agreement for the suction peak at the leading edge and this was recorded as the angle correction. A full 3D simulation including the wind tunnel walls would be necessary to quantify the effects of the walls and downwash more precisely. However, these corrections still demonstrate the discrepancy at the leading edge is mostly a result of the downwash.

For a comparison of the boundary layer velocity profiles see Fig. 3.8 for the lowest NPR and Fig. 3.9 for the middle NPR. Similar to the C_p comparison at the lowest NPR, both turbulence models show good agreement with a slight overprediction of the upper surface velocities and underprediction of the lower ones. This is likely due to the walls of the wind tunnel preventing the streamlines from curving as mentioned above. The effect of this is that the leading and trailing edge stagnation points are overpredicted. As a result of this, the location where the velocity measurements were taken in the experiment are further away from the stagnation point on the lower surface, which causes the underprediction. Also, the jet velocity is slightly higher as a result of the overprediction of the jet attachment. These effects become more apparent at the middle NPR, due to the higher lift produced, the effect of the wind tunnel walls increases. Especially when seeing the difference between the two turbulence models, as the SST model is predicting the rear separation point further along the coanda surface the discrepancy is larger.

3.1.6 Other Simulation Results

Other observations relating to the general behaviour of the coanda jets were made during the first set of wind tunnel experiments, prior to the geometry modifications. A lot of these tests were also performed

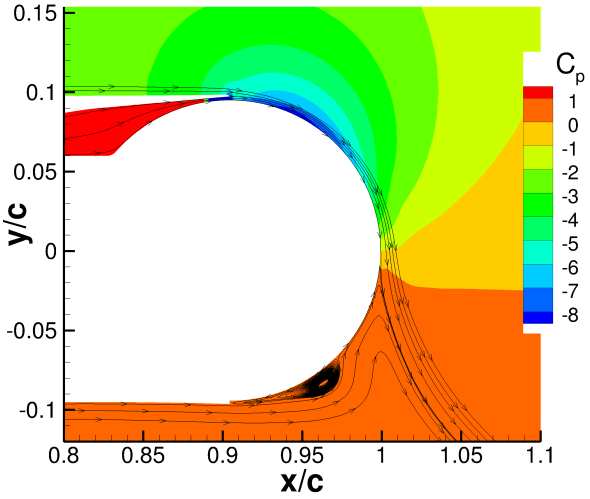

(a) Streamlines on C_p contours for NPR=1.22330 with the Wilcox k-ω turbulence model.

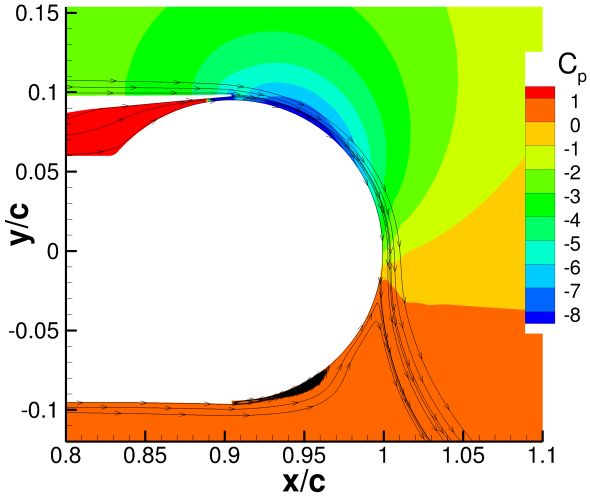

(b) Streamlines on C_p contours for NPR=1.22330 with Menter's SST turbulence model.

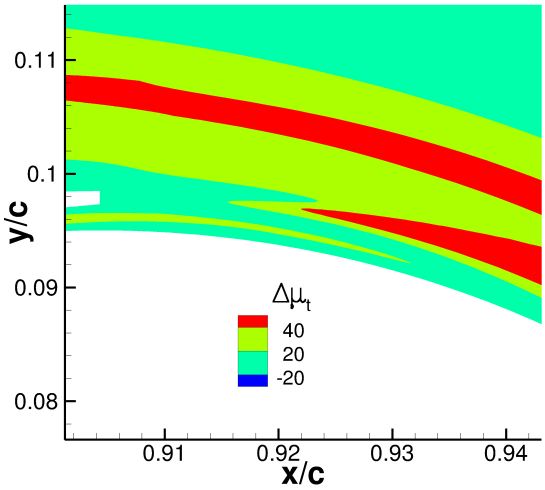

(c) Difference in the ratio of turbulent eddy viscosity to molecular viscosity between the Wilcox k-ω and Menter's SST turbulence models around the slot.

before finalising the slot height, which could also effect the velocity profile of the jet. Relationships between lift coefficient and blowing coefficient and lift versus angle of attack at various blowing coefficients were investigated in these tests. Therefore a qualitative comparison of the behaviours observed will be discussed to ensure the CFD is capable of capturing the general overall trends.

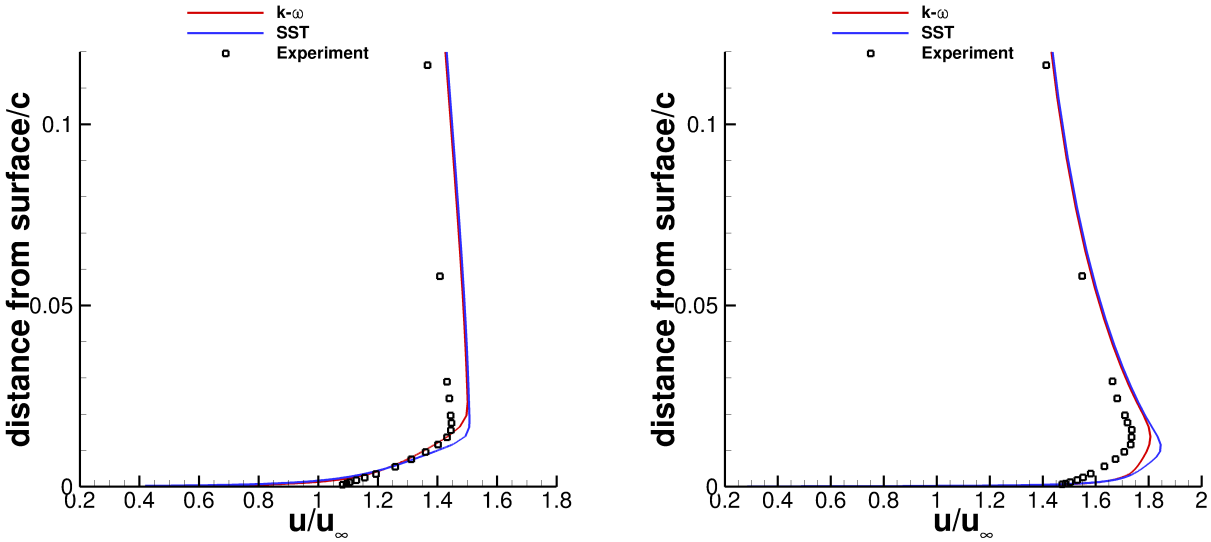

(a) Upper Surface $x/c = 0.8$.

(b) Upper Surface $x/c = 0.9$.

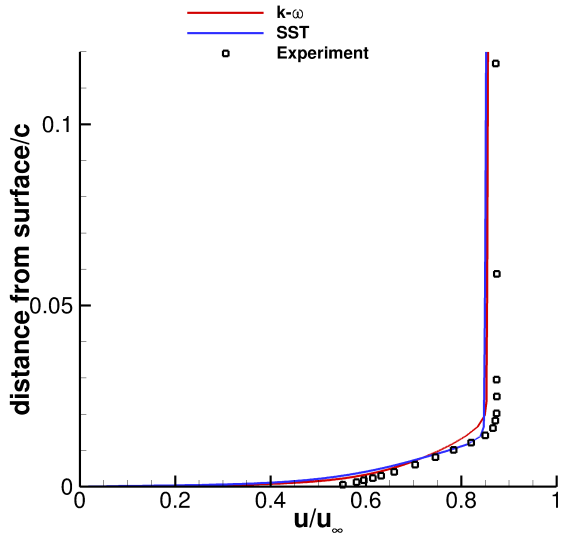

(c) Lower Surface $x/c = 0.8$.

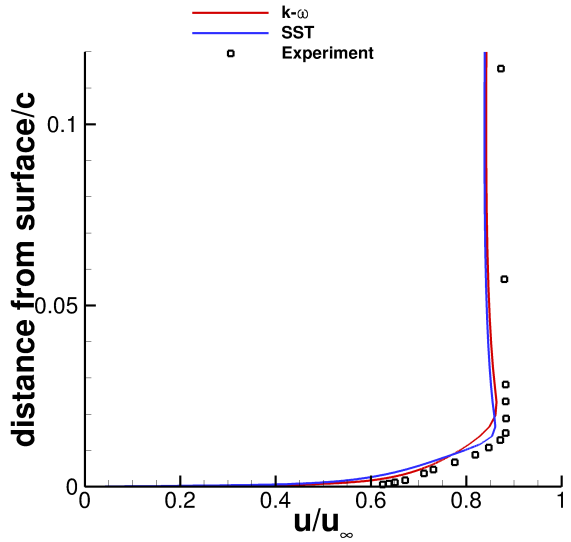

(d) Lower Surface $x/c = 0.9$.

Figure 3.8: Comparison of boundary layer velocites from the CFD calculations and the experimental results for $C_\mu = 0.047$.

For the relationship between lift coefficient and blowing coefficient see Fig. 3.10a. As mentioned earlier, there are minor geometric differences, which have not been documented precisely, for the slot and aerofoil geometry between the CFD and experimental results for this case. Both experiment and CFD show a similar trend, an increase in lift as C_μ is increased with a decrease in slope. There are some

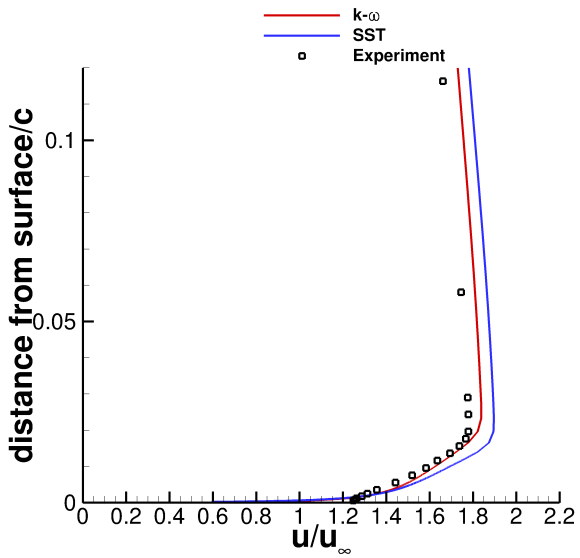

(a) Upper Surface $x/c = 0.8$.

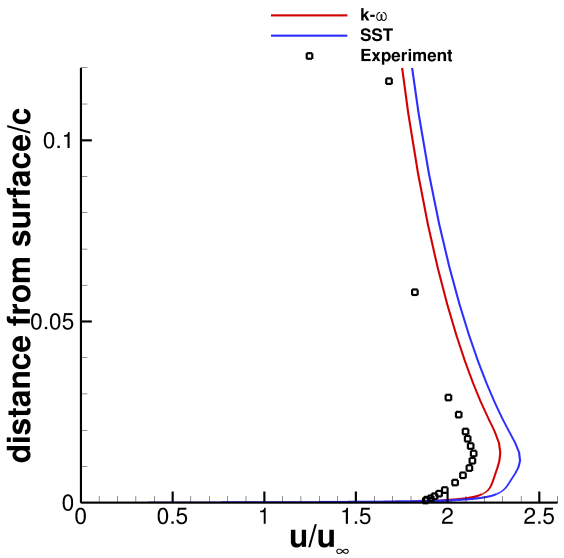

(b) Upper Surface $x/c = 0.9$.

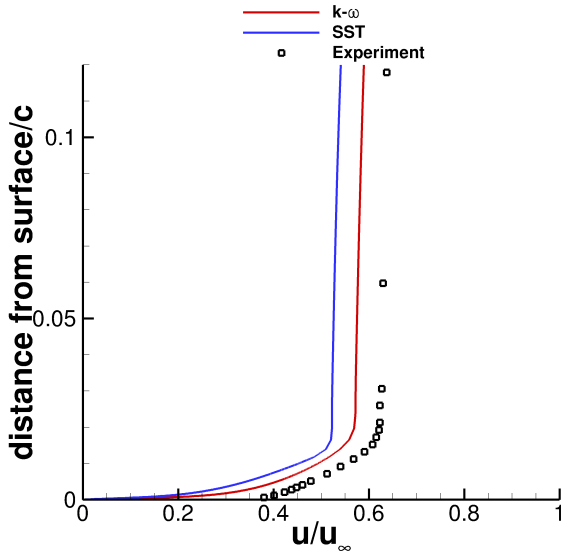

(c) Lower Surface $x/c = 0.8$.

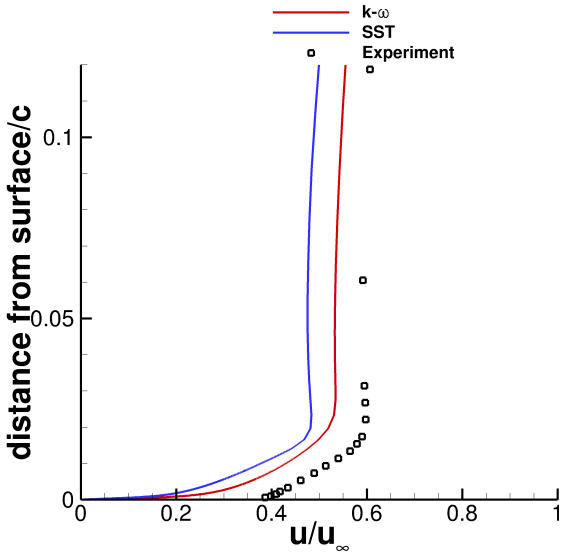

(d) Lower Surface $x/c = 0.9$.

Figure 3.9: Comparison of boundary layer velocites from the CFD calculations and the experimental results for $C_\mu = 0.115$.

slight discontinuities in the CFD results for blowing coefficients higher than 0.35. This is because C_μ is being calculated at the slot exit for the CFD results. The jet becomes supersonic at the higher NPRs and the sonic line occurs earlier in the plenum chamber. As a result of this, there are compression and decompression waves at the slot exit that cause changes in the jet velocity. This becomes clear when C_L

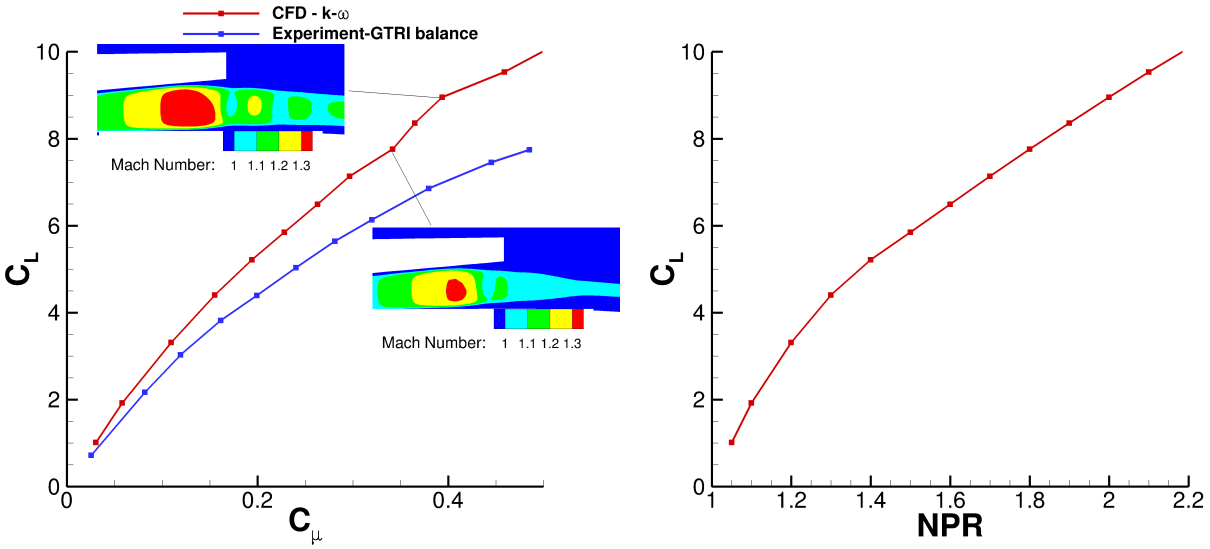

(a) C_L vs. C_μ.

(b) C_L vs. NPR.

Figure 3.10: Lift coefficient vs C_μ and NPR with close-ups of the slot with Mach contours at two points of interest.

is plotted against the NPR as the CFD results appear smoother, Fig. 3.10b. The discrepancy between the experimental and CFD results increases for higher blowing coefficients. This is expected for two reasons, firstly C_μ is being underpredicted in the experiment due to the assumption that the pressure at the slot is the freestream pressure. Secondly the effects of the wind tunnel walls increase as lift generated increases. Both these sources of error are affected, adversely, by increasing the blowing coefficient causing the increase in the discrepancy between the CFD and experimental results.

For a comparison of the stall angles at various blowing coefficients see Fig. 3.11. In the experiments this relationship was investigated at various slot heights before the geometry had been finalised. For this reason no direct comparison will be made, but the trend seen in the CFD results matches that of the experiments. Increasing the blowing coefficient causes a decrease in the stall angle of the aerofoil.

To obtain a better understanding of the mixing process between the coanda jet and the surrounding flow see Fig. 3.12. These plots show the velocity profiles at various points along the coanda surface for a NPR of 1.2233 using a polar coordinate system. The coordinate system has the centre of the coanda

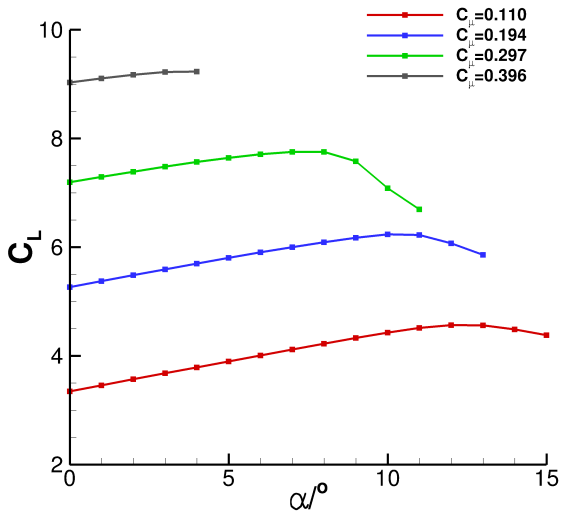

Figure 3.11: C_L vs. α for different C_μ.

surface as the origin and the slot exit as $\theta = 0$ with θ increasing in the clockwise direction. Due to the recirculation zone adjacent to the slot lip the mixing process does not begin until approximately $\theta = 1$. Initially there are sinuisoidal-like oscillations of the flow velocity in the shear layer between the jet and the flow coming off the trailing edge of the aerofoil. This process is smoother for the coarse grid with smaller variations in the velocities. This is followed by a transfer of momentum from the jet to the surrounding flow. The slightly higher jet velocity predicted by the SST model can easily be seen in Fig. 3.12a, also the slower mixing process becomes evident in the last few plots, Figs. 3.12g, 3.12h and 3.12i.

3.1.7 Coanda Jet Validation Summary

From the CFD study it can be seen that with RANS simulation the flow physics of trailing edge CC devices can be predicted with reasonable accuracy. There are a few areas of the flow where there are slight discrepancies relative to the experimental data, such as at the leading edge, the stagnation point's location is predicted further downstream and the suction peak is overpredicted. However, these discrepancies can be partly explained by experimental issues like the downwash caused by the high lift generated. Therefore it is unclear how much of the discrepancy is caused by a deficiency in the simulation

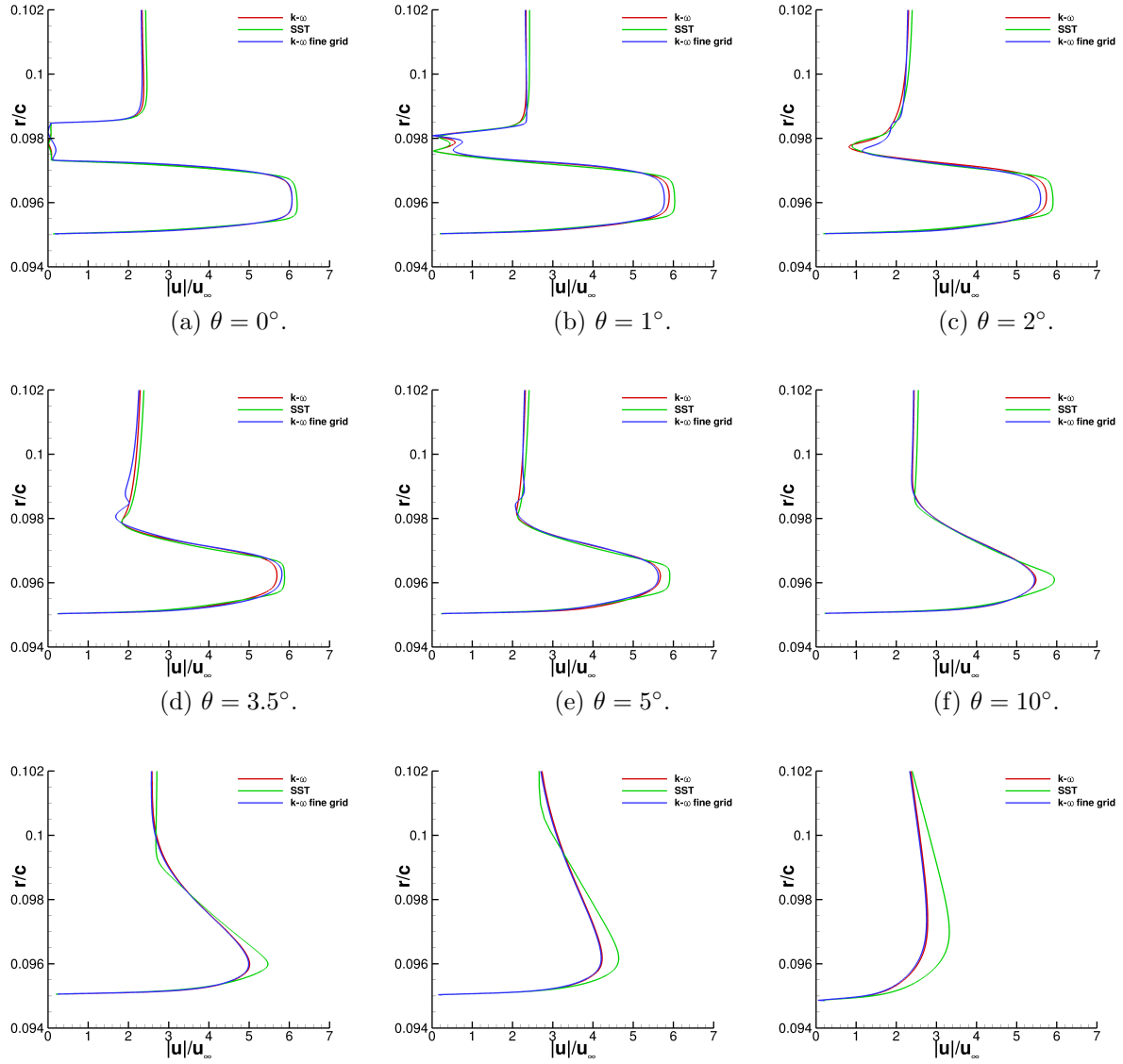

(a) $\theta = 0°$. (b) $\theta = 1°$. (c) $\theta = 2°$.

(d) $\theta = 3.5°$. (e) $\theta = 5°$. (f) $\theta = 10°$.

(g) $\theta = 20°$. (h) $\theta = 40°$. (i) $\theta = 80°$.

Figure 3.12: Velocity profiles at various points along the coanda surface for NPR=1.22330.

methods and how much by the wind tunnel wall effects and the three dimensional flow features in the experiment. A 3D CFD simulation could be used to quantify these discrepancies more precisely. However, as the aim of this thesis is the application of these devices to a UCAV planform and obtaining a general understanding of how they might perform the level of agreement is adequate for these purposes. Another conclusion that can be drawn from this validation case is that the Wilcox k-ω turbulence model provides

the best comparisons with the experimental data. This is due to the fact that the rear separation point predicted by the Wilcox k-ω model is closer to the experimental one and this is one of the key features of these types of flows. The major difference between the two turbulence models is the amount of eddy viscosity generated in the shear layer between the coanda jet and the flowing coming off the upper surface. Further flow details around the slot exit from the wind tunnel experiments would be useful to confirm that the Wilcox k-ω model is predicting the flow conditions in these regions accurately.

3.2 UCAV Validation Test Case

The SACCON (Stability and Control Configuration) is a UCAV planform which is used as a validation test case to demonstrate that the PMB code is capable of predicting the behaviour of vortical flowfields that are typically encountered by UCAVs with reasonable accuracy. This geometry was adapted later to include trailing edge circulation control. It is a lambda wing with a sweep angle of 53° and a wing washout of 5°. The body has a length of $1.061m$, the chord at the root is $0.479m$, the half-span is $0.769m$ and the wing area is $0.77m^2$.

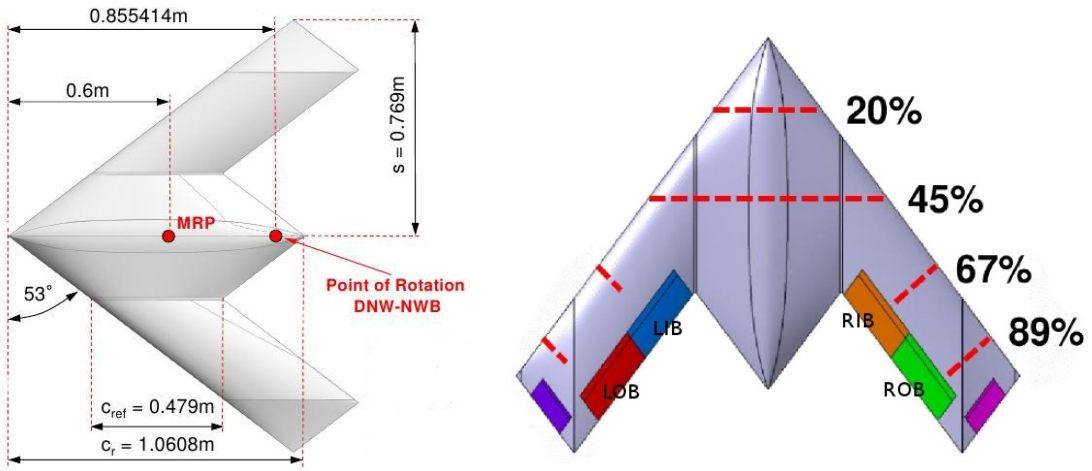

(a) Reference lengths.

(b) Pressure taps and control surfaces.

Figure 3.13: Diagrams of the SACCON planform indicating the reference lengths, location of pressure taps and control surfaces Ref. [45].

This UCAV configuration was used as the main test case for a NATO task group, AVT-161 (2008-2011), assement of stability and control prediction methods for NATO air and sea vehicles. One of the main aims of this group was to determine the current ability of CFD methods for these types of application. An overview of the group's aims and methods is discussed in [45]. For this reason, the SACCON was designed to be a particularly challenging test case which exhibits nonlinear flow. A lot of experimental work has been done in order to obtain static and dynamic aerodynamic loads [46, 47] and PIV data [48, 49] for CFD validation purposes. In conjuction with this, CFD simulations were

performed [50,51] to determine what was predicted accurately and where the CFD could be improved. A new task group, AVT-201 (2011-2015) [52], was established to continue the work performed by AVT-161. This focused on the inclusion of conventional control surfaces and their effectiveness on such a planform, which required new wind tunnel models including inboard and outboard flaps. These are referred to as the F19 which is used for low speed tests and has the dimensions mentioned above and the F17E which is about two and a half times smaller and is used for the high speed tests. See Fig. 3.13 for a planform view of the SACCON with the locations of the pressure taps and the flaps in the experimental setup. The experimental data that is used for comparisons has been obtained from the DNW-NWB wind tunnel in Germany [53].

3.2.1 Treatment of the Control Surfaces

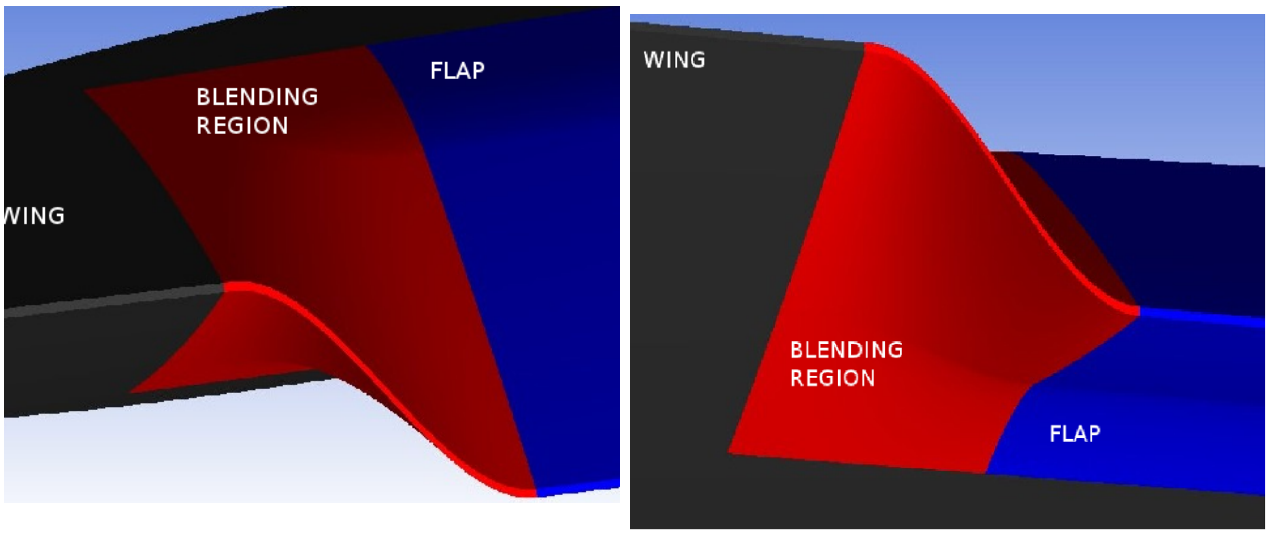

Figure 3.14: Screenshot of the region between the wing (grey) and flap (blue) used as a blending region(red).

Work has been done by Rampurawala at the University of Glasgow [54] on the treatment of control surfaces for use with structured multi-block solvers. This investigates two of the options available which can be used with PMB in its current state. Firstly leaving the flap geometry as is and blocking the gap between the flap and the wing. Secondly using a blending region between the wing and the flap to go from

the trailing edge geometry of the wing to the flap geometry in a smooth fashion. In the work referenced this is done within the CFD solver as the flap geometry is not given. In this work the second option is used as the first one results in extremely low quality cells, due to the skewness, in the gap, it increases the refinement required significantly and it reduces the convergence rate. However, one of the drawbacks of the second option is that the geometry is being approximated within the blending region. Some work has been done on the effect of the size of the blending region on the loads and convergence rate [55]. For the SACCON, as the flap geometry is known, the blending process was done during the grid construction process. This was done by cutting the flap surfaces at either end, in the spanwise direction, and creating a surface between the flap and the wing. Between the flaps and the wings there is a gap of 1mm, this is surfaced over and used as part of the blending region. The original flap surfaces were cut at either end by 25% of the flap chord and this is used as a blending region. Surfaces were then constructed within this region to obtain continuity between the wing and the flap in the spanwise direction.

3.2.2 Grids and Computational Setup

A multi-block grid consisting of 260 blocks was generated using the ANSYS ICEM software package. The geometry was scaled using one metre as a unit length with the apex of the aircraft as the origin. The block topology on the surface of the SACCON, see Fig. 3.15a, was chosen so that each flap surface would be represented by a block face. This was done so that each flap can be deflected separately within the CFD code, e.g. to deploy a flap during an unsteady calculation. As a result of this there was no block edge associated to the surface discontinuity, which is therefore approximated by the cells that it passes over. There is an alternate topology which could have a block edge associated to the surface discontinuity, however, there are other issues which would arise as a result of this. There would be a kite-shaped block just above the wing tip and this is where we expect the vortex to be for a significant portion of the angle of attack range. The quality of the cells within this region would be significantly lower, decreasing the quality and convergence rate of the CFD solution in a critical region of the flow.

Also, the distance between the flap and the surface discontinuity is approximately 20 times bigger than the distance between the flap and the wing tip. This would require a significant amount of refinement in the region to prevent the cell expansion ratios from getting too big. As a result of this all parallel edges would also be affected, which, because of the kite-shaped block, would affect a large number of blocks causing unnecessary refinement.

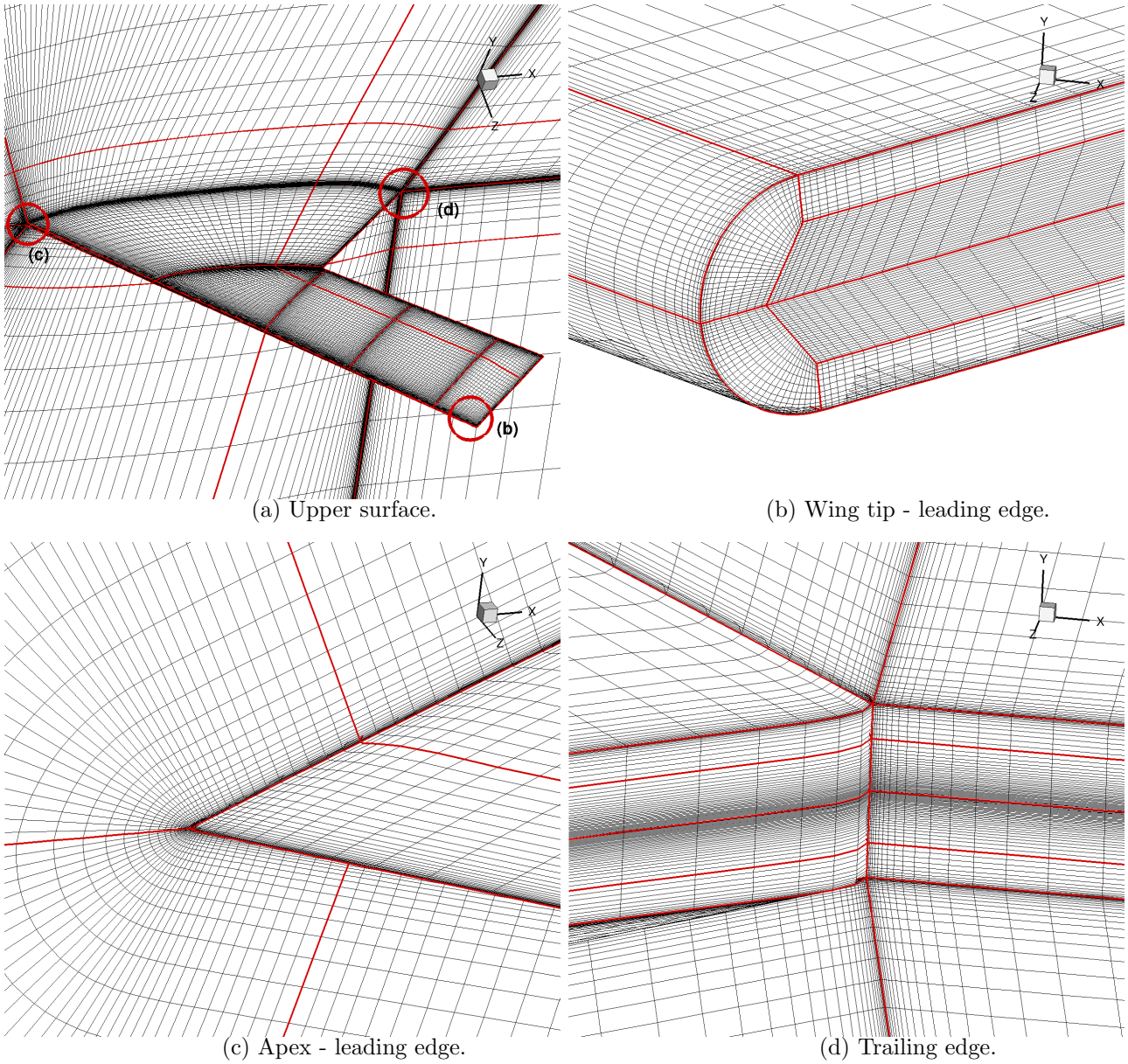

(a) Upper surface.

(b) Wing tip - leading edge.

(c) Apex - leading edge.

(d) Trailing edge.

Figure 3.15: Grid topology at key locations for the SACCON.

The grid has a C-topology at the leading edge see Fig. 3.15c and an O-topology at the wing tip see Fig. 3.15b. The farfield is approximately 20 chords away from the aircraft in every direction with a first cell spacing normal to surface of $c_{ref} \times 10^{-5}$. There are 124 cells in the chordwise direction and 488 cells in the spanwise direction with a total of just over 14 million cells. The grid density and expansion ratios in the chordwise, spanwise and normal directions were based on a grid built by D. Vallespin which was used for earlier work on this configuration [50, 56]. A grid refinement study was performed as part of this work demonstrating that this level of refinement is sufficient to obtain grid indepedent results. The simulations were performed on the supercomputer ARCHER, with this grid it took approximately one day for a steady state simulation on 72 cores.

The wind tunnel conditions for the experiments were a Mach number of 0.145 and a Reynolds number based on the reference chord of 1.585×10^6. The turbulence model used was the k-ω model with vortex correction, chosen based on the work done previously by D.Vallespin [56]. This limits the production of kinetic energy in regions of high vortical flow and increases the production of the dissipation rate to correct the amount of turbulent kinetic energy produced in the vortex core.

3.2.3 Results

For a qualitative understanding of the vortex structures that occur in the CFD solution as the angle of attack is increased, see Fig. 3.16. These are identified using the λ_2 criterion, a vortex identification technique developed by Jeong and Hussain [57]. A short description of the flow structure for this UCAV planform will follow, for more detail the reader is directed to [50, 51]. As the angle of attack is increased the wing tip vortices increase in size, this can be seen between Figs. 3.16a and 3.16b. A further increase in the angle of attack results in the onset point of the wing tip vortex moving inboard along the leading edge and vortices on either side of the body originating from the sharp nose become apparent. As the vortex moves inboard it starts to reduce the area of attached flow over the wing, Fig. 3.16c. Eventually the vortices merge and breakdown and the flow over the entire wing becomes separated, Fig. 3.16d.

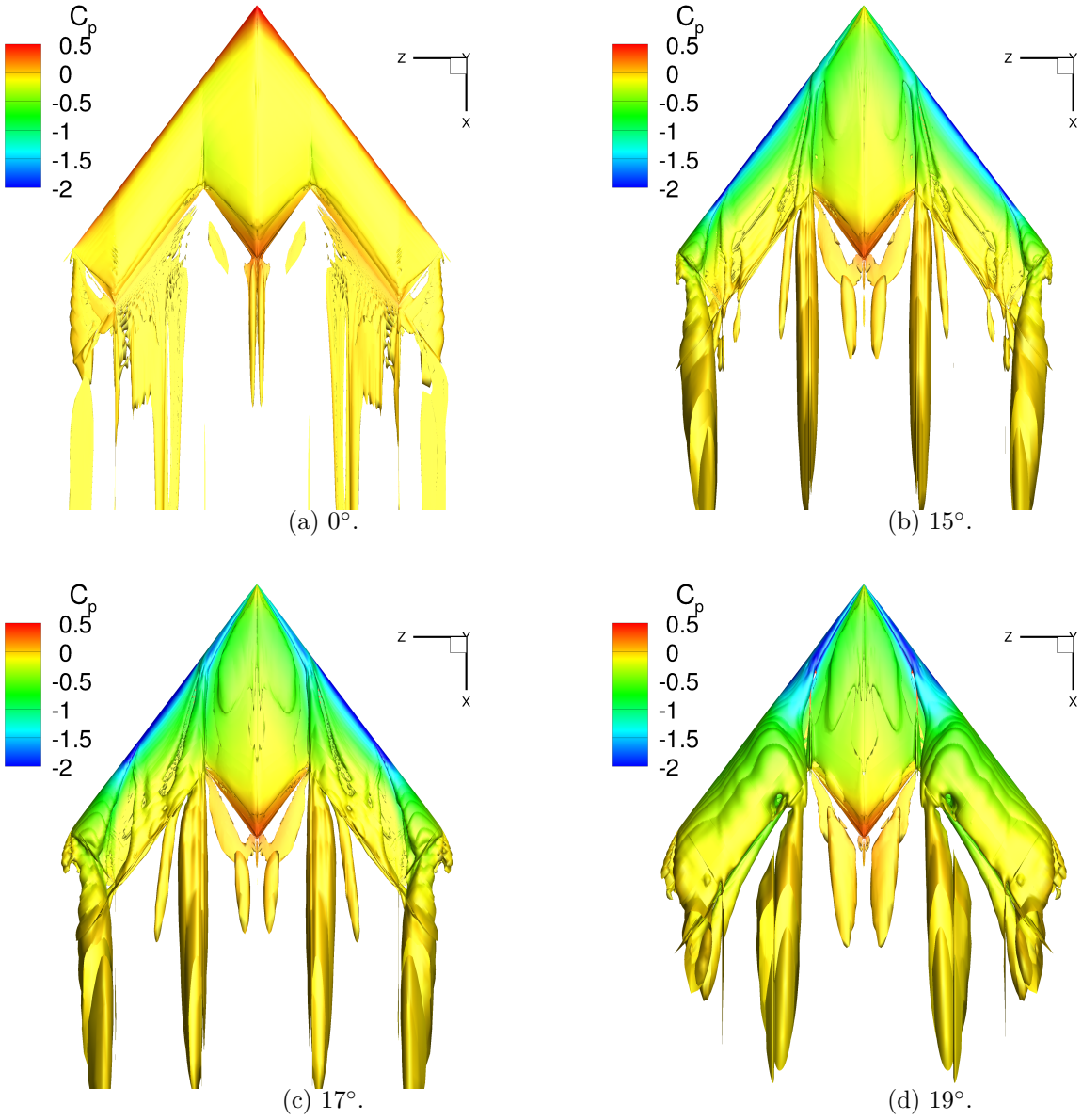

(a) 0°. (b) 15°.

(c) 17°. (d) 19°.

Figure 3.16: Iso-surfaces of the λ_2 criterion coloured with C_p for the SACCON at various angles of attack.

For the comparison of the computational and experimental integrated loads see Fig. 3.17. The lift coefficient, Fig. 3.17a, shows relatively good agreement for the attached part of the flow. In the non-linear region the computed lift shows a similar trend to the experiments, increasing lift with a reduction in slope. However the lift stops increasing at approximately 24° whereas the CFD predicts a continued

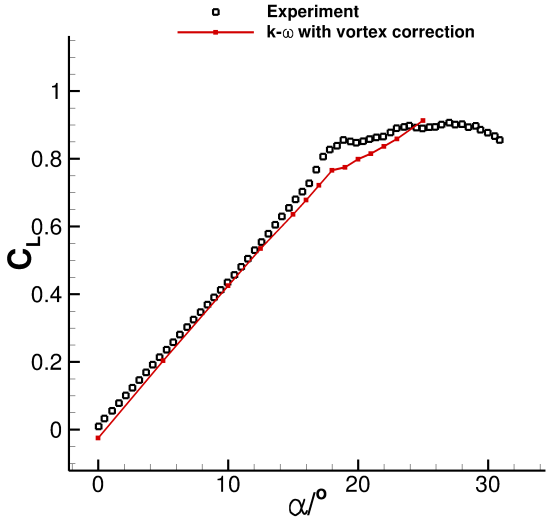

(a) Lift coefficient.

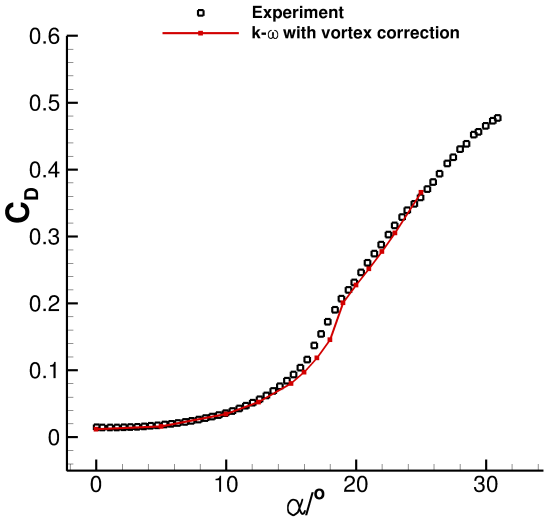

(b) Drag coefficient.

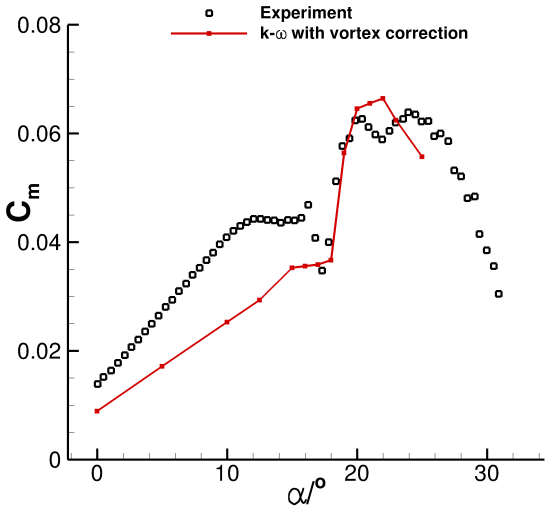

(c) Pitching moment coefficient.

Figure 3.17: Comparison of the computational and experimental integrated loads for the SACCON.

increase. Similarly the drag coefficient, Fig. 3.17b, shows good agreement until the flow separates. There is a slight underprediction between 16° and 18°, however the agreement between the computational and experimental results improves again after this. The discrepancy could be due to the fact that the surface discontinuity is being approximated and it is the angle range at which the wing tip vortex is passing

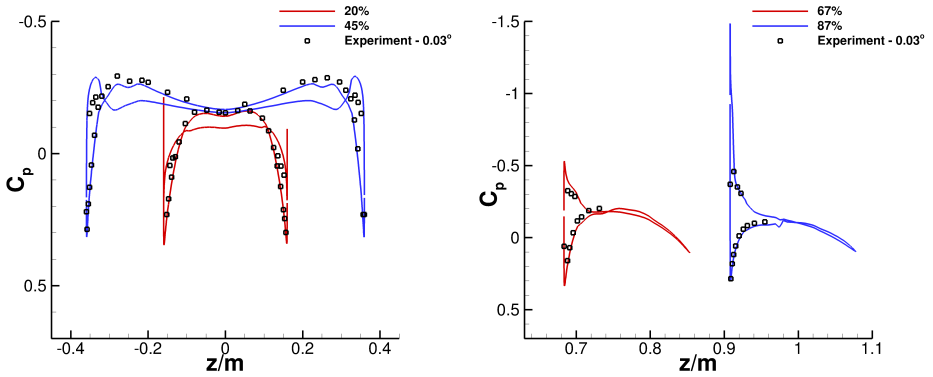

(a) 0° - body.

(b) 0° - wing.

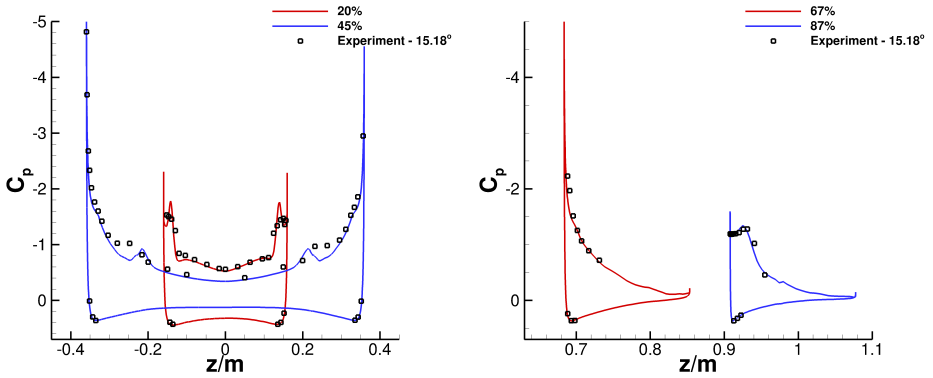

(c) 15° - body.

(d) 15° - wing.

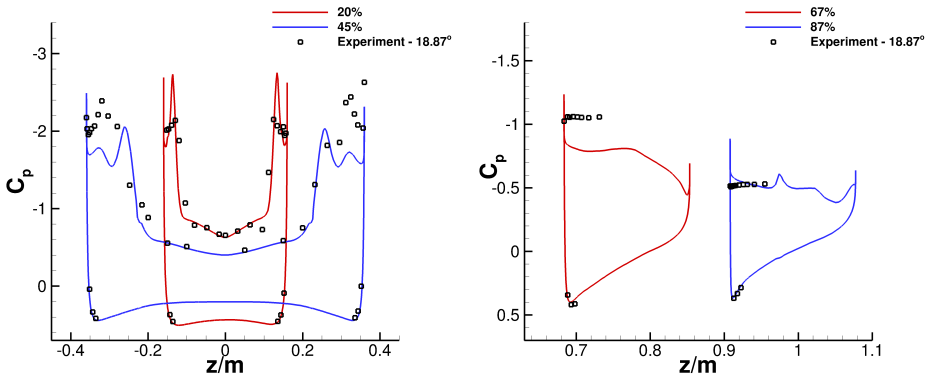

(e) 19° - body.

(f) 19° - wing.

Figure 3.18: Comparison of the computational and experimental integrated loads for the SACCON.

over it, see Figs. 3.16b and 3.16c. For the pitching moment coefficient, Fig. 4.28c, the lack of the sting causes a discrepancy in both the attached and separated regions of the flow. Work has been done [51]

to demonstrate that the inclusion of the sting accounts for this discrepancy. Also the initial dip at 16° is not captured by the CFD however the pitching moment does plateau. This is probably for the same reason as for the difference observed in the drag coefficient.

For the comparison of the surface pressures see Fig. 3.18. The CFD shows good agreement with the experimental results in the attached regime of the flow. The pressure coefficient on the upper surface is slightly underpredicted. As the angle of attack increases and the vortices increase in strength the difference between the computational and experimental results becomes more evident. Particularly in the areas beneath the vortices, see Figs. 3.18c and 3.18e between -0.16 and -0.12 on the 20% slice and between -0.3 and -0.2 on the 45% slice. These differences are partly due to the unsteady nature of the flow and the sting not being modelled. Inclusion of these aspects has been shown to increase the agreement in those areas [51].

3.2.4 UCAV Validation Summary

The computed aerodynamic loads from the CFD simulations show good agreement with the loads recorded in the wind tunnel experiments during the attached regime of the flow. There are a few discrepancies, such as the offset observed in the pitching moment coefficient throughout the angle of attack range. However, previous work done on this configuration has shown that the sting used to mount the model in the wind tunnel is responsible for these discrepancies. At the higher angles of attack where the vortices start to dominate the flow larger differences are seen between the experiment and computations. This is attributed mainly to RANS methods not being able to capture the unsteady nature of the flow and the behaviour of the vortices accurately as has been shown in previous work done on the configuration. An important point to make, is that the flow topology is predicted correctly throughout the angle of attack range and this is key in using the simulation to evaluate if the circulation control is effective. Further investigations of the effects of using different turbulence models and URANS for the SACCON with the conventional control surfaces have been conducted in [55]. The accuracy

obtained is sufficient to gain an understanding of whether the fluidic devices will be effective in providing control moments for such aircraft. If necessary at a later stage unsteady calculations or higher fidelity turbulence modelling can be used to gain a better understanding of the nonlinear part of the flow.

Chapter 4

SACCON with Circulation Control

The CFD solver has been validated using two cases, the SACCON UCAV and the CC-E0020EJ aerofoil. These have demonstrated that the solver is capable of predicting the separation point of the coanda jets, the pressure distribution over the wing, and to correctly predict the overall flow behaviour of a UCAV which exhibits highly nonlinear vortical flow. The next stage is the application of the CC devices to the SACCON to obtain an understanding of how they will perform on a swept wing planform. One of the purposes of the CC is to be used as a manoeuvre effector. There are two operations that are considered, one for generating primarily a rolling moment and the other for a yawing moment. For these types of configurations the pitching moment is generated using thrust vectoring. The rolling is performed by using opposite slots on either wing, for example, using the upper slot on the right wing and the lower slot on the left would cause the plane to roll to the left. For yawing both upper and lower slots are used at the same time to reduce the drag for one of the wings, creating the yawing moment. The SACCON is used mainly because of the amount of experimental data available with and without the conventional control surfaces, making it an ideal case for comparison purposes. Also, even though it has been designed to have a particularly challenging flow, the general flow behaviour is typical of low sweep UCAV planforms. This will make it possible to understand under what conditions the CC can be effective as a manoeuvre effector and what problems it may have.

4.1 2D Analysis in Preparation for CC Modifications

In preparation for modifications to the trailing edge of the SACCON's wings the aerofoil section at the root of the wing was used to determine the jet modifications. The performance of the original and modified aerofoil were then compared to determine the effect of the modifications while the coanda jets were not being used. Also, the effectiveness of conventional control surfaces was determined to see the massflow and coanda sizing required to match them. The coanda radius and slot height were chosen based on work done by Stephen Michie at the University of Manchester [58]. The product of this work was a design methodology for CC effectors, focusing on low observable UAVs. The lift generated by the CC is a function of the radius of the coanda surface and the momentum coefficient used, increasing either parameter increases the lift. The work demonstrated that a coanda radius as small as 0.5% of the chord could be used successfully to augment the lift minimising the drag penalty of the CC device. As a result, this was the size that was chosen for the following work.

The initial trailing edge thickness of the aerofoil was not enough for the CC device. Therefore part of the trailing edge, approximately 2.05% of the chord, was removed and replaced with a dual CC system, consisting of a semi-circular trailing edge and 2 slots. The coanda radius is 0.5% of the chord, the slot height is 10% of the coanda radius and the slot lip is 5% of the coanda radius. The conventional control surface was made by rotating the trailing edge, 25% of the chord length, by 20 degrees and then blending it with the rest of the aerofoil. The parameters for the blended flap were chosen to match the conventional control surfaces for the SACCON DLR-F19 from the experimental setup. See Fig. 4.1 for an overall view of the original aerofoil section with the modifications and the blended flap.

4.2 Grids and Computational Setup

The grid for the aerofoil was generated using the ANSYS ICEM software. It has a C-topology at the leading edge and an H-topology at the trailing edge consisting of 9 blocks, with a total of 36,419 cells.

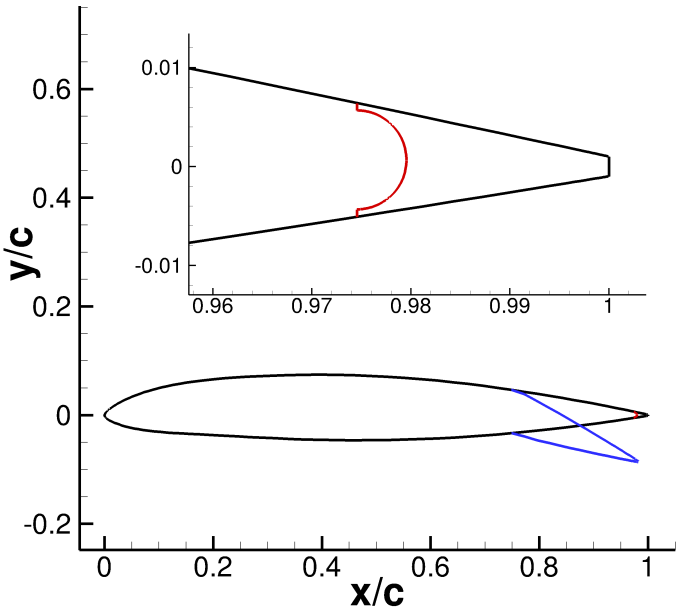

Figure 4.1: CC modifications(red) and the blended flap(blue) for the 2D aerofoil section from the root of the wing with a close up of the trailing edge.

The first cell spacing normal to the aerofoil surface is 1×10^{-5} and the farfield is 10 chord lengths from the surface. For the modified aerofoil a grid with a C-topology at the trailing edge was constructed using the same blocking as the previous grid for the leading edge and altering the blocks at the trailing edge. This increases the total number of blocks to 12, not including the plenum chambers, with a total of 43,112 cells. Similarly, the grid for the aerofoil with the conventional control surface was constructed by using the first grid. The block edges normal to the trailing edge were moved to maintain as much orthogonality as possible. This way all the grids have the same topology and grid density around the leading edge of the aerofoil and up to where the flap begins, allowing for comparison between the different cases without the grid causing any discrepancies. See Fig. 4.2 for the grid for the unmodified aerofoil and a close-up of the trailing edge with and without the modifications. A second grid with double the number of cells along the coanda surface was also constructed to check for grid independent solutions.

The freestream conditions used for all the calculations were a Mach number of 0.2 and a Reynolds

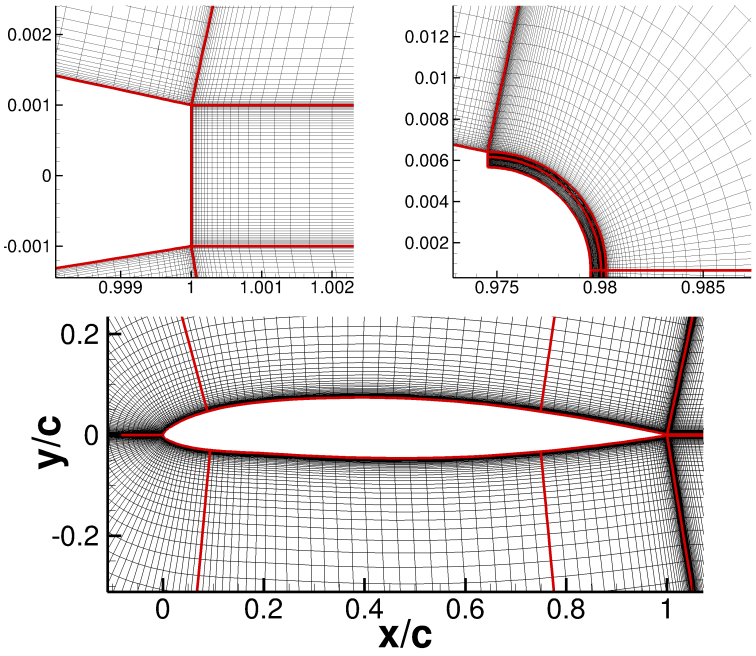

Figure 4.2: Plot showing the grid used for the aerofoil taken from the root of the SACCON's wing with close-ups of the trailing edge for both the modified and unmodified aerofoil.

number of 2.2×10^6 based on the c_{ref} of the DLR-F19. The turbulence model used was the k-ω model based on the validation work done in Chapter 3. All the simulations were run as steady-state calculations, unless mentioned otherwise. The angle of attack ranges used are from zero until the loads from the CFD solutions were unable to converge, this occurs when there is significant flow separation over the upper surface.

4.3 Results

All the aerodynamic coefficients have been scaled with the original chord length as the purpose of this analysis is to quantify the effect of the CC on an aerofoil section relative to a flap. Initially the CC aerofoil was tested at an angle of 0° with a range of NPR to determine what is needed to match the C_L generated by the aerofoil with the blended flap, see Figs. 4.3a and 4.3b. Both grids predict the jet attaching to the coanda surface at a NPR of 1.27 which corresponds to a C_μ of 0.0096. There appears

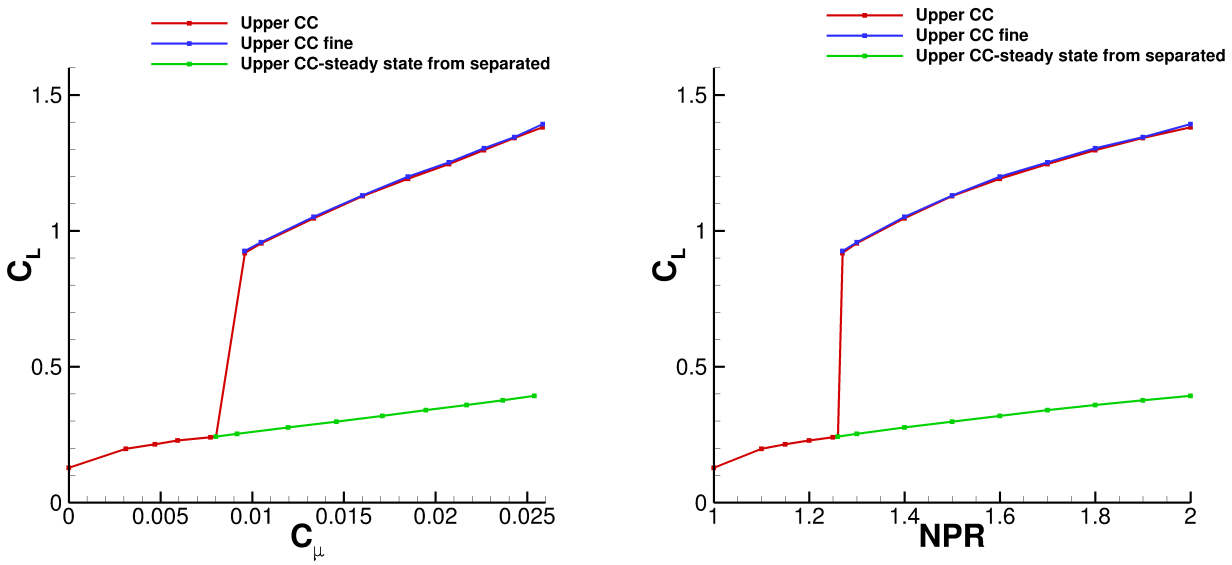

(a) C_L vs. C_μ for the CC aerofoil with the upper slot in use.

(b) C_L vs. NPR for the CC aerofoil with the upper slot in use.

Figure 4.3: Lift coefficient for the CC aerofoil at a range of NPR.

to be a jump in the blowing coefficients used in Fig. 4.3a. This was because as soon as the coanda jet becomes attached there is a decrease in the pressure around the slot which causes an increase in the jet velocity and hence the blowing coefficient. At lower pressure ratios the solution for the fine grid does not converge and the C_l values oscillate between 0.15 and 0.22. This suggests there is unsteadiness in the CFD solutions while the coanda jet is detached. The purpose of the CC is to be used as a manoeuvre effector. So if it no longer works (i.e. the jet is detached) and the load is significantly below the required value to perform a manoeuvre, the value of the lift coefficient is of little interest to us. Therefore as long as the CFD is correctly predicting whether the jet is attached we do not need to be able to predict the value of the lift coefficient with accuracy while the jet is separated. From these results a NPR of 1.5, corresponding to a C_μ of 0.0160, was chosen for the comparisons with the flap. The coarse grid will be used for the rest of the results presented.

During later unsteady simulations it was observed that a separated jet would not re-attach as the NPR increased. Therefore the simulations for a NPR of 1.3 and higher were rerun from converged solutions

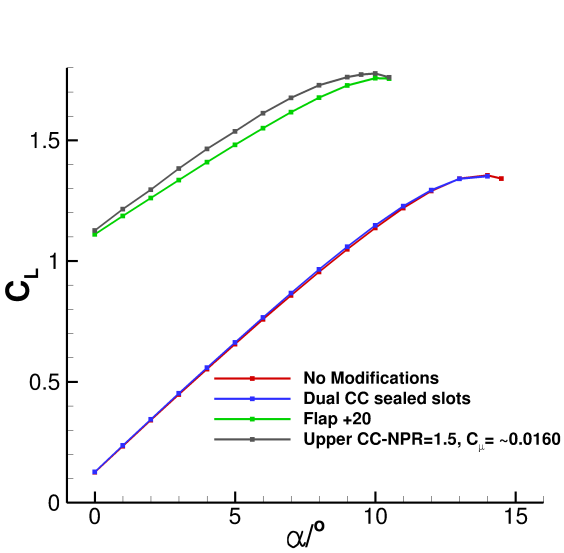

(a) Lift coefficient.

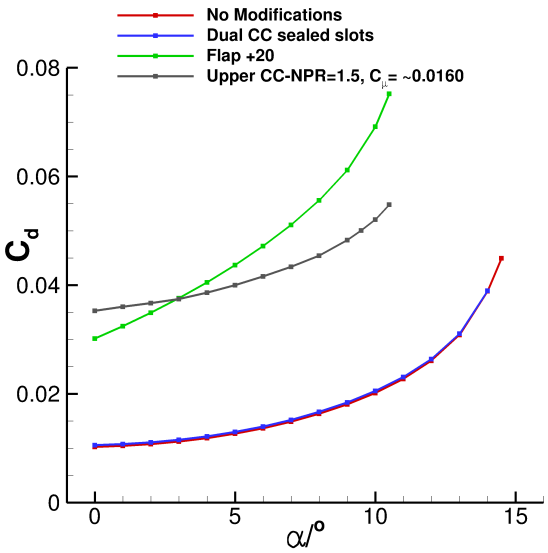

(b) Drag coefficient.

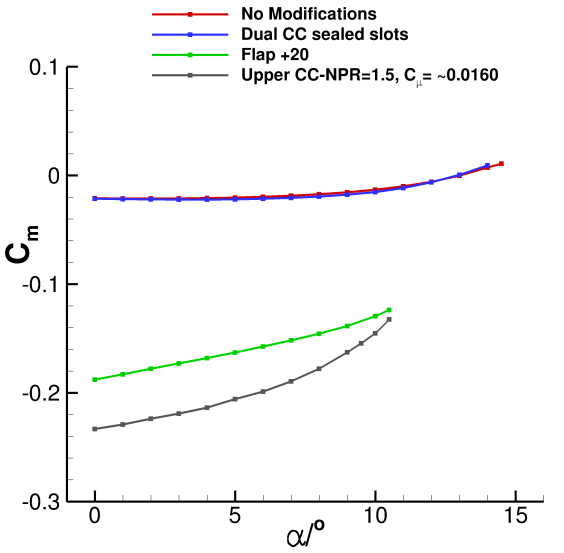

(c) Pitching moment coefficient.

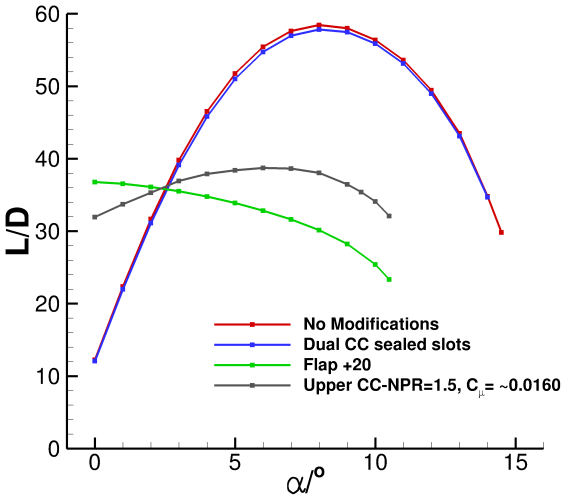

(d) Lift/Drag.

Figure 4.4: Comparison of the aerodynamic coefficients against angle of attack for the various aerofoils.

with a slightly lower pressure ratio. This is done to determine whether the converged CFD solution depends on the initial conditions. The NPR was incremented using values of 0.1, and each step was then run using the solution from the previous step. As can be seen from Fig. 4.3b for the higher pressure ratios, the jet remains detached when using a separated jet with a slightly lower pressure ratio as an

initial condition.

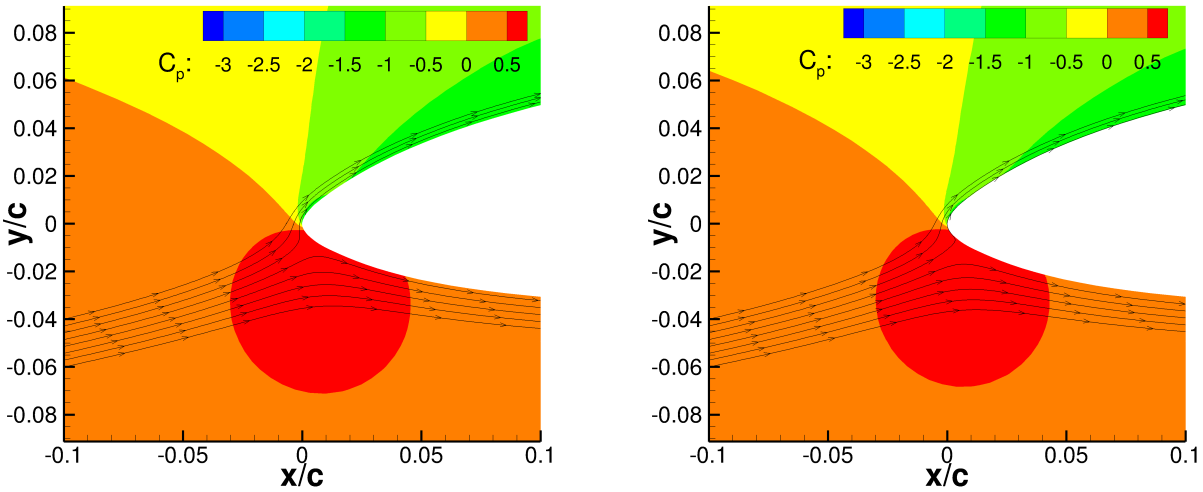

(a) Blended flap at 0°.

(b) CC at 0°.

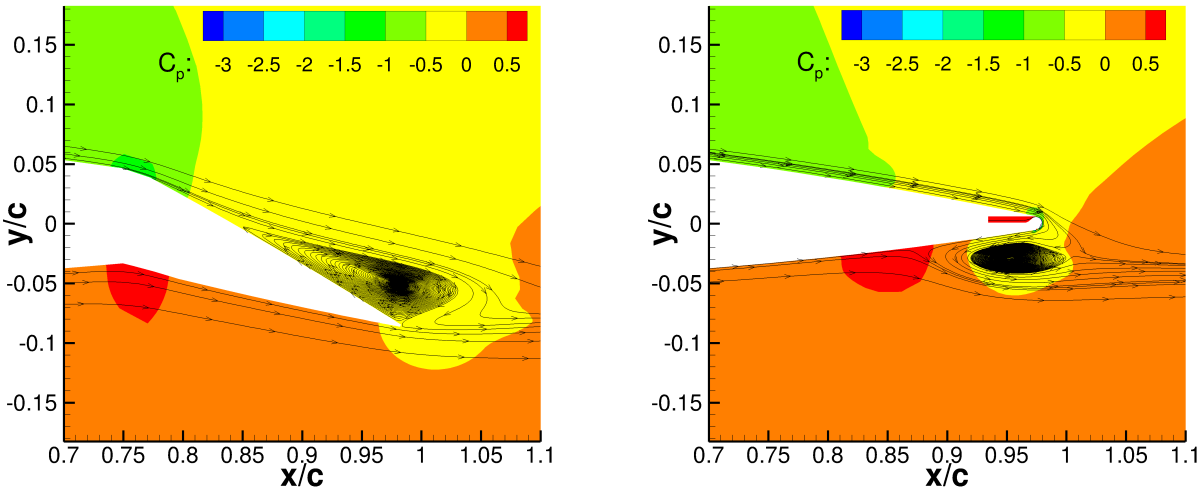

(c) Blended flap at 4°.

(d) CC at 9°.

Figure 4.5: Comparison of the flowfield at the leading and trailing edges of the aerofoil for the blended flap and CC at various angles of attack.

The integrated loads obtained from the CFD simulations are shown in Fig.4.4. The effects of the modifications to the lift and pitching moment coefficient curves of the aerofoil are neglible. There is a very slight increase in the drag coefficient at the low angles of attack due to the increased thickness of

the trailing edge. However, as the angle of attack was increased the difference between them decreases. Both the CC and the blended flap have a similar overall effect on the aerodynamic coefficients. The slope of the lift coefficient curve is greater for the fluidic device relative to the flap, making it slightly more effective at producing lift at the higher angles of attack. They both predict peak lift coefficient values at a similar angle, however, the steady state computations do not converge after an angle of attack of 10°. Also, the blowing coefficient decreases slightly as the angle is increased. This is because the pressure at the slot increases as the angle is increased, causing a decrease in the velocity of the jet. At 0° the CC produces 15% more drag however, the gradient of the curve for the flap is greater and by 3° they are already producing the same value. This occurs because the flow starts to separate on the flap, Fig.4.5c, very early on creating the rapid increase in drag. In contrast to this, the CC remains attached until higher angles of attack, Fig.4.5d, with the drag being generated primarily by the low pressure jet travelling around the trailing edge. The pitch down moment is greater for the fluidic device at all angles of attack, however again the slope is greater for the flap. The leading edge stagnation point and pressure contours are almost identical for the CC and blended flap, Figs. 4.5a and 4.5b. The difference in the pitch moment curves occurs as a result of the differences in the flow at the trailing edge. For the flap the maximum pressure on the lower surface occurs at the point of rotation, $x/c = 0.75$, for the flap, Fig.4.5c. For the CC it occurs just before the separation point of the jet at approximately $x/c = 0.85$, Fig.4.5d. Also, the high speed jet causes a very large pressure drop in the area surrounding the slot. This is because the coanda jet, being a relatively low massflow high speed jet, causes a very large pressure drop at the trailing edge which has a limited effect on the overall flowfield. Whereas the pressure changes caused by the flap is spread more evenly over the entire surface of the aerofoil.

4.4 Steady State Simulations Summary

2D analysis has been done on a cross-section of the SACCON's wing to determine the sizing and momentum requirements of the trailing edge CC device. The initial size of 0.5% of the coanda radius

with a slot height of 5% of the coanda radius was able to provide the same lift augmentation as a blended flap deflected at 20° at a NPR of 1.5. There are slight differences in the drag produced and in the pitching moment behaviour which may have adverse effects on the handling qualities of the aircraft. However, these issues can be investigated when the devices have been tested on the 3D planform as the swept wing could cause significant differences in the behaviour of the CC. These results show that in two dimensional flows, the CC effects the overall flowfield in a very similar manner to the blended flap. This also indicates that they could potentially be used as a replacement for conventional control surfaces without having to alter existing stability and control methodologies. Therefore the parameters stated above will be used on the SACCON.

4.5 Unsteady Simulations and Dynamic Behaviour

This aerofoil section was also used to investigate the unsteady behaviour of the coanda jets. Changes were made to the boundary condition that was implemented into PMB to allow the NPR to change during an unsteady simulation. The NPR was prescribed at each time step as part of the unsteady input file with the rest of the unsteady parameters. A first case was run from a steady-state converged solution with the plenum chamber at freestream pressure and the NPR at 1.5. This was done to determine how long it will take for the jet to become attached and to get an initial idea of the time step that is required for time accuracy. A variety of dynamic test cases were run, these involved oscillations in the angle of attack and NPR/flap deflection angle. Initially each parameter was varied individually to isolate the behaviour observed. The parameter range and reduced frequency of the oscillations were also varied to determine what the observed behaviour depends on. For the comparisons between the blended flap and the circulation control, the flap deflection angles were chosen to approximately match the maximum/minimum lift predicted by the steady-state simulations. Finally, a couple of cases involving coupled oscillations were simulated to investigate if any other effects were observed. The reduced frequencies were chosen to include a mix of cases involving quasi-steady and unsteady aerodynamics. Typically, a value below 0.05

corresponds to quasi-steady behaviour and above that to unsteady behaviour. The angle of attack range and the NPR/flap deflection angle for each case run are shown in table 4.1. For all of these cases the oscillation cycles begin at $T = 110$, this is because of the way they are initialised, which is case specific.

Case	Angle of Attack	Flapdeflection/NPR	Reduced Frequency
1 (jet)	0	$1.5 + 0.2 \times sin\left(\frac{\pi(T-110)}{50}\right)$	0.0314
2 (flap)	0	$20 + 5 \times sin\left(\frac{\pi(T-110)}{50}\right)$	0.0314
3 (jet)	0	$1.5 + 0.2 \times sin\left(\frac{\pi(T-110)}{10}\right)$	0.1571
4 (flap)	0	$20 + 5 \times sin\left(\frac{\pi(T-110)}{10}\right)$	0.1571
5 (jet)	0	$1.5 + 0.2 \times sin\left(\frac{\pi(T-110)}{2}\right)$	0.7854
6 (jet)	0	$1.3 + 0.2 \times sin\left(\frac{\pi(T-110)}{50}\right)$	0.0314
7 (jet)	0	$1.5 + 0.45 \times sin\left(\frac{\pi(T-110)}{50}\right)$	0.0314
8 (jet)	0	$1.3 + 0.2 \times sin\left(\frac{\pi(T-110)}{10}\right)$	0.1571
9 (jet)	0	$1.5 + 0.45 \times sin\left(\frac{\pi(T-110)}{10}\right)$	0.1571
10 (jet)	$5 + 5 \times sin\left(\frac{\pi(T-110)}{100}\right)$	1.5	0.0157
11 (jet)	$7 + 5 \times sin\left(\frac{\pi(T-110)}{100}\right)$	1.5	0.0157
12 (jet)	$10 + 5 \times sin\left(\frac{\pi(T-110)}{100}\right)$	1.5	0.0157
13 (jet)	$5 + 5 \times sin\left(\frac{\pi(T-110)}{30}\right)$	1.5	0.0524
14 (jet)	$7 + 5 \times sin\left(\frac{\pi(T-110)}{30}\right)$	1.5	0.0524
15 (jet)	$10 + 5 \times sin\left(\frac{\pi(T-110)}{30}\right)$	1.5	0.0524
16 (jet)	$10 + 5 \times sin\left(\frac{\pi(T-110)}{30}\right)$	$1.5 + 0.2 \times sin\left(\frac{\pi(T-110)}{10}\right)$	0.0524/0.157
17 (jet)	$10 + 5 \times sin\left(\frac{\pi(T-110)}{50}\right)$	$1.5 + 0.2 \times sin\left(\frac{\pi(T-110)}{10}\right)$	0.0314/0.157
18 (jet)	$5 + 5 \times sin\left(\frac{\pi(T-110)}{30}\right)$	$1.5 + 0.2 \times sin\left(\frac{\pi(T-110)}{10}\right)$	0.0524/0.157

Table 4.1: Dynamic cases $\left(T = \frac{u_\infty t}{c}\right)$.

4.6 Unsteady Results

The overall behaviour of the coanda jet is described in a qualitative manner. A couple of cases display an identical behaviour making it unnecessary to go through each case individually. Therefore, the key characteristics are discussed and the reader will be directed to the cases which demonstrate these

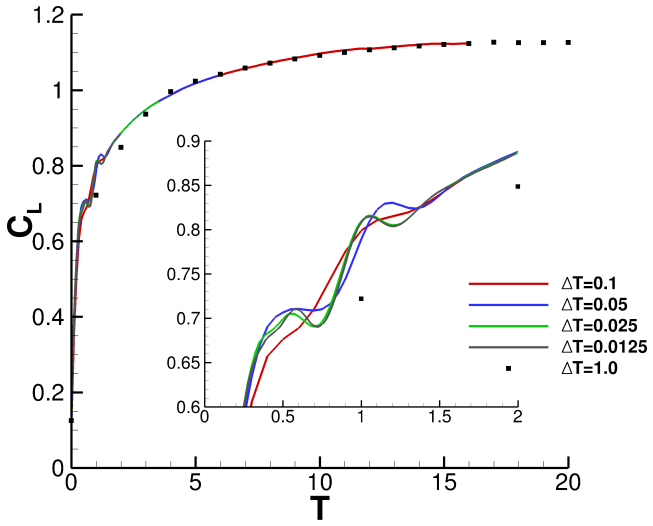

Figure 4.6: Unsteady coanda jet at NPR=1.5 with the plenum chamber at freestream pressure at T=0.

characteristics. Any effect the reduced frequency may have is also addressed. The simulation with the coanda jet turned on is explained in more detail as it demonstrates most clearly the effect of the size of the time step in the CFD solution. The load history of the lift coefficient is looked at to understand the state of the coanda jet (whether it is attached or not, the location of the separation etc.). This is because it is the simplest to interpret due to its sensitivity to these conditions.

4.6.1 Indicial Response

For the case with the coanda jet being turned on from the freestream pressure to a constant NPR of 1.5, see Fig. 4.6. With the appropriate scaling this is the equivalent of an indicial response. The lift increases rapidly and asymptotes exponentially towards the steady state value. This occurs as a result of the jet wrapping round the trailing edge and pushing the rear separation point upstream. As a result of this the leading edge stagnation point begins to move downstream. The time it takes to move to its steady state position can easily be captured with a coarse timestep. However, the movement of the stagnation point is not monotonic, it changes direction occasionally moving downstream, causing small oscillations in the lift, before continuing towards its final position. To capture these small oscillations a

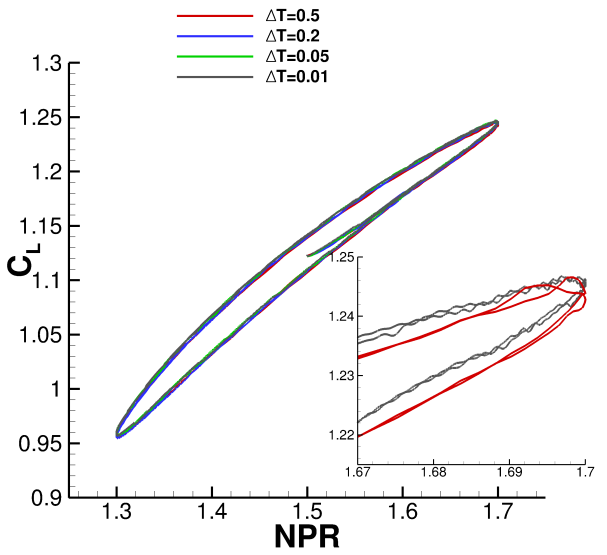

(a) NPR=$1.5 + 0.2 \times sin\left(\frac{\pi(T-110)}{50}\right)$.

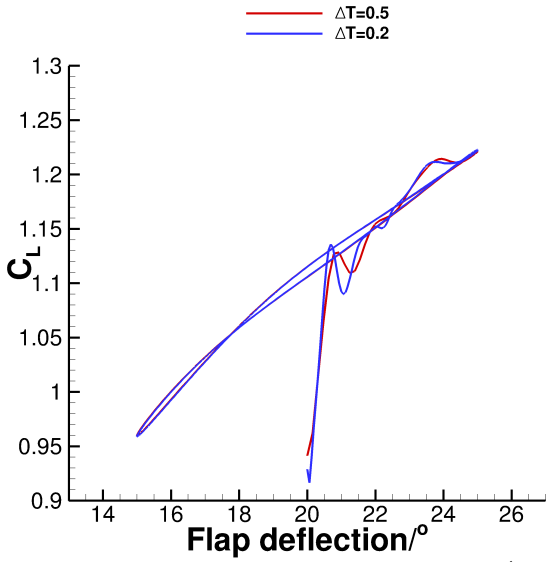

(b) Flap deflection=$20 + 5 \times sin\left(\frac{\pi(T-110)}{50}\right)$.

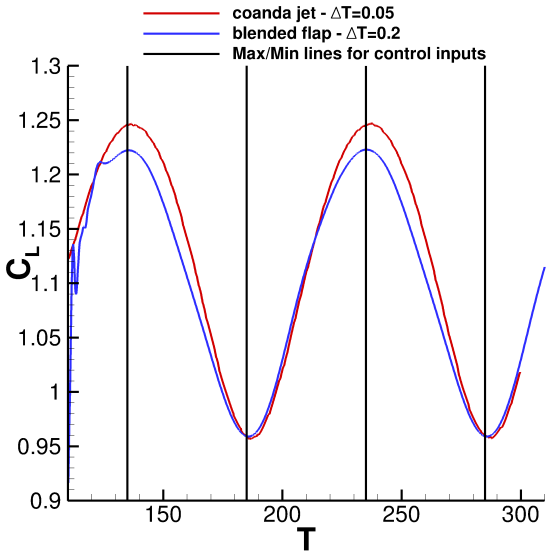

(c) Comparison of cases (a) and (b).

Figure 4.7: Oscillations of the control parameters at a reduced frequency of 0.0314.

much finer time step is required. Focusing on the section from $T = 0$ until $T = 1.5$, the various time step sizes predict these oscillations slightly differently, the time step of 0.1 almost completely misses them. We only start to see agreement between the two finest time steps, 0.025 and 0.0125. However for $t > 1.5$ there is very good agreement between all the step sizes except for the coarsest one of 1.0.

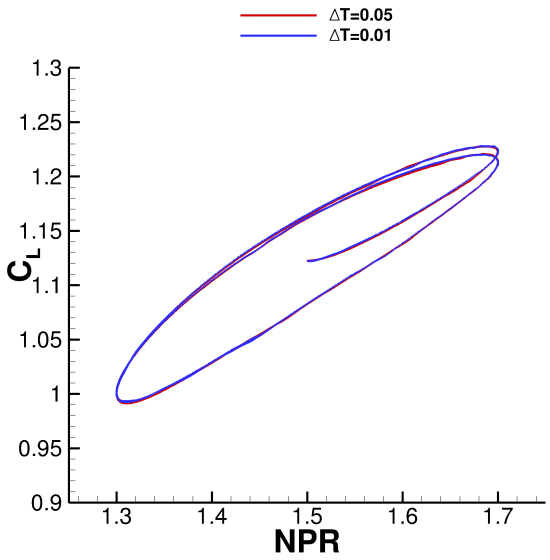

(a) NPR=$1.5 + 0.2 \times sin\left(\frac{\pi(T-110)}{10}\right)$.

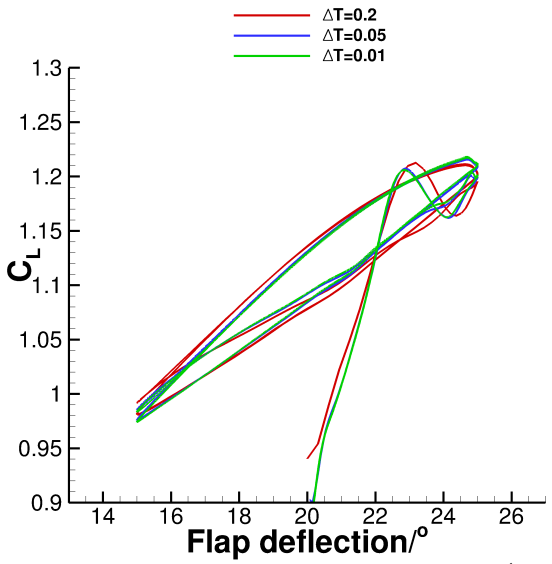

(b) Flap deflection=$20 + 5 \times sin\left(\frac{\pi(T-110)}{10}\right)$.

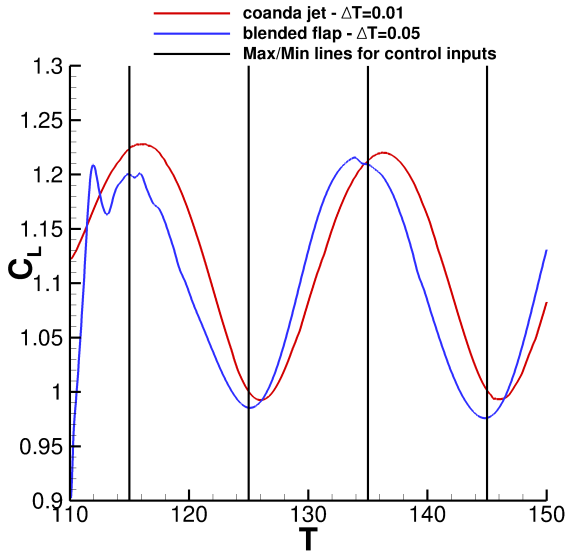

(c) Comparison of cases (a) and (b).

Figure 4.8: Oscillations of the control parameter at a reduced frequency of 0.1571.

4.6.2 Hysteresis

One of the key characteristics of the coanda jet's behaviour is that there is significantly more hysteresis relative to the blended flap, when adjusting the control parameter. This can be seen in cases 1 to 4 which are shown in Figs. 4.7 and 4.8. Changing the control parameter for the flap creates a geometric change

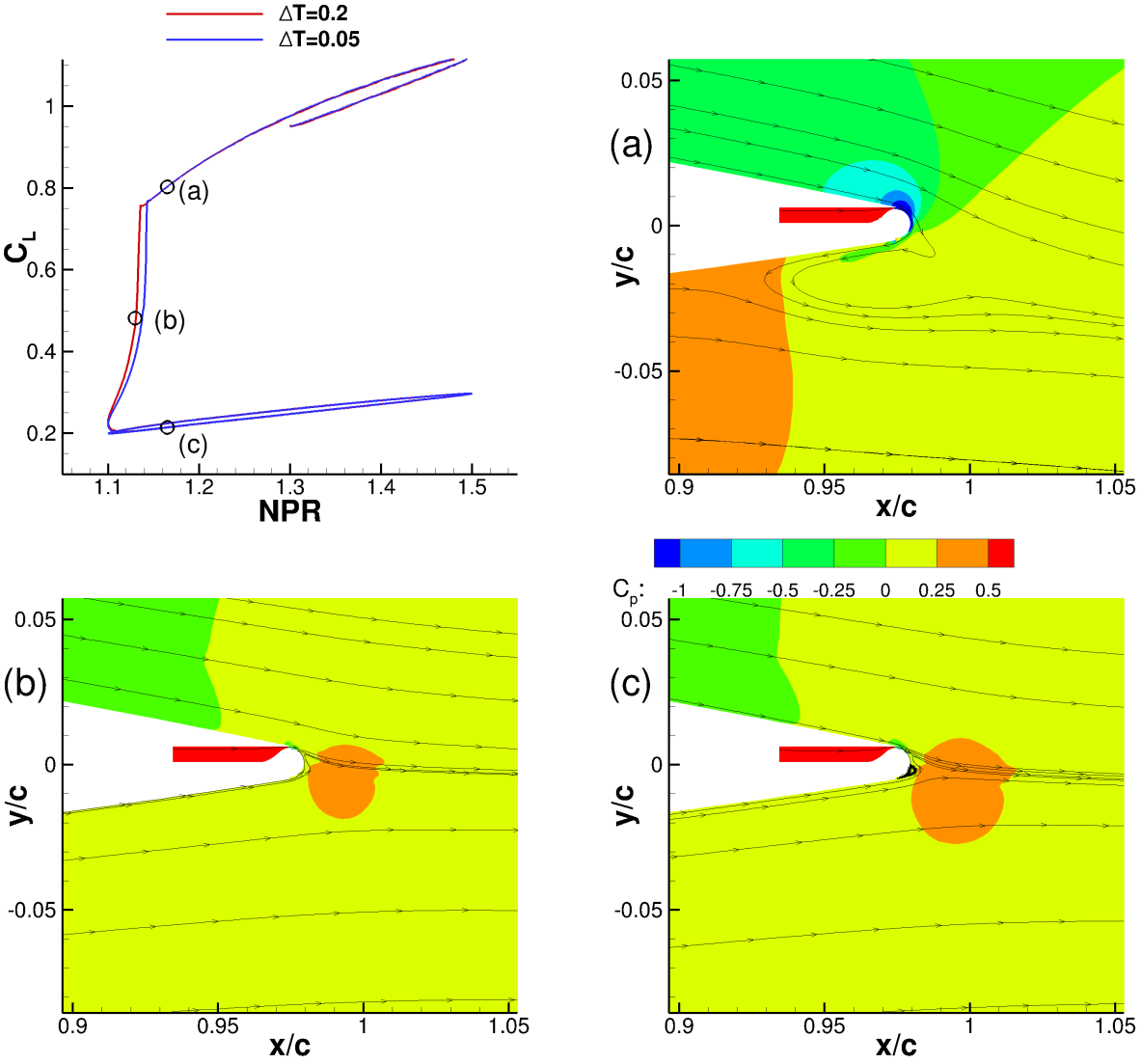

Figure 4.9: Flowfield plots demonstrating the jet separation due to NPR oscillations.

which forces the flow to adjust almost instantaneously. A change in the NPR leads to a movement of the trailing edge separation point which takes longer to occur. At a reduced frequency of 0.0314, Fig. 4.7a, some hysteresis is already clear for the coanda jet. In contrast to this the blended flap results, Fig. 4.7b, appear to be quasi-steady, which is to be expected as unsteady effects usually become important for reduced frequencies greater than 0.05, as a general guideline. At the higher reduced freuency of 0.1571, Fig. 4.8b, there is some flow separation behind the flaps, increasing the hysteresis at high deflection

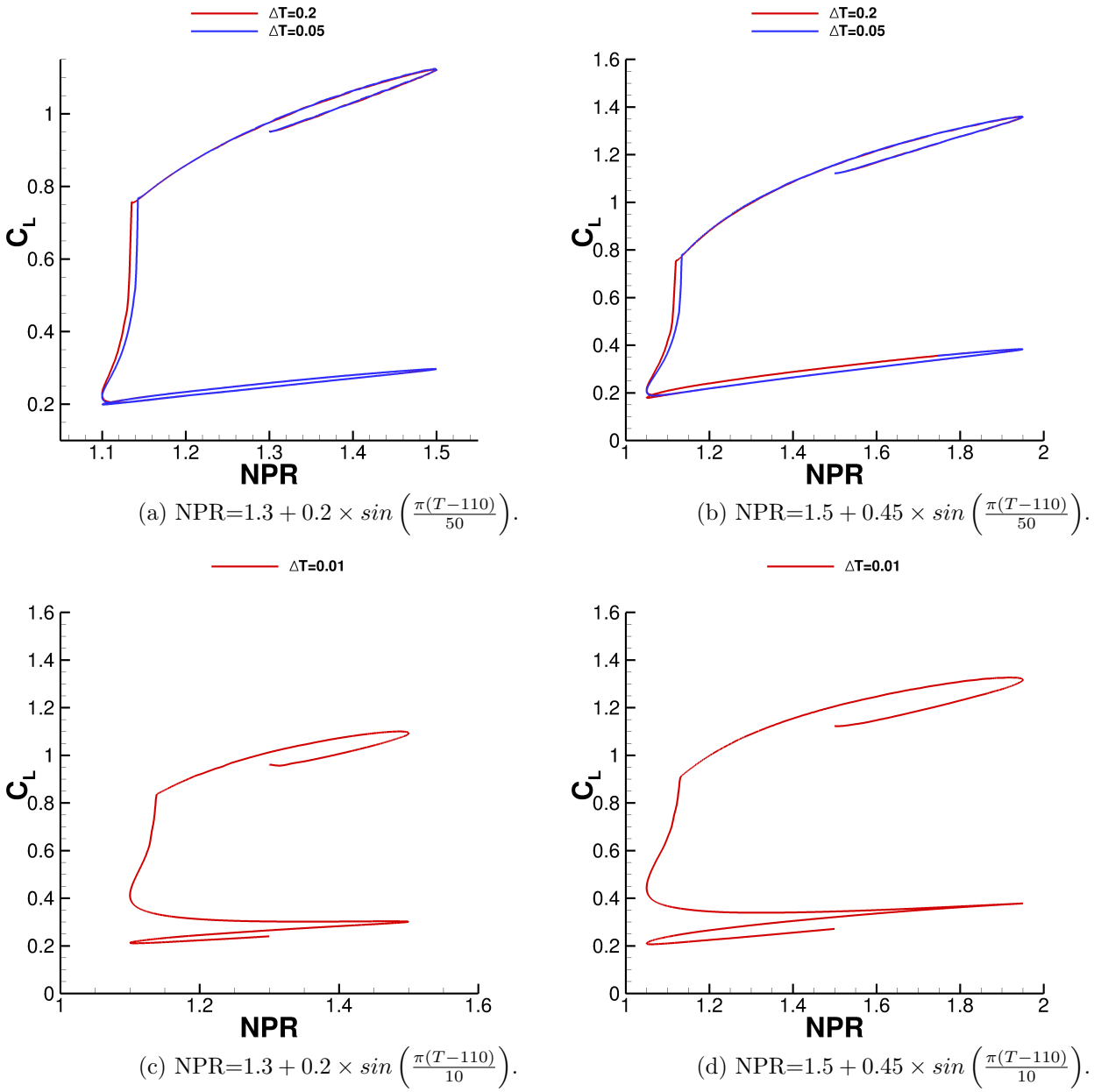

(a) NPR=$1.3 + 0.2 \times sin\left(\frac{\pi(T-110)}{50}\right)$.

(b) NPR=$1.5 + 0.45 \times sin\left(\frac{\pi(T-110)}{50}\right)$.

(c) NPR=$1.3 + 0.2 \times sin\left(\frac{\pi(T-110)}{10}\right)$.

(d) NPR=$1.5 + 0.45 \times sin\left(\frac{\pi(T-110)}{10}\right)$.

Figure 4.10: Cases involving oscillations in the NPR for two NPR ranges and two reduced frequencies.

angles and causing a dip before the maximum control parameter is reached, Fig. 4.8c. The overall shape of the loop can be captured well by all the time steps used, however, the small oscillations caused by the continuous movement of the separation points can only be seen when using a very fine timestep, as discussed earlier.

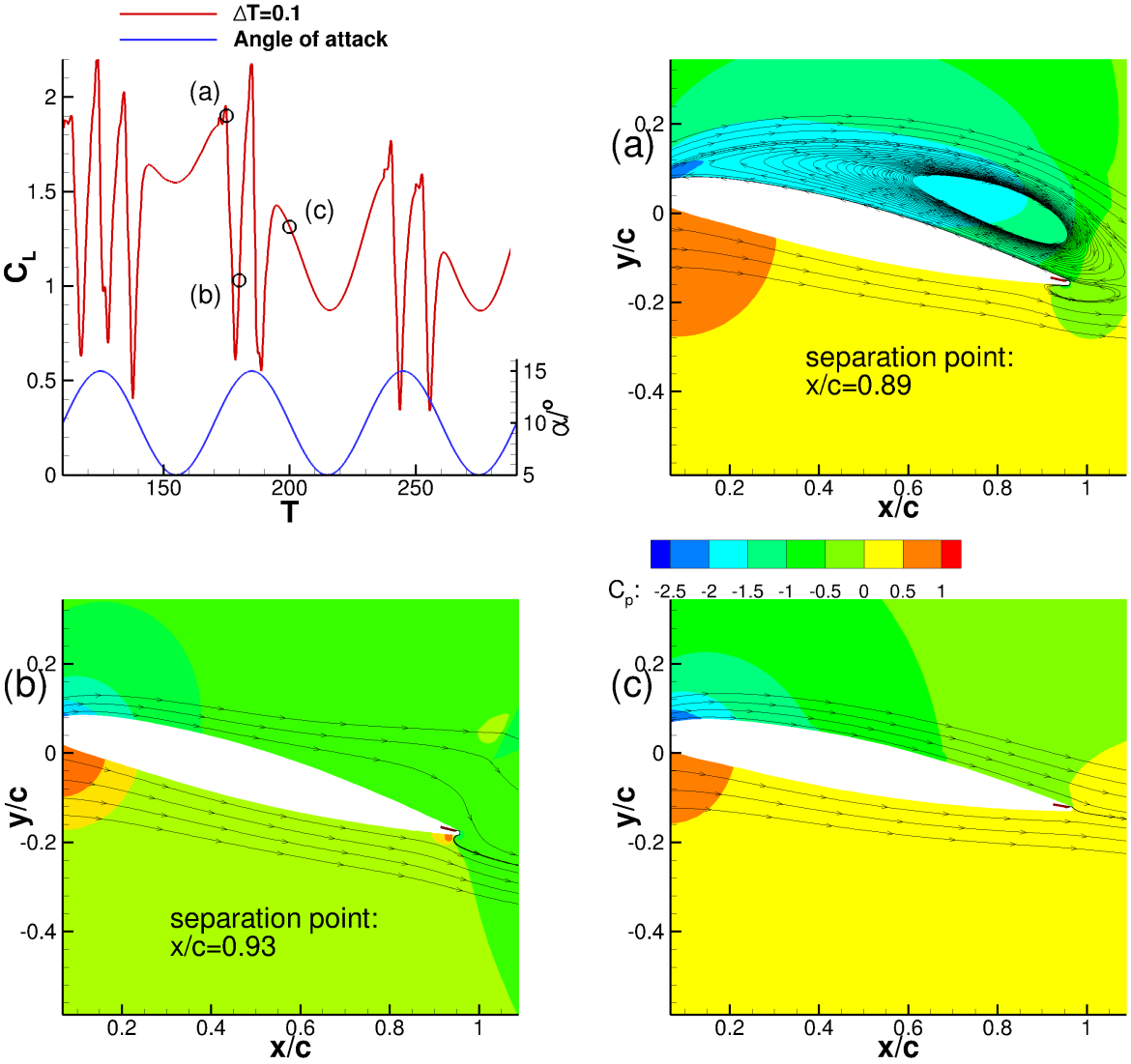

Figure 4.11: Flowfield plots demonstrating the jet separation due to AoA oscillations.

4.6.3 Jet Separation

Another characteristic of the coanda jet is that as the NPR drops below the attachment point, the jet separates and does not reattach when the NPR is increased again. This can be seen in cases 6-9, Fig. 4.10. A plot of the flowfield at different points during the oscillations can be seen in Fig. 4.9. The coarser timestep delays the separation, however, the agreement at all other points is very good. The reduced frequency seems to have very little effect on this detachment process, only delaying the separation to a

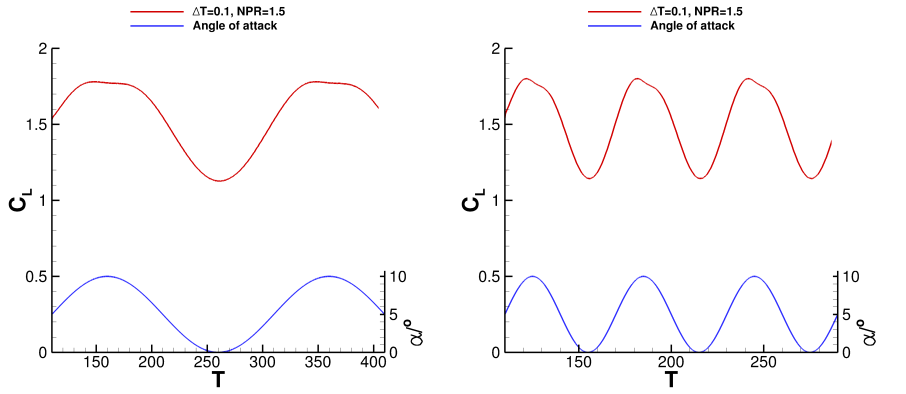

(a) $\alpha = 5 + 5 \times sin\left(\frac{\pi(T-110)}{100}\right)$. (b) $\alpha = 5 + 5 \times sin\left(\frac{\pi(T-110)}{30}\right)$.

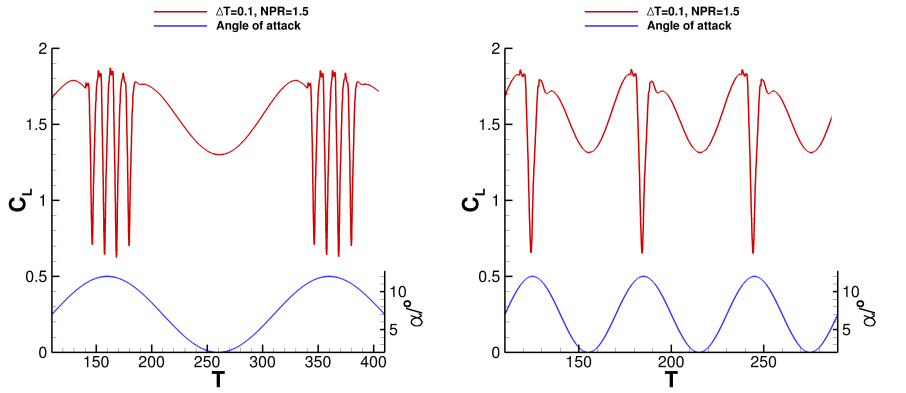

(c) $\alpha = 7 + 5 \times sin\left(\frac{\pi(T-110)}{100}\right)$. (d) $\alpha = 7 + 5 \times sin\left(\frac{\pi(T-110)}{30}\right)$.

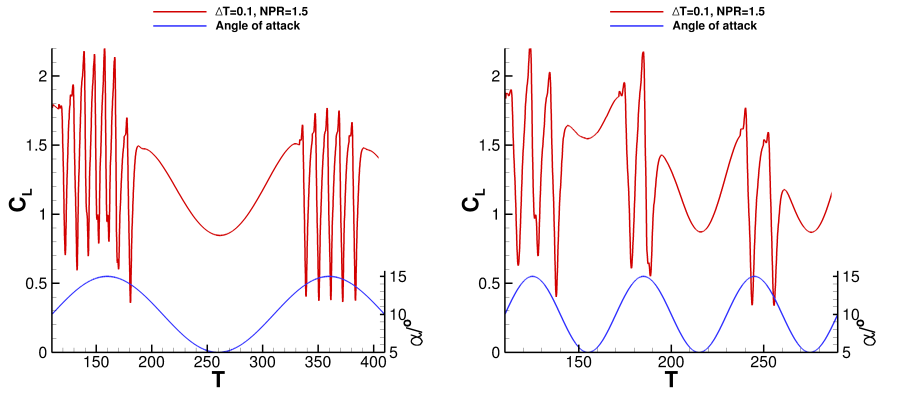

(e) $\alpha = 10 + 5 \times sin\left(\frac{\pi(T-110)}{100}\right)$. (f) $\alpha = 10 + 5 \times sin\left(\frac{\pi(T-110)}{30}\right)$.

Figure 4.12: Cases involving oscillations in the AoA with a constant NPR of 1.5.

slightly lower NPR. Also, a larger amplitude was used to see if the reattachment may occur at higher NPRs, however, this had no effect either, Figs. 4.10b and 4.10d. This led to another set of steady-state

computations which used solutions with the jet already turned on but separated as an initial condition instead of freestream conditions. The result of this can be seen in the previous section. This could potentially be a serious problem, as it suggests that if the jet were to separate during a manoeuvre the only way to get it to reattach would be to switch it off, and then back on again.

Cases 10-15 are all oscillations of the AoA with an increase in the average AoA at a constant NPR of 1.5, at two reduced frequencies, Fig. 4.12. The purpose of these was to determine the potential for the separation of the jet due to factors other than a low NPR. One thing to note in Figs. 4.12c, 4.12d, 4.12e and 4.12f is that the large oscillations in the lift coefficient occur as a result of dynamic stall. The cases in which it causes the jet to separate are the two that oscillate between 5° and 15°, Figs. 4.12e and 4.12f. Flowfield plots at different points during the oscillations are shown in Fig. 4.11 demonstrating how the jet separates. The separation occurs after the flow over the upper surface of the aerofoil is completely separated. This causes a large recirculation zone behind the aerofoil which entrains the coanda jets and drags the rear separation point downstream. As the aerofoil starts to pitch down the jet completely separates. At the higher reduced frequency of 0.157 the jet does not separate until the second cycle however, this could be because the CFD is not fully converged on the first cycle. The cases which oscillate between 2° and 12° also exhibit stall however the jet remains attached in this case, 4.12c and 4.12d.

4.6.4 Unsteady Simulation Summary

Unsteady simulations of sinusoidal oscillations of the AoA, NPR and flap deflection angle were performed at a range of reduced frequencies to understand the dynamic behaviour of the coanda jet. Certain key issues were identified, such as the jet separating when the aerofoil goes into stall. Also, the fact that the jet does not reattach, after it has separated, by increasing the NPR. This behaviour was independent of the reduced frequency of the oscillations.

4.7 SACCON with Circulation Control

The CAD model of the DLR-F19 was used as the basis for the CC modifications. The spanwise extent of the trailing edge CC device is the same as the inboard and outboard flaps used in the wind tunnel experiments. As the SACCON has a blunt trailing edge, the portion of the wing employing the CC needs to be changed into a circular trailing edge. The trailing edge of the entire model has been modified to allow for a C-grid topology, which will also increase the grid quality around the coanda surface. The modifications to the body were done by creating a semi-circular trailing edge and matching the gradients with the existing blunt trailing edge, see Fig. 4.13a.

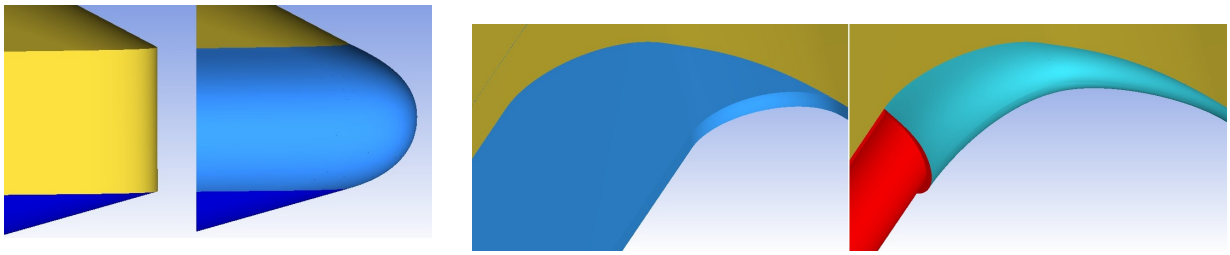

(a) The trailing edge of the body of the SACCON before and after the modifications are made.

(b) The junction between the wing and the body of the SACCON before and after the modifcations are made.

Figure 4.13: Screenshots of two key locations of the SACCON's trailing edge to show the modifications made for the CC device.

The modifications to the wings are done by truncating the existing wings at the required thickness, 98% of the c_{ref} at the root of the first control surface, creating a semi-circular trailing edge with upper and lower slots. A coanda radius of 0.5% and a coanda radius to slot height ratio of 10 was used, based on earlier work. The thickness of the wing decreases as the wing tip is approached, meaning either the trailing edge thickness will decrease or the wing has to be truncated further. To avoid reducing the wing area significantly and introducing further deviations from the baseline SACCON, the wing was truncated by 98% from the root of the first control surface to the wing tip. The coanda radius to slot height ratio was kept constant, with the maximum to minimum slot height ratio across the span being 1.33. For the parts of the wings which are not employing the fluidic devices, the trailing edge is modified in a similar

way to that of the body. At the junction between the wing and body the original surface between the body and the wing is cut to create a smooth transition from the trailing edge thickness at the body to the thickness required for the CC device, see Fig. 4.13b. See Fig. 4.14 for the CAD model before, 4.14a, and after, 4.14b, the modifications have been made.

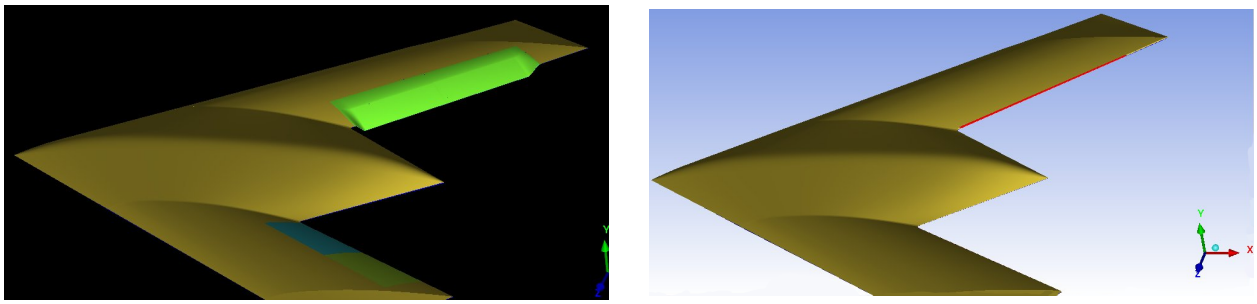

(a) Before the modifications with the ROB and RIB flaps at 20°.

(b) After the modifications, the coanda surface and slot are coloured red.

Figure 4.14: Screenshots of the full CAD model of the SACCON before and after the modifications.

A second configuration consisting of three slots, of equal width, on either wing was also constructed. This was done by creating a zero thickness wall within the plenum chamber to keep the grid a reasonable size. Having a wall with a thickness significantly increases the number of points needed in the spanwise direction to prevent the grid from expanding too rapidly. The purpose of this is an alternate way to control the circulation instead of varying the NPR, as the efficiency ($\frac{\Delta C_l}{\Delta C_\mu}$) of the device is not constant across the NPR. Each slot can then be turned on individually and to increase C_μ, multiple slots can be used at once. This also makes it possible to optimise the device for a particular NPR without having to worry about the off-design conditions, further increasing its efficiency and effectiveness. The slots will be referred to as inboard (IB), midboard (MB) and outboard (OB) from root to tip respectively.

There are two main CC operations which are of interest for manoeuvring aircraft. The first is an anti-symmetric operation, using the upper slots on one wing, increasing the circulation, and the lower slots on the other, decreasing the circulation. This operation is used to generate rolling moment. The second is using both upper and lower slots on one wing at the same NPR to reduce the wing's drag,

producing a yawing moment.

4.7.1 Grid and Computational Setup

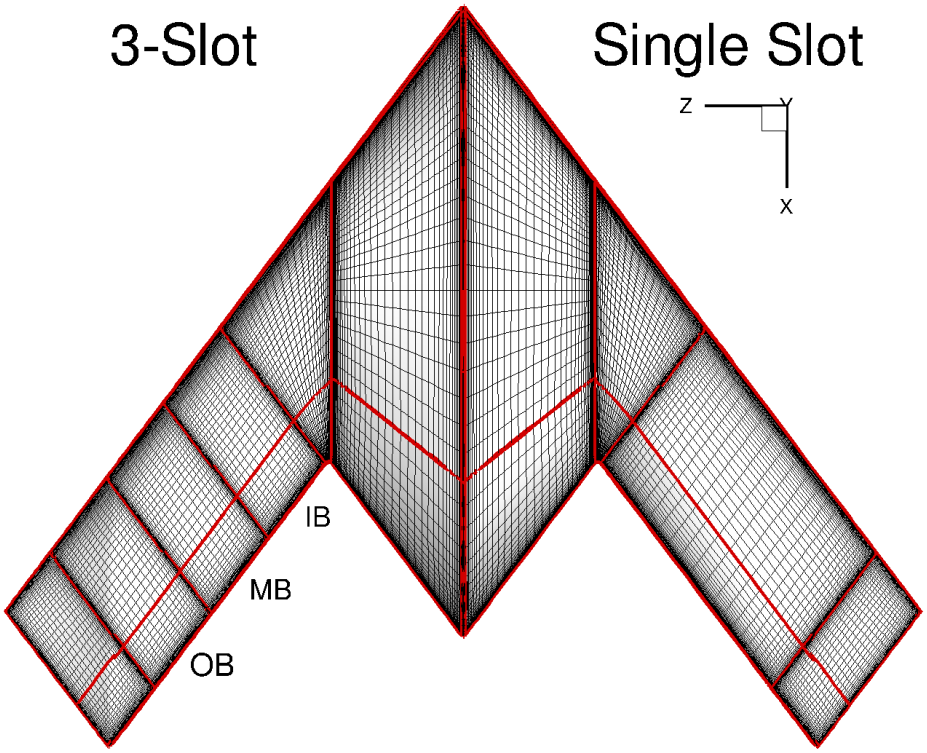

Figure 4.15: The surface grid for the SACCON employing CC. The left half corresponds to the 3-slot configuration and the right half corresponds to the single slot configuration.

The grid for the SACCON with the CC device uses the same number of cells in chordwise, spanwise and normal directions as for the F19 grid, where the geometry is the same. At the trailing edge the refinement has been chosen based on experience with the two-dimensional CFD validation. The grids for the single slot and three slot configuration have a total of 12.68 and 16.29 million cells respectively. A plot of the surface grids can be seen in Fig. 4.15. The Mach and Reynolds numbers were kept the same as the wind tunnel experiments, 0.145 and 1.585×10^6 respectively, to allow for a comparison with the experimental data with the flaps deployed.

Initially, the way each slot was used was by producing a separate grid for each case, similar to the way it was done for the conventional control surfaces. A parent grid was built which has blocks for all the plenum chambers included, with surfaces covering all the slots. When a particular slot combination was chosen, the required surfaces covering the slots were removed and all unnecessary plenum chamber blocks were deleted. This is relatively efficient in terms of human labour. Creating the parent grid can take days or weeks depending on the complexity of the configuration and the size of the grid, while creating a particular grid from the parent grid is a five minute job. However, for a manoeuvring aircraft different groupings of slots are needed to execute a specific manoeuvre. This means the capability to control each of the slots independently, and to be able to turn them off, is needed. To facilitate this, modifications were made to the CFD solver.

An additional input file was used, this has a list of the plenum blocks with the interior blocks that they are connected to and the corresponding block faces. The NPR for each of the slots is part of the unsteady input file as mentioned in the previous section. If a particular slot is turned off then the associated plenum block is excluded from the calculation. The interior block that it was connected to has the face which it was connected to changed into a solid wall sealing the slot off. This is unrealistic as a solid wall instantly appears where the slot exit was and may cause some convergence issues, however, no better solution was found to turn off the jet with a multi-block solver using this boundary condition. It is anticipated that the way these devices will work is that when the plenum chamber reaches the appropriate pressure the slot will open and it will be kept shut during the rest of the flight. This extra functionality works with steady-state simulations too, therefore, only a parent grid is needed and the particular setup can be chosen with the input file.

4.8 Results

The results regarding the yawing moment operation will be discussed first. This will be followed by an investigation of the rolling moment operation, including a comparison against conventional control

surfaces. Lastly, the differences between the three slot and single slot configurations and their effects with regards to the rolling moment operation will be examined.

4.8.1 Yawing Moment Operation

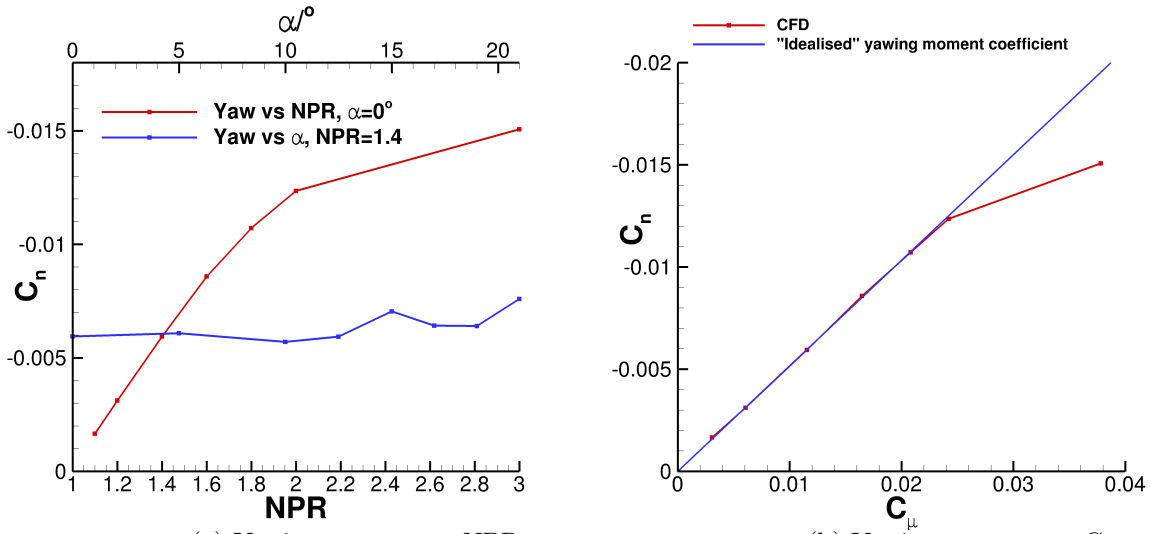

(a) Yawing moment vs NPR.

(b) Yawing moment vs C_μ.

Figure 4.16: Yawing moment against NPR and C_μ for the SACCON with CC determined using CFD.

As mentioned earlier to generate a yawing moment with the CC both upper and lower slots are used in conjuction at the same NPR to reduce the drag for one of the wings. Initially the operation is performed at a range of NPR, at an angle of attack of zero degrees, to get an idea of how it will perform, see Fig. 4.16a. The CFD predicts a linear relationship between the yawing moment and the blowing coefficient at the low NPR. Assuming that the yawing moment is purely a result of the momentum ejected by the coanda jet, and it occurs at a specific point on the wing, then it is possible to determine the yawing moment purely from the blowing coefficient. The point that is used is the geometric centre of the combination of the upper and lower slots, $\mathbf{gc} = [0.96, 0.0265, -0.38]^T$ for the right wing. The velocity of the jet varies slightly along the span of the slot and depends on the local pressure. Therefore, the centre of momentum ejection can change for different NPR and AoA. With these assumptions we obtain the following:

$$C_n = \mathbf{C}_\mu \times (\mathbf{MRP} - \mathbf{gc}) \cdot \hat{\mathbf{j}}$$
$$C_n = -0.51642 C_\mu \tag{4.1}$$

where $\mathbf{C}_\mu$ is the vector of the blowing coefficient, $\mathbf{C}_\mu = C_\mu[0.603, 0, 0.798]^T$, **MRP**, is the moment reference point and $\hat{\mathbf{j}}$ is a unit vector in the y-direction.

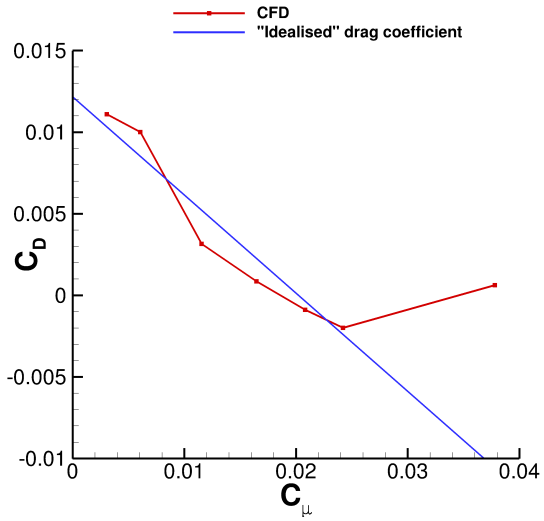

Figure 4.17: Drag coefficient vs. C_μ for the SACCON with CC determined using CFD.

A similar equation can be created for the drag coefficient using the same assumptions:

$$C_D = C_{D0} - \mathbf{C}_\mu \cdot \hat{\mathbf{i}}$$
$$C_D = C_{D0} - 0.603 C_\mu \tag{4.2}$$

where C_{D0} is the drag coefficient of the SACCON with the slots sealed and $\hat{\mathbf{i}}$ is a unit vector in the x-direction.

A comparison of the coefficients determined using the equations with those computed by the CFD is shown in Figs. 4.16b and 4.17. At low blowing coefficients the difference between the two is negligible and only at a blowing coefficient of 0.04 is there a significant difference. The reason for this is that at high NPR the mixing between the jet and freestream flow creates multiple vortices behind the right

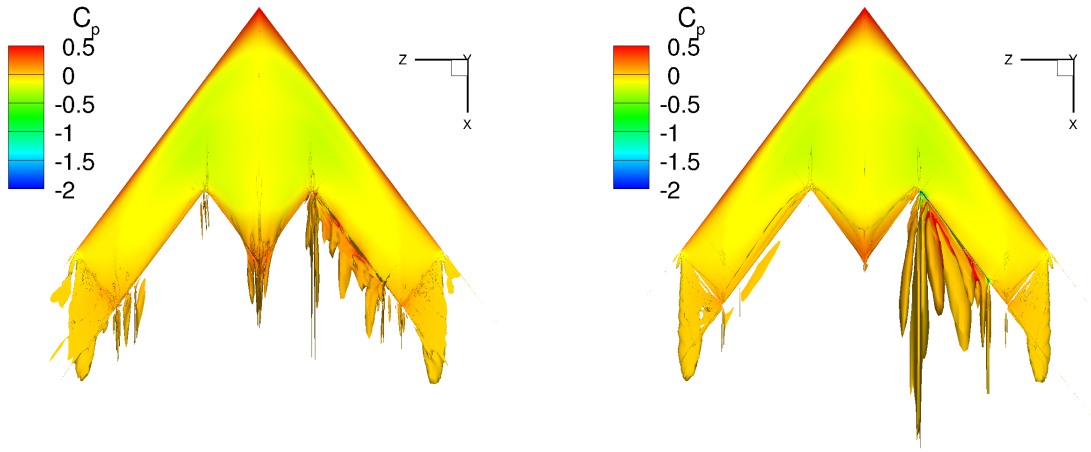

(a) NPR=1.4. (b) NPR=3.

Figure 4.18: Iso-surfaces of the λ_2 criterion coloured with C_p for the SACCON with CC using the upper and lower slots on the right wing at a NPR of 1.4 and 3.

wing. This creates low pressure regions behind the root and tip of the wing that counteract the yawing moment, see Fig. 4.18b. Also, it can seen that the linear relationship between the yawing moment and blowing coefficient at low NPR occurs because the effect of the jet on the flow over the wings is minimal, see Fig. 4.18a.

The conventional method for generating a yawing moment is by deflecting the vertical flap on the tail. However, for these type of aircraft, tailless configurations are preferred due to stealth considerations. For these, yawing moment is generated using split elevons which increases the drag for one of the wings. Experimental data for the SACCON with the split elevon deployed was not available at the time of writing. Also, representing the split elevon using a multi-block grid is difficult. Therefore, this operation will not be compared against a conventional control method and its performance will be evaluated differently.

The key interest in this operation is how large a sideslip angle is the CC able to trim. To determine this the maximum yawing moments generated by the SACCON, with no deflection of the control surfaces, for the range of conditions investigated is examined. The experimental results are used for the purpose of the discussion. Alpha sweeps, for selected sideslip angles, were performed from angles of approximately

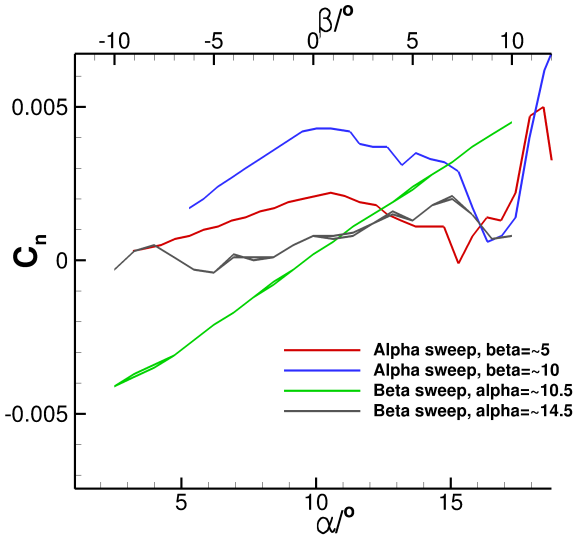

Figure 4.19: Yawing moment vs. α and Yawing moment vs. β for the SACCON at various conditions.

zero up to thirty degrees. Similarly, beta sweeps were performed at a particular AoA for angles between negative ten and ten degrees. See Fig. 4.19 for two alpha and beta sweeps. The two alpha sweeps were performed at sideslip angles of approximately five and ten degrees. While the flow is attached, between approximately zero and seventeen degrees, the maximum yawing moment occurs at an AoA of about ten and a half degrees for both sideslip angles. There are large spikes at higher angles due to asymmetric vortex bursting, which is characteristic of such planforms. For the beta sweeps, we see that at an AoA of about ten and a half degrees the yawing moment has a linear dependency on the sideslip angle. The maximum yawing moment is generated at this AoA is 0.0045. At the higher AoA, fourteen and a half degrees, for the small sideslip angles there is a sort of spiky linear dependence due to the prescence of the vortices on the upper surface. However, at sideslip angles above a magnitude of approximately six degrees this breaks down. The maximum yawing moment is only about 0.002 in this case.

The effect of the AoA on the performance of the yawing moment operation is relatively minimal, Fig. 4.16b. Therefore the CC should easily be able to maintain a trimmed state for sideslip angles larger than 10° at low Mach numbers.

4.8.2 Rolling Moment Operation

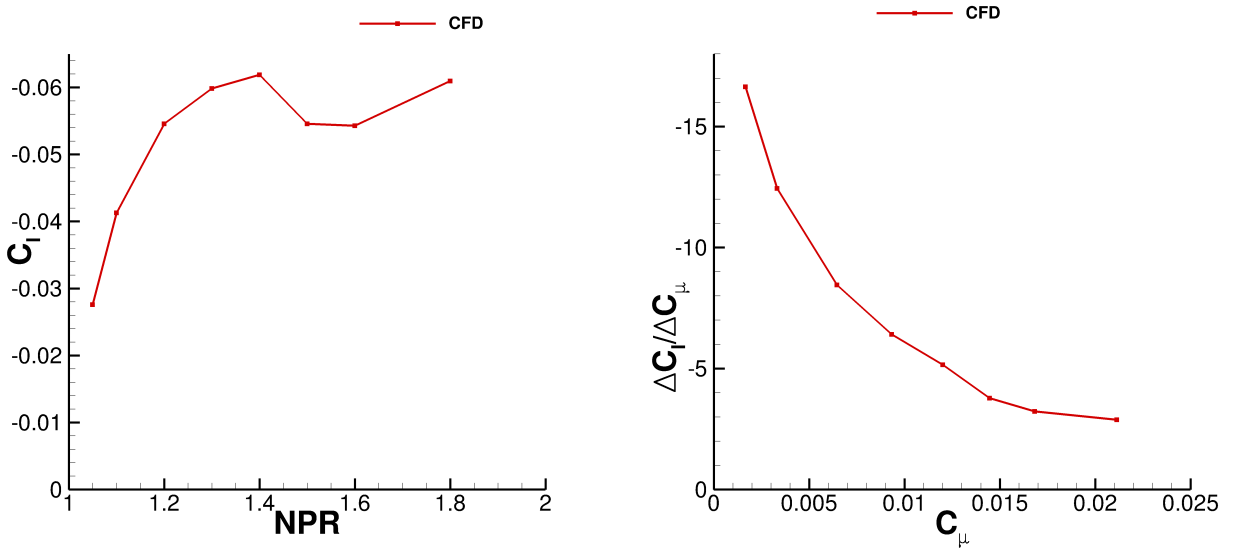

(a) Rolling moment vs. NPR.

(b) Rolling moment efficiency vs. C_μ.

Figure 4.20: Rolling moment and efficiency for the SACCON with CC at 0°.

The rolling moment is generated by using the upper slot on the right wing and the lower slot on the left wing. Initially the operation is done for a range of NPR, at an angle of attack of zero degrees, to get an idea of how it will perform, see Fig. 4.20a. Before understanding why the rolling moment curve behaves as it does, it is necessary to understand how the flowfield is affected by the jet and how the rolling moment is being generated. Unlike the yawing moment operation, the interaction of the jet with the freestream flow is quite complex. The case with a NPR of 1.2 will be used as an illustrative example to facilitate the explanation. The flowfield will only be described for the right wing, for the left wing the behaviour is inverted. An overall view of the wing can be seen in Fig. 4.21 with boxes indicating the regions that are focused on in the subsequent figures. The jet exits as a vortex sheet with the sides curling over due to the presence of the side walls, see Fig. 4.22. These parts of the jet interact with the flow over the upper surface creating a vortex at the root of the wing which travels in the direction of the freestream flow, see Fig. 4.23b. The extent of this vortex can be seen in a later plot, see Fig. 4.26a.

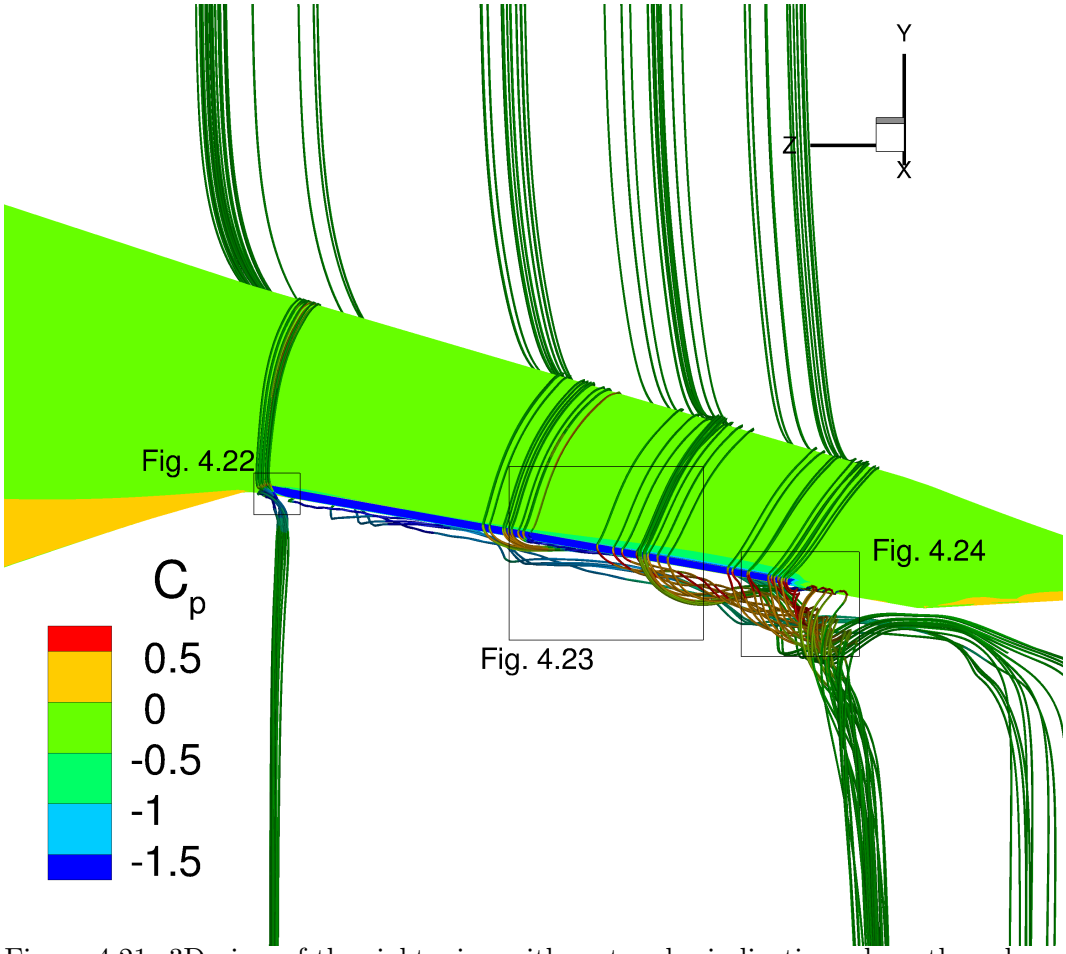

Figure 4.21: 3D view of the right wing with rectangles indicating where the subsequent close ups are.

There are also small recirculation zones beneath the curled up portion of the jet. These mix with the flow under the lower surface creating a small vortex adjacent to the lower sealed slot, see Fig. 4.23a. This vortex travels in the spanwise direction along the lower surface, increasing in size as it moves towards the wing tip, see Figs. 4.24a and 4.25a. Eventually it merges with the wing tip vortex, this can be seen more clearly in Fig. 4.26. The result of this is a decrease in the size of the wing tip vortex as they are counter-rotating, for the left wing the wing tip vortex increases in the size. As the NPR is increased this vortex increases in size, see Figs. 4.26c and 4.26d.

Another vortex originates near the tip of wing where the spanwise extent of the slot terminates. This is created in a similar way to the one originating from the root. The side wall of the CC creates recirculation

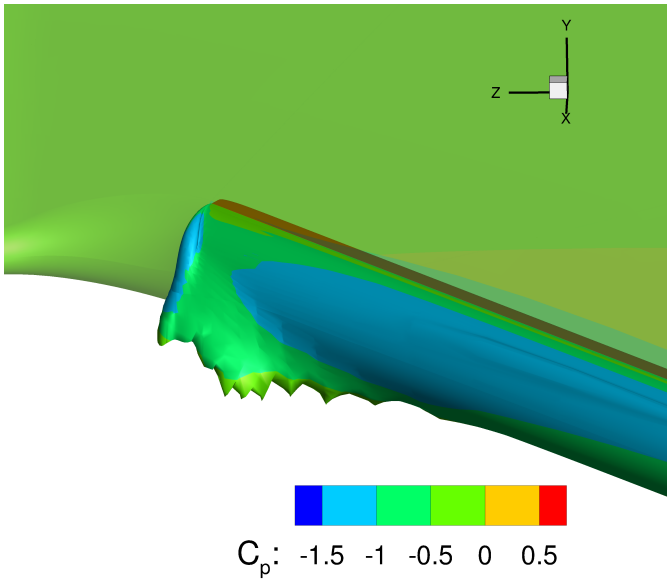

Figure 4.22: 3D view at the root of the wing of the jet exiting the slot.

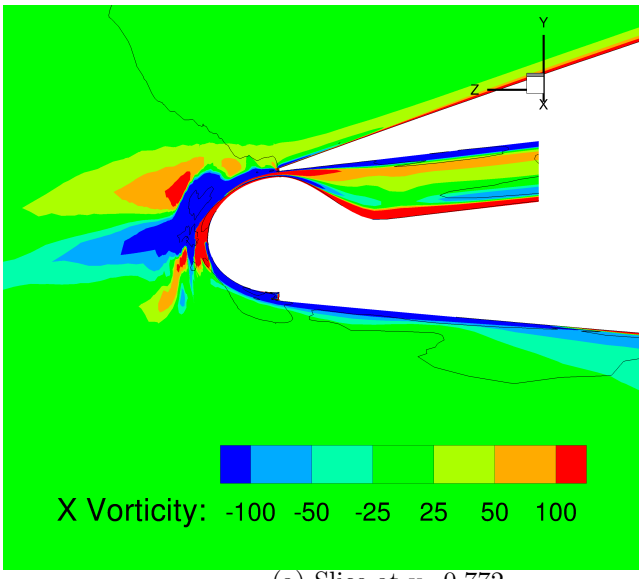

(a) Slice at x=0.772.

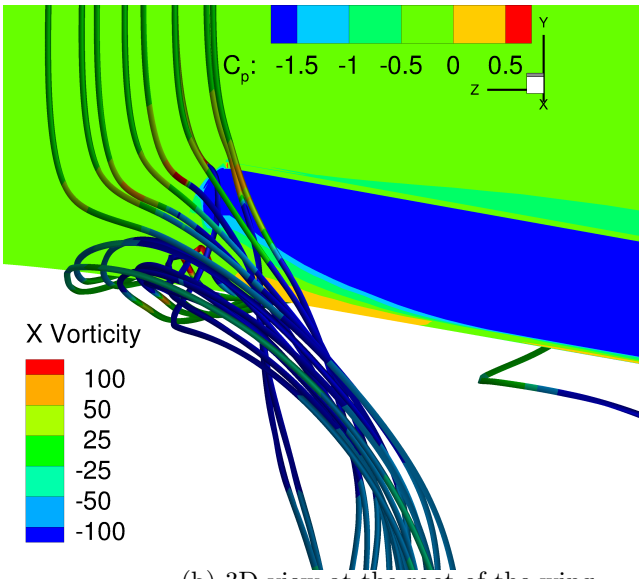

(b) 3D view at the root of the wing.

Figure 4.23: The slice is coloured using X-vorticity contours and the regions enclosed by black lines are regions identified as vortices by the λ_2 criterion. The surfaces in the 3D view are coloured using C_P contours and the streamtraces are coloured with X vorticity.

zones and slows down parts of the jet which interact with the freestream flow creating the vortex. This can be seen in Figs. 4.25a and 4.26a. As the jet exits normal to the trailing edge it creates a strong

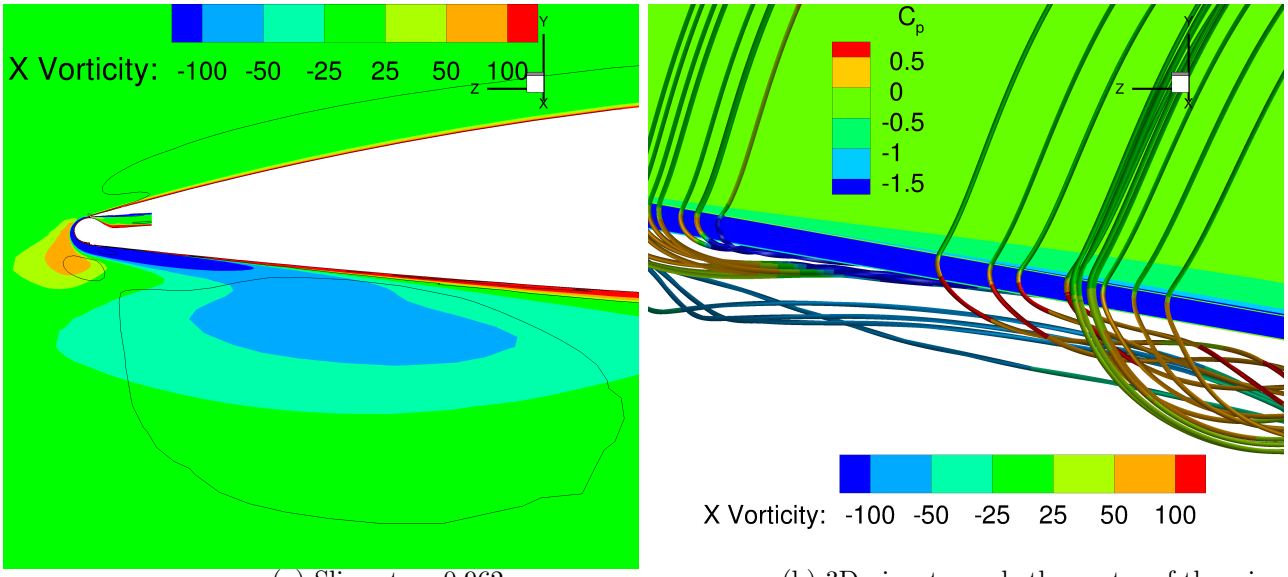

(a) Slice at x=0.962.

(b) 3D view towards the centre of the wing.

Figure 4.24: The slice is coloured using X-vorticity contours and the regions enclosed by black lines are regions identified as vortices by the λ_2 criterion. The surfaces in the 3D view are coloured using C_P contours and the streamtraces are coloured with X vorticity.

shear layer with the oncoming flow beneath the wing forming another vortex towards the centre of the CC device, see Figs. 4.26a. This vortex is only seen on the left wing and as the NPR is increased its location moves towards the wing tip, see Figs. 4.26c and 4.26d.

For an understanding of the way the moment is generated see Fig. 4.27. These plots show the moment generated as a proportion of the total roll moment, it is calculated by determining the moment at each point on the surface and dividing by the total moment. The main portion of the rolling moment is generated on the upper surface in the area around the slot while the upper slot is in use and vice versa while the lower slot is being used, Figs. 4.27a and 4.27b. There is a large suction peak at the slot which lowers the pressure in the area around it on the upper surface. The moment contribution increases towards the wing tip, partly for the obvious reason that it is further from the moment reference point but also because the pressure is lower there, increasing the speed of the jet and making it more effective. The vortex emanating from the root of wing on the opposite side of the jets counteracts the moment,

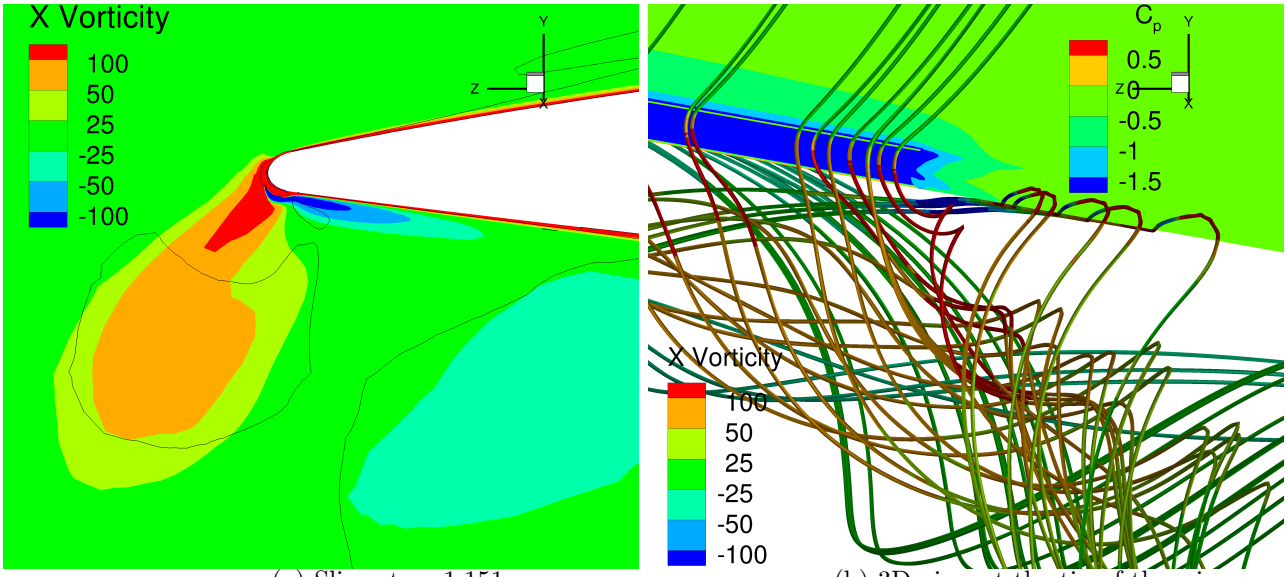

(a) Slice at x=1.151.

(b) 3D view at the tip of the wing.

Figure 4.25: The slice is coloured using X-vorticity contours and the regions enclosed by black lines are regions identified as vortices by the λ_2 criterion. The surfaces in the 3D view are coloured using C_P contours and the streamtraces are coloured with X vorticity.

however this also blocks the flow creating a higher pressure region that also contributes to the moment, see the trailing edge of the left wing in Fig. 4.27a. Visually it seems that the vortex is having a slightly stronger effect than the high pressure region. However, it is very difficult to show this concretely as it is unclear how to define the boundaries of the two regions. As the NPR is increased and the size of the vortex increases it becomes clear that the vortex has a larger effect on the moment compared to the high pressure region, see Figs. 4.27a and 4.27c. However, the vortex's increase in size slows down significantly after a NPR of 1.6. As the NPR is increased there is very little difference to the moment contribution over the upper surface, see Figs. 4.27a and 4.27c. The major difference occurs as a result of the increase in the size of the vortex emanating from the root of the wing. This helps to explain the behaviour that we see in Fig. 4.20a. Initially as the NPR is increased there is almost a linear increase in the roll moment. This is because the upper surface contribution is increasing proportionally with the NPR. However, on the lower surface the balance between the vortex and the high pressure region is negligible to start off

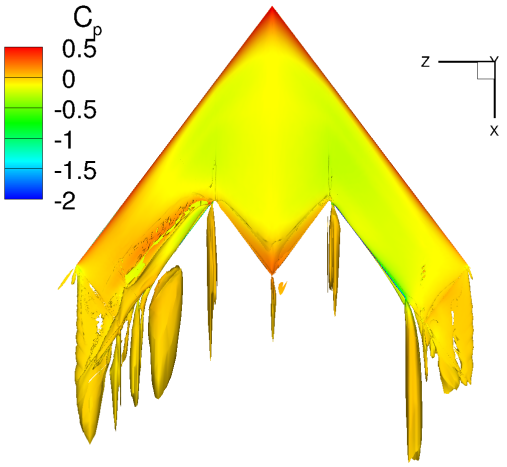

(a) NPR=1.2 upper surface.

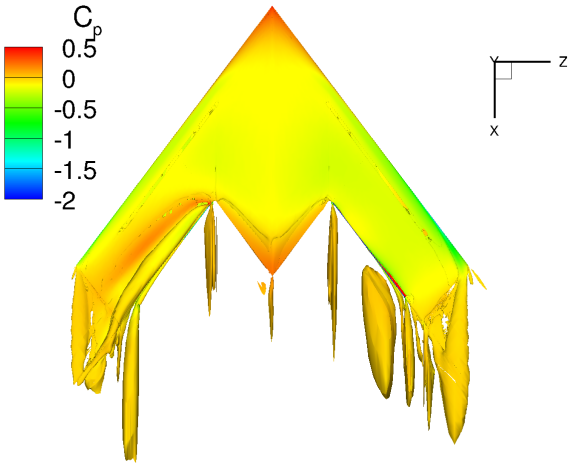

(b) NPR=1.2 lower surface.

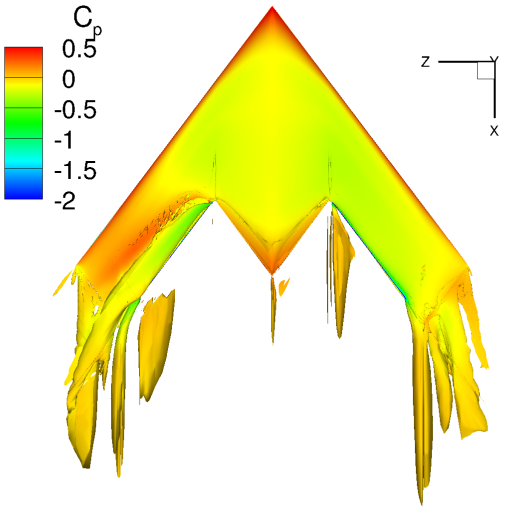

(c) NPR=1.5 upper surface.

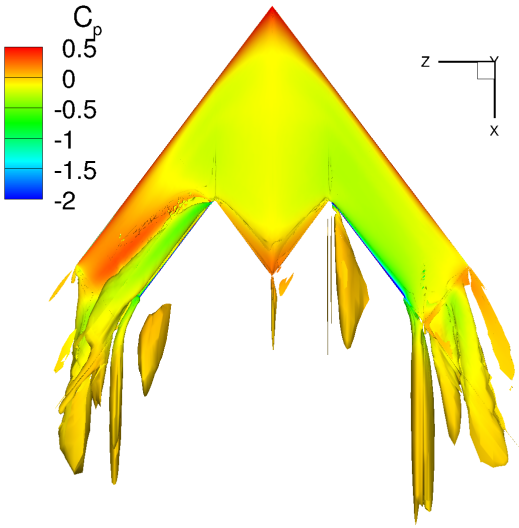

(d) NPR=1.8 upper surface.

Figure 4.26: Iso-surfaces of the λ_2 criterion coloured with C_p for the SACCON with CC using the upper slot on the right wing and lower slot on the left wing at a range of NPRs.

with. Then, as the size of the vortex increases it begins to hinder the process, this causes a dip in the roll moment curve. Eventually the vortex stops growing with the increase in the NPR and then we see a further increase in the roll moment.

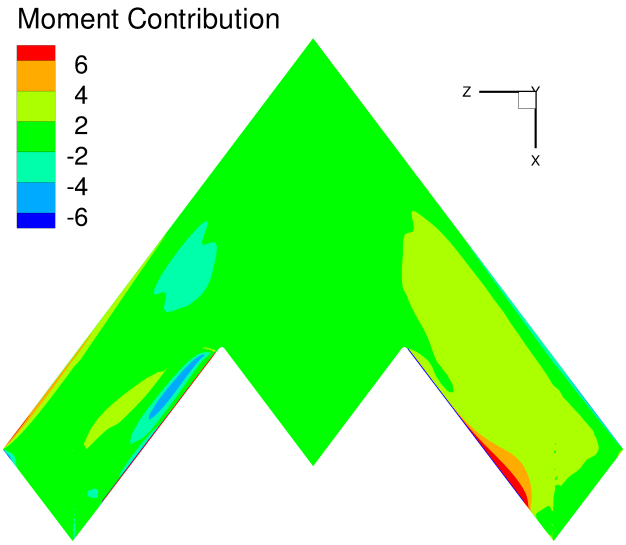

(a) NPR=1.2 upper surface.

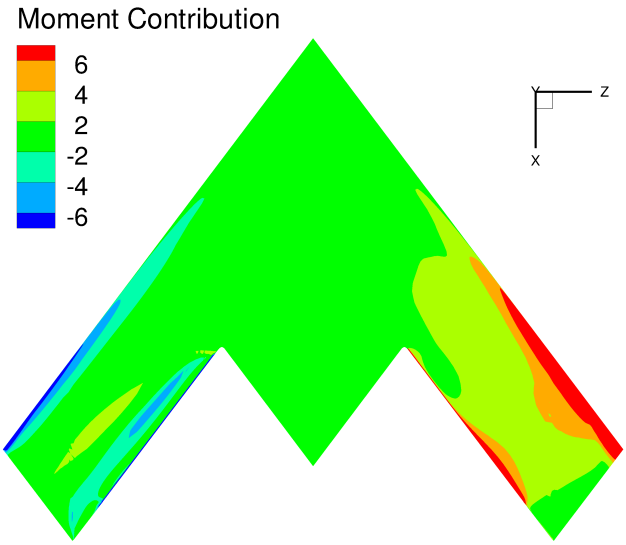

(b) NPR=1.2 lower surface.

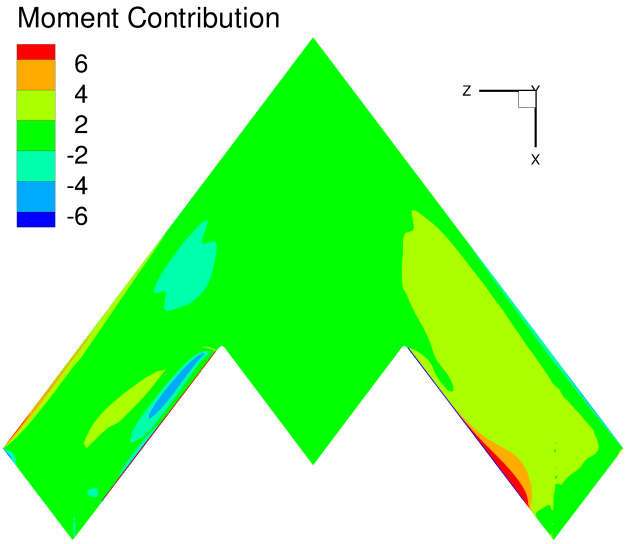

(c) NPR=1.6 upper surface.

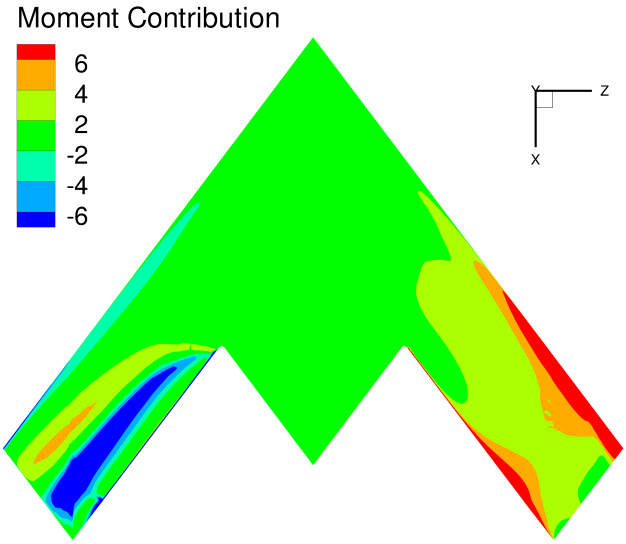

(d) NPR=1.6 lower surface.

Figure 4.27: Plot showing the contribution to the roll moment for a NPR of 1.2 and 1.6 for the case with the single slot CC.

4.8.3 Comparison against Conventional Control Surfaces

The next step is to investigate the performance of the CC device across the AoA range and compare them against conventional control surfaces. The comparison will be against the configuration with

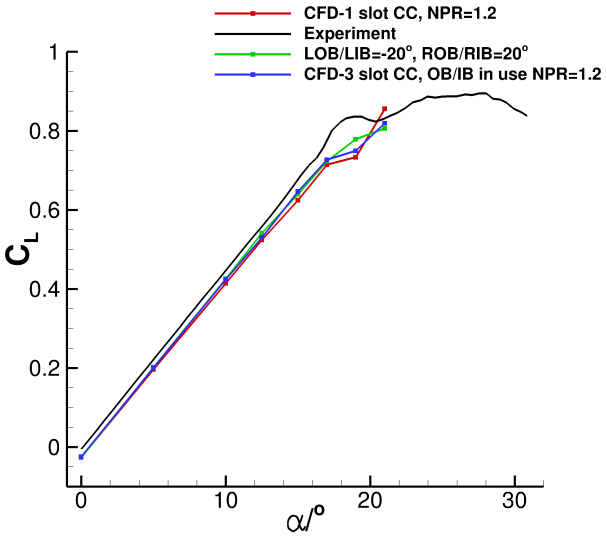

(a) Lift coefficient.

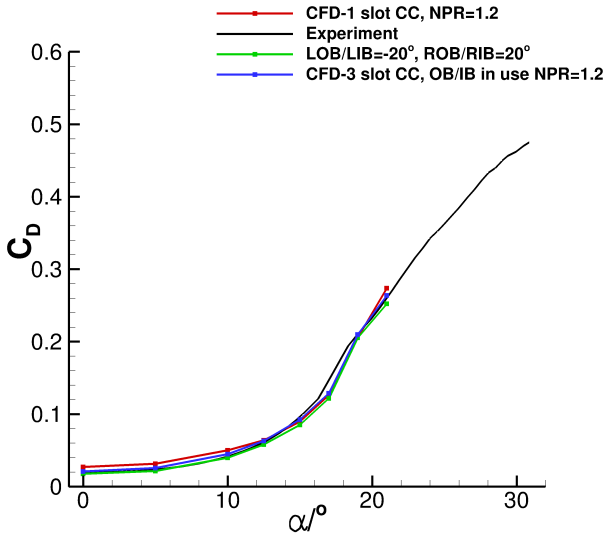

(b) Drag coefficient.

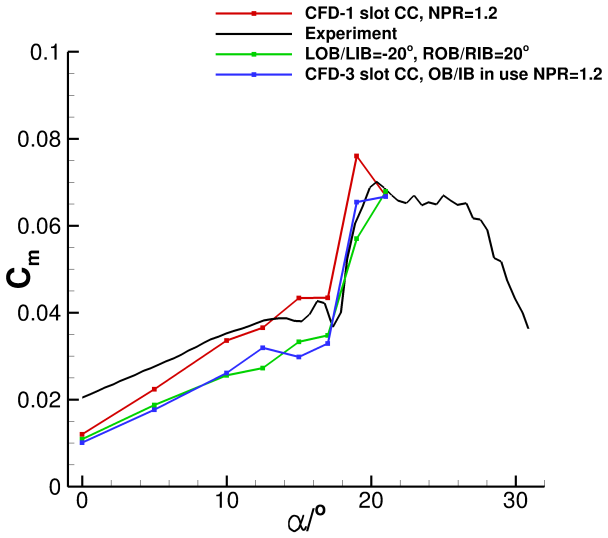

(c) Pitching moment coefficient.

Figure 4.28: Comparison of the loads from the experiments with LOB/LIB at −20° and ROB/RIB at 20°, the integrated loads from the CFD results with the same flap settings and the integrated loads from the CFD result of the SACCON with CC at a NPR of 1.20.

both the right inboard and outboard flaps (RIB/ROB) at 20° and the left inboard and outboard flaps (LIB/LOB) at −20° (20/0/-20 are the only configurations which match an experimental setup). The NPR was then chosen to approximately match the roll moment generated by the flaps at an AoA of 0°

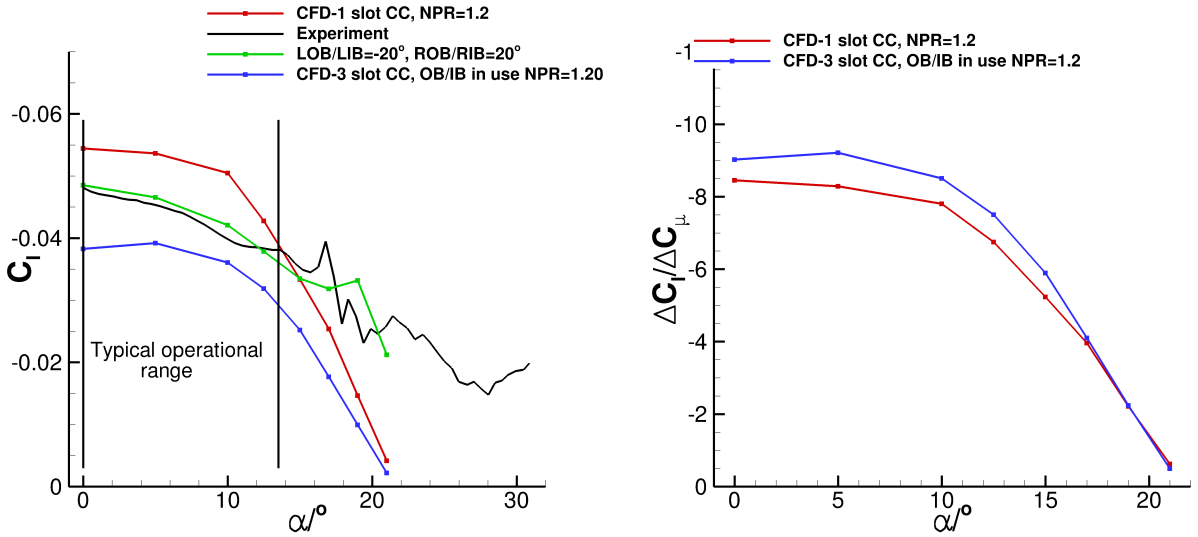

(a) Rolling moment coefficient.

(b) Roll moment coefficient/Blowing coefficient.

Figure 4.29: Comparison of the loads from the experiments with LOB/LIB at $-20°$ and ROB/RIB at $20°$, the integrated loads from the CFD results with the same flap settings and the integrated loads from the CFD result of the SACCON with CC at a NPR of 1.20.

and then kept constant over the AoA range tested. A NPR of 1.2 was used which corresponds to a C_μ of 0.00645 at an AoA of $0°$. The purpose is to investigate the performance of the CC device over the AoA range, not to match the performance of the flap precisely.

For the integrated loads see Figs. 4.28 and 4.29. As can be seen from the lift, drag and pitching moment coefficients, Figs. 4.28a, 4.28b and 4.28c, the CC device has a relatively similar effect on these coefficients as the flaps do. The pitching moment coefficient's gradient is slightly higher than the flaps causing a larger pitch up moment as the angle of attack is increased. This is due to the fact that the high speed jet causes a large pressure drop around the trailing edge which affects the flow in its vicinity. Whereas for the flaps, the geometric change creates a smoother pressure distribution over the wing. The gradient of the lift coefficient curve as well as C_L values have been reduced slightly due to the reduced wing area, the original wing area is used for scaling the coefficients. The CC device produces slightly more drag at the lower angles of attack however the difference is reduced as the angle of attack is increased.

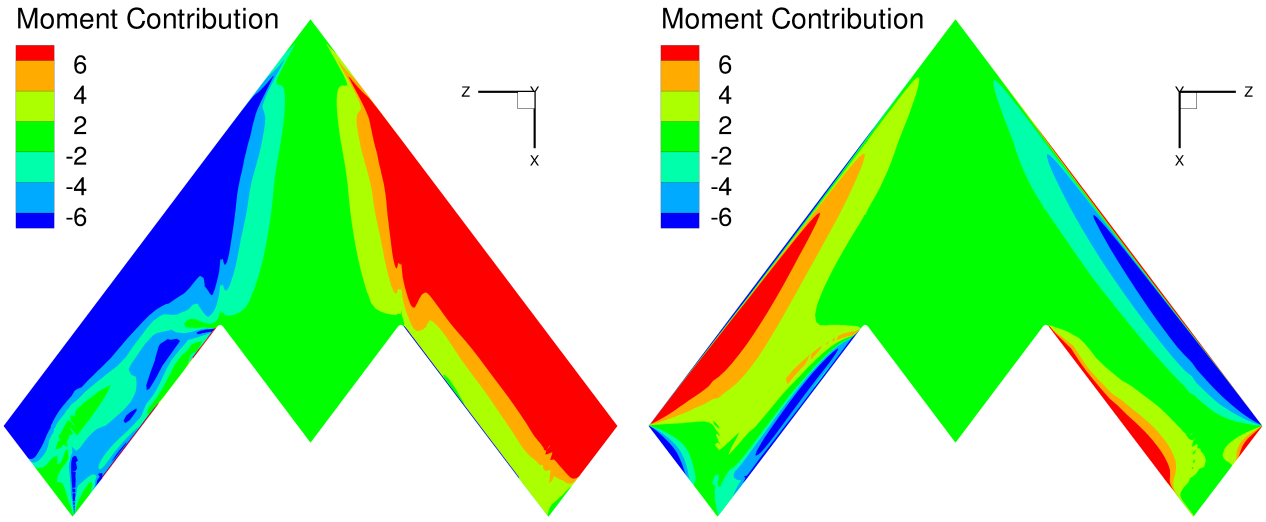

(a) AoA=15° upper surface.

(b) AoA=15° lower surface.

Figure 4.30: Plot showing the contribution to the roll moment for a NPR of 1.2 for the case with the single slot CC.

The rolling moment slope for the CC device is smaller than the conventional flaps for the lower angles of attack, maintaining a stronger roll moment initially. However it starts to increase after 10° making the CC device's effectiveness significantly impaired at higher angles whereas the conventional flaps have an almost linear loss of roll moment with spikes in the non-linear region.

The main reason for this difference in the loss of control, as the AoA is increased, is because the CC relies primarily on the upper surface of the wing to generate the roll moment. As the vortices over the upper wing begin to increase in size, they create large regions of separated flow around the trailing edge, Fig. 4.31. The coanda jet has almost no effect on these regions. Also as a proportion of the total moment the flow around the leading edge (which is affected mainly by the angle of attack and not the jet) contributes much more relative to the effects of the jet, see Figs. 4.30a and 4.30b. The location of the vortices is affected slightly by the pressure change around the trailing edge, Fig. 4.31a, which helps to slow the loss of roll moment. However, this does not compensate enough for the reduction in moment contribution around the slot. By an AoA of 19° the flow over the upper surface is completely

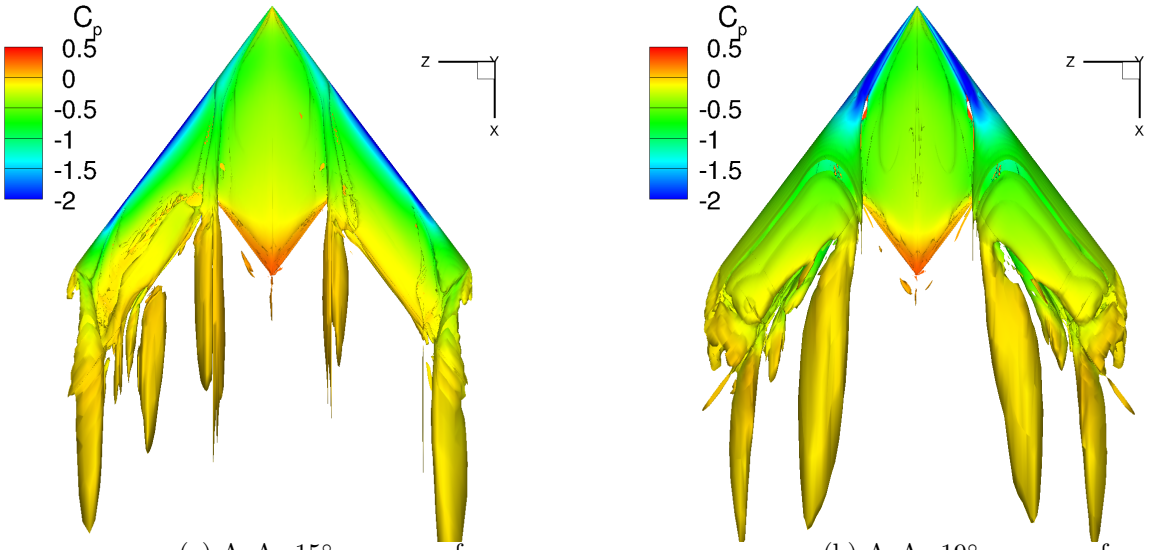

(a) AoA=15° upper surface.

(b) AoA=19° upper surface.

Figure 4.31: Iso-surfaces of the λ_2 criterion coloured with C_p for the SACCON with CC using the upper slot on the right wing and the lower slot on the left wing at a NPR of 1.2.

dominated by the separated flow and the coanda jet has no effect, Fig. 4.31b. In contrast to this, for the conventional control surfaces both upper and lower surfaces contribute relatively equally to begin with, Figs. 4.32a and 4.32b. And as the AoA is increased the contribution from the lower surface is left relatively unaffected, Figs. 4.32c and 4.32d.

4.8.4 3-slot Configuration

Using multiple slots along the span of the wing makes it possible to control the blowing coefficient without having to vary the NPR. A higher blowing coefficient can be used by using more slots and vice versa. This allows the CC device to be designed for a particular NPR, making it possible to optimise for those conditions, potentially increasing the effectiveness. This configuration was not used to investigate the yawing moment operation as the effects on the flow over the wings are minimal. Also, the grid size increases for the 3-slot case making it more computationally expensive. Therefore, the investigation was restricted to the rolling moment operation as there is potential for interference between the slots and different flow behaviour. The inboard and outboard slots will be used to determine if there are any

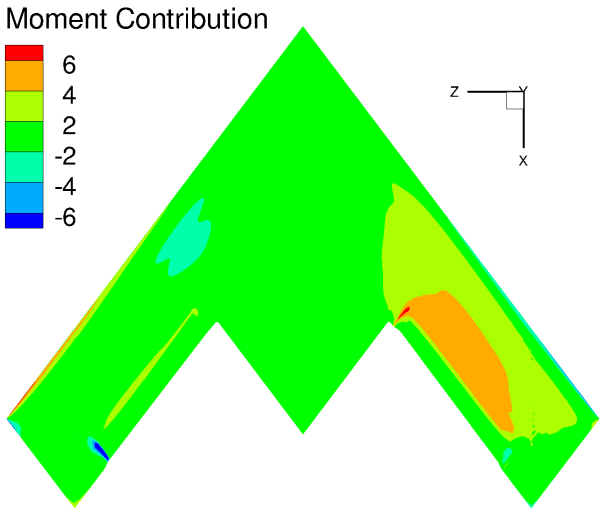

(a) AoA=0° upper surface.

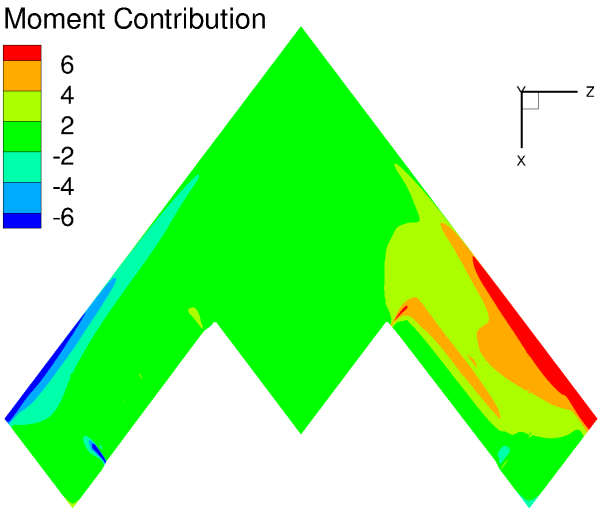

(b) AoA=0° lower surface.

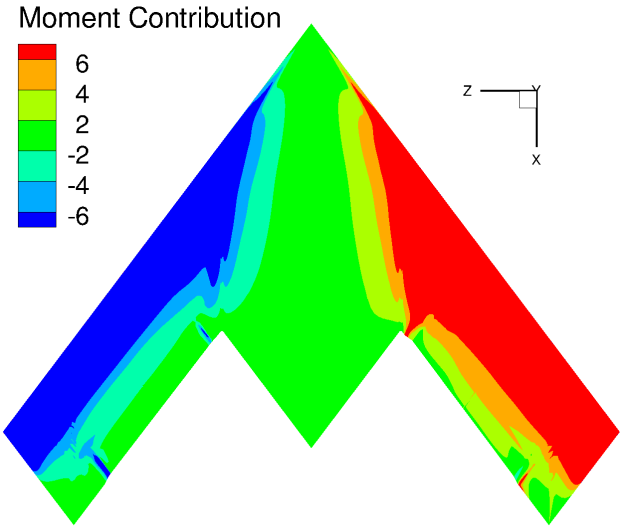

(c) AoA=15° upper surface.

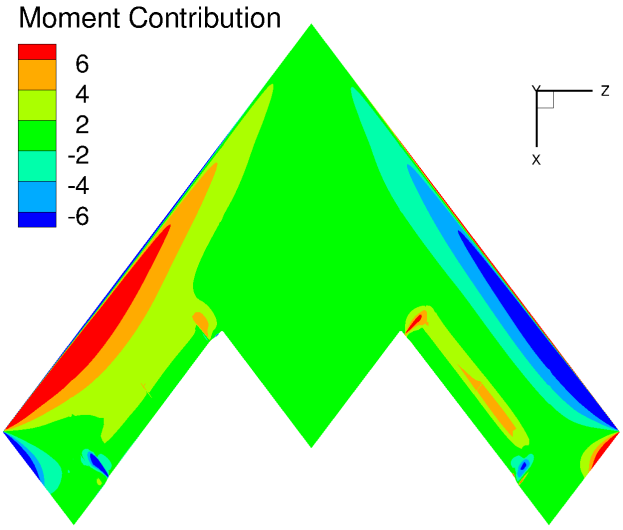

(d) AoA=15° lower surface.

Figure 4.32: Plot showing the contribution to the roll moment for 0° and 15° for the case with conventional control surfaces.

changes in the efficiency and if there is any inteference between the slots.

The integrated loads can be seen in Figs. 4.28 and 4.29. The overall flow behaviour is similar to that of the single slot case broken up into smaller sections. There are two key differences between the single slot and three slot configurations. Firstly, for the three slot configuration the effects of the inboard

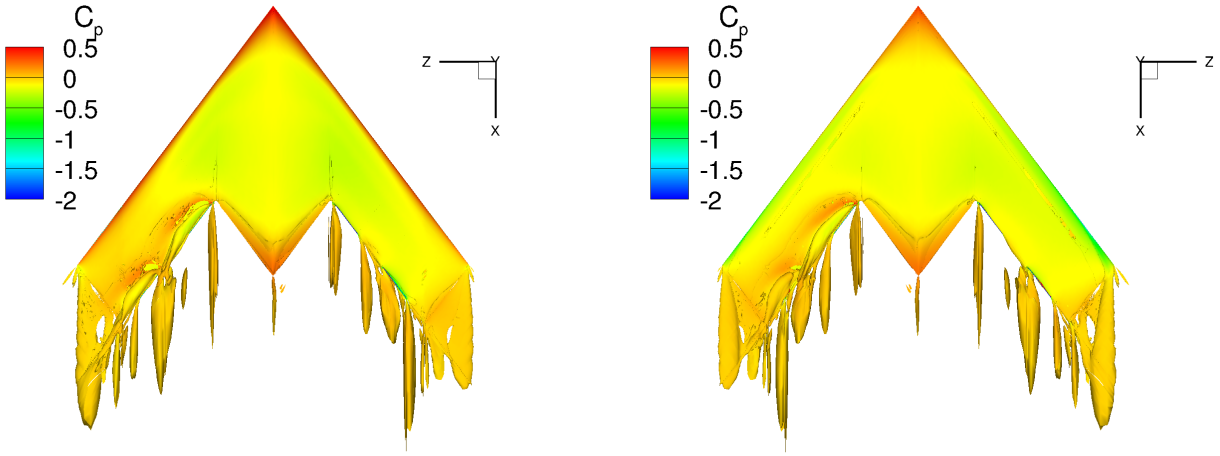

(a) AoA=0° upper surface.

(b) AoA=0° lower surface.

Figure 4.33: Iso-surfaces of the λ_2 criterion coloured with C_p for the SACCON with CC using the upper IB/OB slots on the right wing and the lower IB/OB slots on the left wing at a NPR of 1.2.

and outboard jets spill over into the middle section of the wing lowering the pressure slightly in that region too, see Fig. 4.34. Secondly, the vortices that travel along the wing span on the surface opposite the active jet. In the single slot case we had a single vortex emanating from the root of the wing which increased in size eventually combining with the wing tip vortex. In the three slot case once the vortex has reached the section without an active jet it mixes with the freestream flow and dissipates, see Fig. 4.33. A second vortex, travelling along the span similar to the previous one, is also present at the beginning of the outboard section. Because of this, relative to the single slot case, it seems the contribution from the high pressure region and the region below the vortex has a smaller effect, Figs. 4.30 and 4.34. The result of these differences is that the three slot configuration is between 6.5% and 12% more efficient during the attached regime, see Fig. 4.29b. However, the performance still drops off in an almost identical fashion to the single slot case. Also, there is very little difference between the single and three slot case when considering the other coefficients, lift,drag and pitching moment. The drag and pitching moment are slightly lower, but this is because the blowing coefficient for the three slot case is only two thirds of the

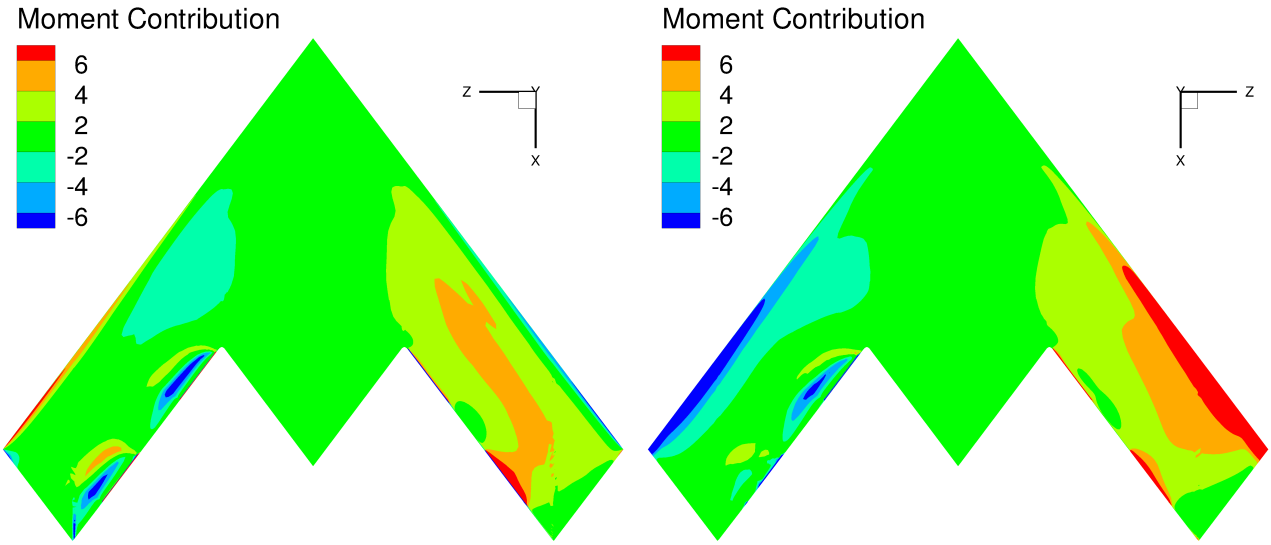

(a) AoA=0° upper surface.

(b) AoA=0° lower surface.

Figure 4.34: Plot showing the contribution to the roll moment for a NPR of 1.2 for the case with three slot CC.

single slot case.

4.9 Summary and Conclusions

Circulation control has been applied to a generic UCAV planform, the SACCON. This includes two configurations, one with a single slot and one with three slots along each each wing, the overall spanwise extent is equal to that of the flaps used in the wind tunnel setup. Two operations were investigated, one used to generate roll moment and the other yaw moment. The performance of the CC with respect to the yawing is quite robust. The coanda jet has almost no effect on the flow over the wing and generates the yawing moment as a result of the momentum ejected from the slot. The relationship between the yawing moment and the NPR is almost linear and even when the flow over the wing is completely separated it is still able to perform. Further investigation into the location of the slot to improve the performance of this operation could be conducted. Placing the slot closer to the wing tip would increase the moment arm, however, the wing tip vortex may cause interference limiting its effectiveness. For the roll moment

the results have shown that at low angles of attack the fluidic devices can match the conventional control surfaces. However, it relies mainly on the upper surface of the wing to generate the control moment. At high angles of attack the flow separates over the wings and by 21° the CC devices are almost completely ineffective at generating a rolling moment. In contrast to this, the flaps maintain their effectiveness up to slightly higher angles of attack. The key difference between the single slot and three slot configuration was in the efficiency of the CC. The three slot configuration was approximately 10% more efficient between angles of attack of 0° and 15°. This is attributed to the spill over effect around the slot and the reduced size of the vortex on the opposite surface. Further investigation into the number of slots should be done to see if the efficiency can be increased further. A parametric study of the distance between each of the slots, the number of slots and the width of each slot could be performed to determine this.

Chapter 5

Reduced Order Modelling: Tabular Method

One method which can be used to predict loads and moments during aircraft manoeuvres is the tabular method. This uses large lookup tables which store the loads for the range of flight parameters. One advantage of this method is that it can represent any non-linearities in the loads accurately. However, for a full aircraft employing conventional control surfaces, these tables typically depend on the Mach number (M), angle of attack (α), sidelip angle (β) and the control parameters (δ_i) for each of the control surfaces. The usual control surface combination is elevator, aileron and rudder. For tailless aircraft the elevator and rudder are replaced by split elevons and stability about the pitch and roll axis are incorporated into the wing design. Using one integrated table, $[M, \alpha, \beta, \delta_e, \delta_a, \delta_r]$, requires a very large number of data entries to populate it. Assuming n entries are needed for each dimension, then a total of n^6 entries are required. To reduce the number of entries needed, certain parameters can be decoupled within the tables. This assumes that the effect of each parameter is linearly independent, e.g. a change in the angle of the rudder will not affect the load contribution that an aileron is producing. In the case of a full aircraft, the sideslip angle and the angles for the control surfaces can be decoupled. The result of this is four tables with three dimensions: $[M, \alpha, \beta]$, $[M, \alpha, \delta_e]$, $[M, \alpha, \delta_a]$ and $[M, \alpha, \delta_r]$. Doing this reduces the total number of entries from n^6 to $4n^3$, assuming n entries are needed for each dimension. The loads are then determined using the following equation:

$$C = C_0(M, \alpha, \beta) + C_1(M, \alpha, \delta_e) + C_2(M, \alpha, \delta_a) + C_3(M, \alpha, \delta_r) \tag{5.1}$$

where C is the load or moment coefficient that is being predicted. $C_0(M, \alpha, \beta)$ is the load or moment coefficient for the aicraft as discussed above. C_1, C_2 and C_3 represent the increments in the loads relative to $C_0(M, \alpha, \beta = 0)$, i.e. the load increments caused by the flap deflection angles. This method has been used to construct a flight dynamics model for the SACCON configuration in [56]. Ailerons were used for roll control and the fluidic thrust vectoring for control about the pitch and yaw axes. This allowed for two three dimensional tables to be generated, the fluidic thrust vectoring was included directly into the equations of motion by assuming a single point exhaust.

Within the tabular model a selected number of discrete entries are determined. These entries can be calculated using a variety of methods such as semi-empirical methods, panel methods and Euler CFD, ordered by increasing computational cost per entry. In the current work the selected points were calculated using RANS CFD simulations. This increases the computational cost significantly, however, the RANS model is able to predict the loads at the edges of the flight envelope where flow separation begins to occur. Also, as predicting the performance of the CC relies heavily on predicting the rear separation point of the jet, none of the other methods are currently feasible for CC. The remainder of the domain is then determined using Kriging interpolation. The interpolation is performed using a MATLAB based code called DACE (Design and Analysis of Computer Experiments), built by the the Technical University of Denmark [59].

The complexity of the model can be increased by including quasi-steady effects. This is done by building additional tables with stability derivatives. With the inclusion of these effects equation 5.1 then becomes:

$$
\begin{aligned}
C = C_0(M,\alpha,\beta) + C_1(M,\alpha,\delta_e) + C_2(M,\alpha,\delta_a) + C_3(M,\alpha,\delta_r) \\
+C_p(M,\alpha,p)\frac{pc}{U_\infty} + C_q(M,\alpha,q)\frac{qc}{U_\infty} + C_r(M,\alpha,r)\frac{rc}{U_\infty} \\
+C_{\dot{\delta}_e}(M,\alpha,\dot{\delta}_e)\frac{\dot{\delta}_e c}{U_\infty} + C_{\dot{\delta}_a}(M,\alpha,\dot{\delta}_a)\frac{\dot{\delta}_a c}{U_\infty} + C_{\dot{\delta}_r}(M,\alpha,\dot{\delta}_r)\frac{\dot{\delta}_r c}{U_\infty}
\end{aligned} \tag{5.2}
$$

where $C_{p,q,r}$ are the stability derivatives with respect to rolling, pitching and yawing, respectively and $C_{\dot{\delta}_e,\dot{\delta}_a,\dot{\delta}_r}$ are the control derivatives with respect to the elevator, aileron and rudder motion, respectively. Similarly to static coefficients, these represent the increments with respect to $C_0(M,\alpha,\beta = 0)$, i.e. $C_q(M,\alpha,q)\frac{qc}{U_\infty}$ corresponds to the increment caused by the pitch rate. These derivatives can be estimated using the harmonic balance technique, which uses forced sinusoidal motions [60]. However, due to the way unsteady simulations are performed with PMB, it is possible to run a simulation with a constant pitch rate but no angle of attack change. The result of this is an indicial response with respect to a change in pitch rate, with the result as $T \to \infty$ being the pitch damping derivative. As seen in section 4.5, the final result does not depend on the size of the timestep. This allows a solution to be obtained significantly faster and cheaper when compared with the forced periodic motion where multiple cycles can be required to obtain a converged solution. An example of an indicial response can be seen in Fig. 5.1.

5.1 Circulation Control Aerofoil

For a two dimensional aerofoil with circulation control the static aerodynamic coefficients depend on three parameters; the angle of attack, Mach number and the NPR. With the inclusion of unsteady effects an additional parameter is needed, the pitch rate. The modified aerofoil from the root of the SACCON's wing were be used as a test case to evaluate the performance of the tabular methods for such applications. The effects of decoupling the angle of attack from the NPR within the tables will be investigated. Also, the way the discrete entries are chosen with respect to the NPR parameter will be explored. Past work has been performed demonstrating the effects of the resolution of the tables on the

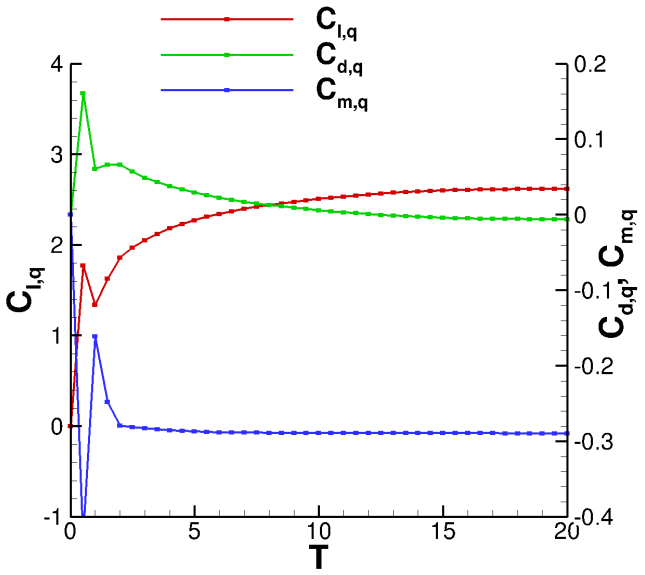

Figure 5.1: Indicial response for an anlge of attack of 5° for the modified aerofoil from the root of the SACCON's wing with the jet turned off.

predictions of the loads and moments [61]. However, due to the attachment behaviour of the coanda jet the loads are discontinuous at very low NPR making it necessary to examine the way the points are chosen for the NPR. The performance of the tabular methods will be assessed against time-accurate CFD simulations. As the tables were constructed using CFD results, the best that can be achieved is matching the unsteady simulation. Therefore, any discrepancies between the two solutions is attributed to the inadequacy of the tabular methods.

5.1.1 Sample Placement for the Nozzle Pressure Ratio Parameter

In previous work the selection of points was performed using regular intervals [61]. In the case of a flap, the increments in the aerodynamic coefficients are usually smooth functions of the deflection angle, therefore, it is reasonable to use regular intervals. However, for the CC the increments in the loads while the jet is separated are practically negligible, for the purpose of a manoeuvring aircraft. Then, once the jet becomes attached the increments instantly become significant creating a discontinuity. The bifurcating behaviour observed in chapter 4 is interesting to model from a theoretical point of view but

for industrial application it is not required. For the CC to be used as a replacement for conventional control surfaces the jet must remain attached. Therefore, being able to predict whether jet separation will occur is important, but trying to incorporate it into the flight mechanics model would increase the complexity unnecessarily. Two approaches will be used for the point selection. Firstly, regular intervals with increasing number of points accross the domain. Secondly, neglecting the region where the jet is separated and using regular intervals across the rest.

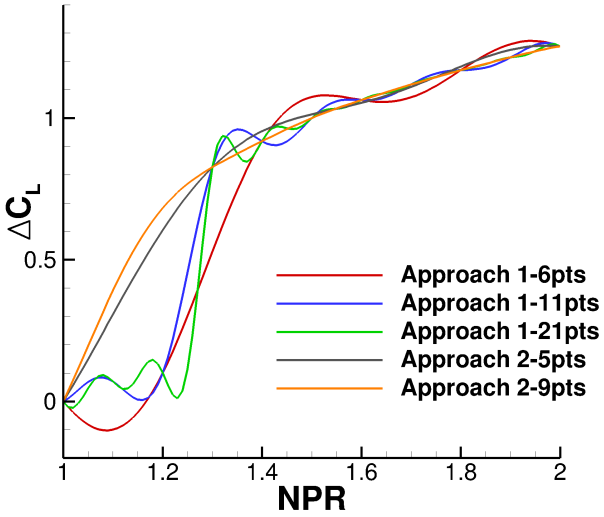

Figure 5.2: Lift coefficient vs. NPR interpolated using kriging for different numbers of points.

The result of these two approaches can be seen in Fig. 5.2. Including points within the separated region, the first approach, produces an oscillatory relationship between lift and NPR. Even using an interval of only 0.05, with 21 points, there are still oscillations at the low NPR, between 1.3 and 1.5. In contrast to this, with the second approach we can achieve a smooth representation with only 9 points. Using only 5 points with the second approach still achieves a better result than the first approach with 21 points. However, there are some oscillations at the low NPR. Therefore, no points should be included in the parameter region where the jet is separated.

5.1.2 Decoupling Nozzle Pressure Ratio from Angle of Attack

To investigate the effects of decoupling the NPR from the AoA within the tables two ROMs are constructed. A single table depending on both the angle of attack and the NPR, [α, NPR] and two tables depending on [α] and [NPR]. From the previous work done in preparation for the modifications made to the SACCON and in understanding the behaviour of the jet several points have already been calculated. Therefore all the points that have already been calculated will be used in the construction of the aerodynamic tables.

The lift, drag and pitching moment coefficients for the coupled model can be seen in Figs. 5.3a, 5.3b and 5.3c, respectively, the points correspond to the discrete entries that were calculated using CFD. There are very few discrete entries at the high angles of attack with increasing NPR due to the fact that the flow becomes highly separated in those regions causing significant unsteadiness in the loads. In this region the interpolation method is predicting a decrease in the drag coefficient which seems unrealistic. The highly separated flow on the upper surface of the aerofoil at the high angles of attack will cause a large increase in the drag coefficient.

Previous unsteady results involving harmonic oscillations of the AoA will be used to evaluate the performance of the tabular methods. The case used for evaluation involves oscillations between 0° and 10° at a reduced frequency of 0.052 with a constant NPR of 1.5. A comparison of the integrated loads computed using the time-accurate CFD simulations and the two ROMs can be seen in Fig. 5.4. As can be seen from all three coefficients the effectiveness of the coanda jet depends significantly on the AoA. The decoupled model overpredicts the lift coefficient and underpredicts the drag and pitching moment coefficients relative to the coupled model and the discrepancy increases for higher angles of attack. This is because as the AoA is increased, the pressure at the slot exit increases causing a decrease in the speed of the jet. As a result of this, the trailing edge separation point moves downstream causing the differences in the prediction of the two models. The lift in the CFD solutions dips as the AoA approaches its peak,

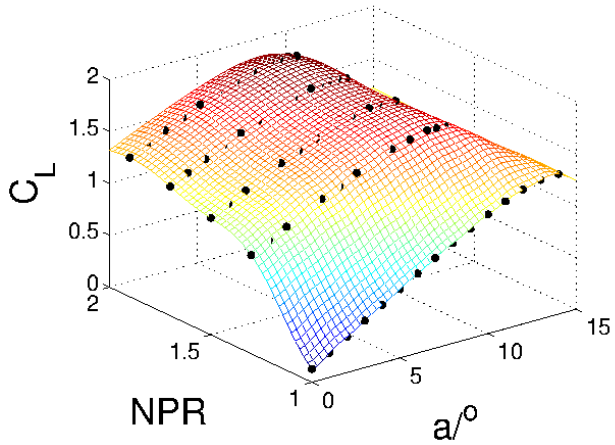

(a) Lift coefficient.

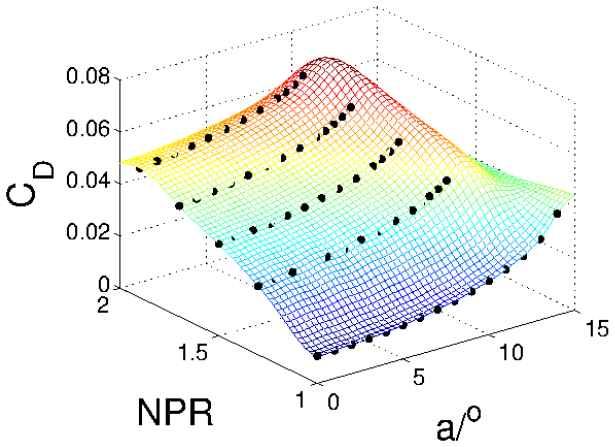

(b) Drag coefficient.

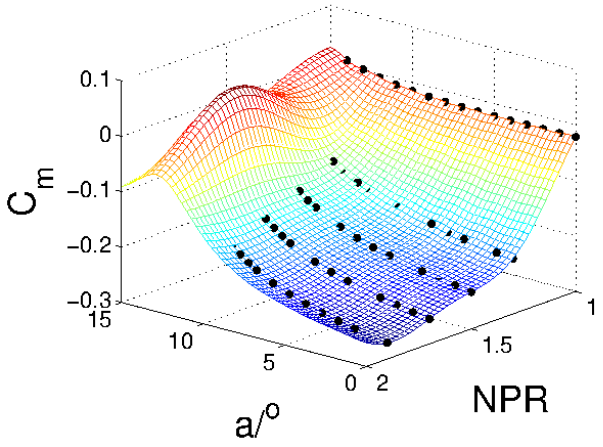

(c) Pitching moment coefficient.

Figure 5.3: The aerodynamic coefficients and the damping derivatives at a Mach Number of 0.2. The points correspond to the discrete entries determined using CFD.

as the aerofoil is about to stall. This suggests the onset of stall is delayed slightly by the ramping up motion. However, this is completely missed by the decoupled model. The coupled model predicts the lift flattening out as it cannot capture unsteady effects such as these. The stall angle decreases with increasing NPR and by decoupling the NPR and AoA this effect is lost.

Overall the coupled model captures the lift and pitching moment coefficients well with some minor discrepancies. There is some slight hysteresis in the pitching moment coefficient. As the AoA oscillates the

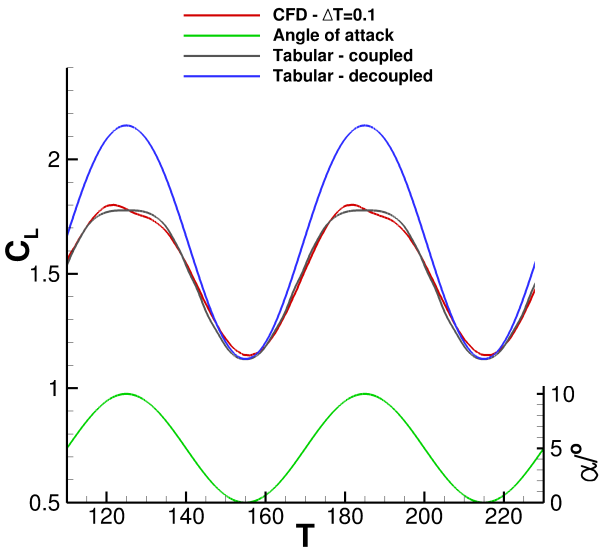

(a) Lift coefficient.

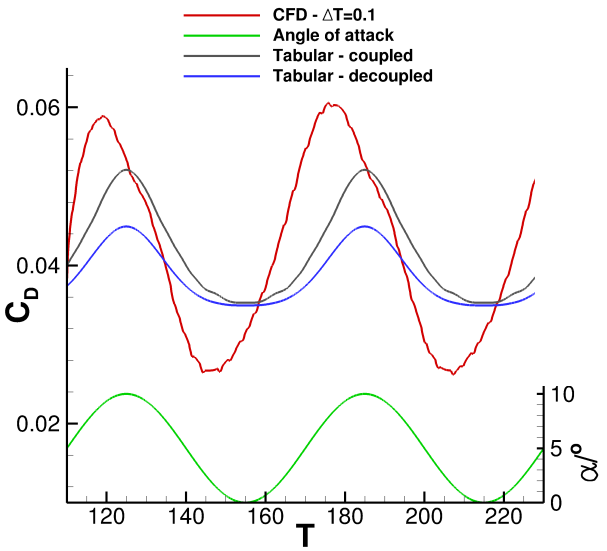

(b) Drag coefficient.

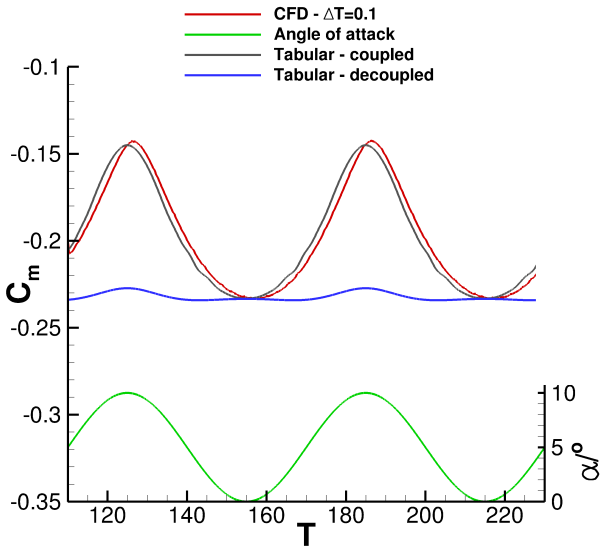

(c) Pitching moment coefficient.

Figure 5.4: Comparison of the aerodynamic loads predicted by CFD and by tabular methods for sinusoidal oscillations of the AoA between 0° and 10° at a reduced frequency of 0.052 with a NPR of 1.5.

rear separation point oscillates due to the fluctuations in the jet speed. The leading edge stagnation point also moves as a result of the change in AoA. The flow response to the movement of the separation point is slower than the flow response to the change in the angle of attack. This causes the slight discrepancies that can be seen in Fig. 5.4c. The drag is quite poorly predicted, Fig. 5.4b, underprediction of the

maximum drag and overprediction of the minimum drag. There is also significant evidence of hysteresis in the drag coefficient. Again this occurs as a result of the fluctuations in the jet speed which lead to oscillations of the leading edge and trailing edge stagnation points. However as the drag depends primarily on the pressure around the leading and trailing edges the effects of the varying jet speed and stagnation point are more noticeable.

5.1.3 Inclusion of Stability Derivatives

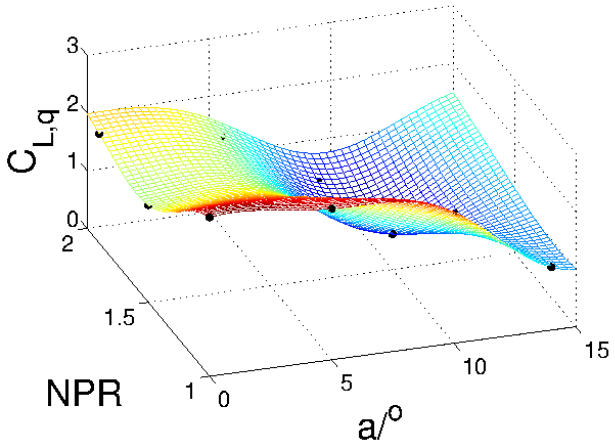

(a) Lift damping derivative.

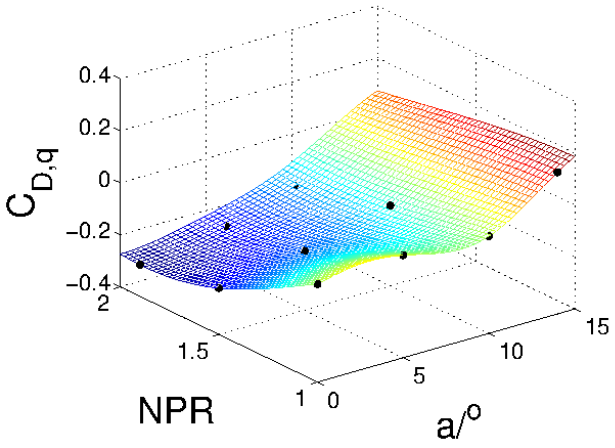

(b) Drag damping derivative.

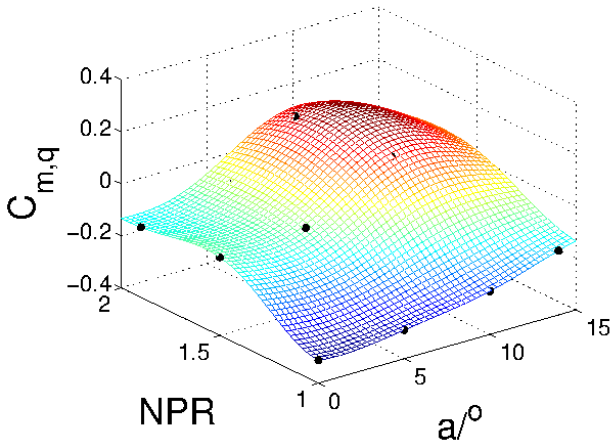

(c) Pitch damping derivative.

Figure 5.5: The aerodynamic coefficients and the damping derivatives at a Mach Number of 0.2. The points correspond to the discrete entries determined using CFD.

For the inclusion of quasi-steady effects, additional tables, [α,NPR], are constructed containing the stability derivatives. The tables containing these are plotted in Fig. 5.5.

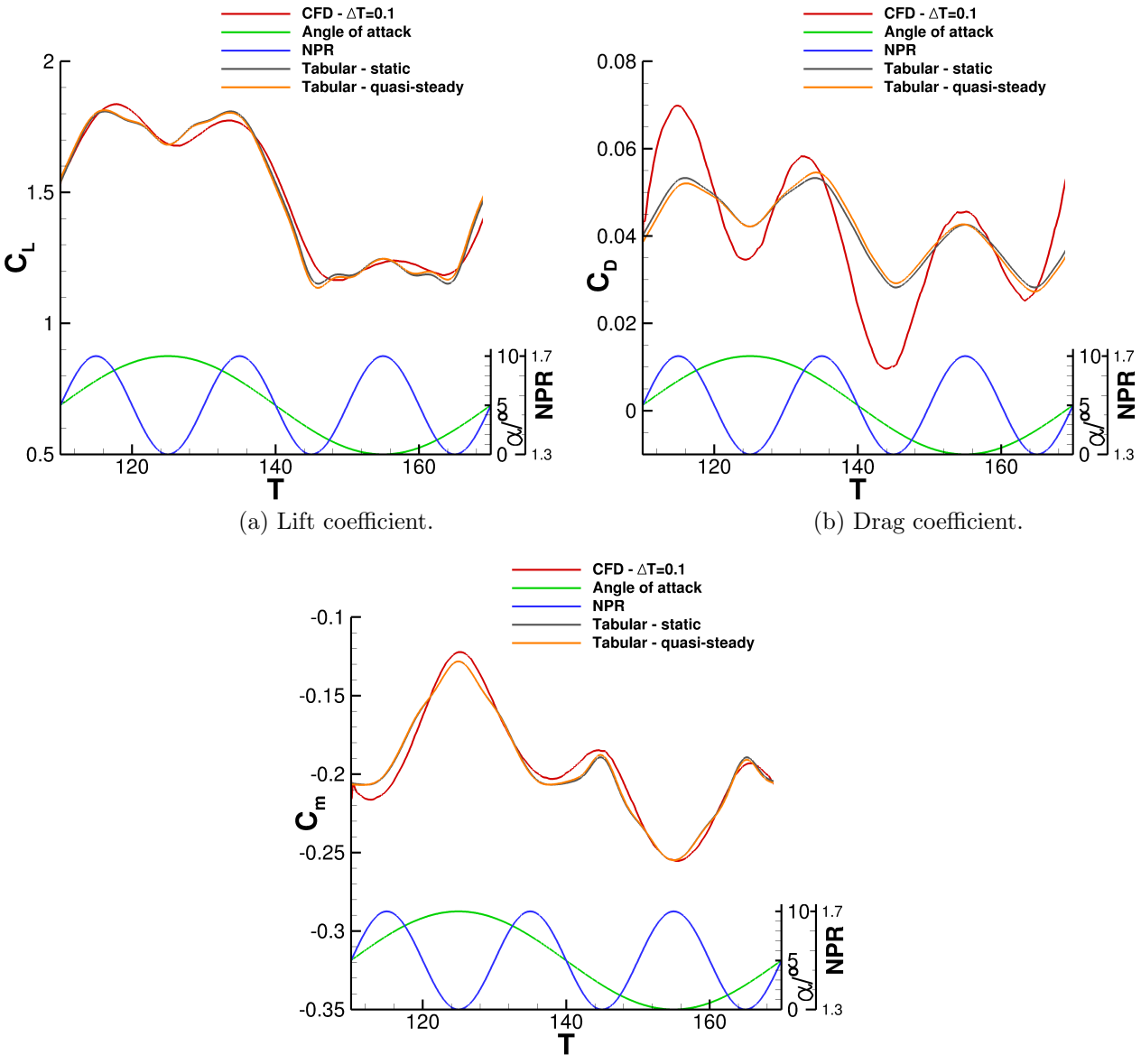

(a) Lift coefficient.

(b) Drag coefficient.

(c) Pitching moment coefficient.

Figure 5.6: Comparison of the aerodynamic loads predicted by CFD and by tabular methods for sinusoidal oscillations of the NPR between 1.3 and 1.7 at a reduced frequency of 0.157 and sinusoidal oscillations of the AoA between between 0° and 10° at a reduced frequency of 0.052.

The case used to demonstrate the effects of the inclusion of stability derivatives is shown in Fig.

5.6. This case involves oscillations of both the angle of attack and the NPR. The effects of the stability derivatives on the lift and pitching moment coefficient are barely noticeable, Figs. 5.6a and 5.6c. For the drag coefficient they are slightly larger, but still only approximately 5% of the static contribution during the peak pitching rate, Fig. 5.6b. This case also demonstrates that the hysteresis exhibited by the jet cannot be captured by these types of methods. If we look at the lift coefficient, Fig. 5.6a, we see that the tabular methods predicts a small oscillations around the maximum and minimum angles of attack which are identical in value. In the CFD solution, the first maxima occurs as the NPR is being decreased and has a lift of 1.84 while for the second the NPR is being increased and the lift is 1.77.

5.2 Summary and Conclusions

Tabular methods have been used to predict the aerodynamic loads throughout harmonic oscillations of the modified aerofoil taken from the root of the SACCON's wing. The effects of decoupling the NPR and AoA were investigated and shown to be of great importance. The NPR affects the stall angle of the aerofoil and the AoA affects the perfomance of the coanda jet. This causes significant discrepancies in both the attached regime of flow and at high angles of attack where the onset of flow separation causes plateauing of the lift. The stability derivatives had very little effect on the predictions of the lift and pitching moment coefficients for a reduced frequency of 0.057. Their effect on the drag coefficient was more noticeable however still negligible when considering the static contribution. Therefore they are not required except for very agile manoeuvres, especially as the computational cost of constructing the tables for the damping derivatives is significantly higher than the static part.

Overall the prediction of the lift and pitching moment coefficients is reasonable for the attached regime of the flow. The hysteresis is less noticeable in these two coefficients and the tabular methods capture the overall trend and actual value quite well. However for the drag coefficient the effect of changes in the jet speed, as a result of either the change in the NPR or AoA, is initially quite drastic and it takes a while for the flow to adjust. The change in pressure occurs initially at the slot causing a shift first in the

rear stagnation point then in the leading edge stagnation point. This leads to the large oscillations in the drag which cannot be captured by the tabular methods, as these are the equivalent of both stagnation points adjusting to the changes in the NPR at the same time.

5.3 Tabular Method for the SACCON with CC

The large number of iterations required for convergence, approximately five times more relative to the SACCON with flaps, and large grids make generating a look-up table for the SACCON with CC prohibitively expensive. Some potential changes and their implications on using a tabular method to predict the unsteady aerodynamics are discussed.

During the construction of the two dimensional flight mechanics model for the circulation control aerofoil it was observed that the effects of the coanda jet depend significantly on the angle of attack. This occurs because the speed of the subsonic jet is affected by the changes in the pressure around the slot as a result of the change in the angle of attack. For these devices to be successfully used as manoeuvre effectors they will also be required to perform in the transonic regime, requiring a supersonic jet to entrain the freestream flow. Achieving circulation control with the use of supersonic coanda jets is being investigated [62, 63] ; with the main aspects being related to nozzle contouring and trailing edge geometry optimisation. The main point of this is that with correct nozzle design the pressure at the slot exit will be fixed, so there should be no variation in the blowing coefficient with respect to changes in the angle of attack. This will make it possible to use the blowing coefficient as the control parameter, which is more suitable relative to the NPR as the dependency on the freestream Mach number is included.

A second issue is that the final design of an aircraft employing circulation control is still unclear. The CFD results from chapter 4.7 suggest that the yawing moment occurs almost purely as a result of the momentum ejected at the low blowing coefficients. At high blowing coefficients the vortices created from the strong shear layer between the jet and freestream flow, which create a suction force behind the wing reducing the efficiency of the operation. Therefore, increasing the number of slots and leaving

gaps in between may also increase the efficiency for higher blowing rates as the vortices will likely be smaller and be given an opportunity to breakdown. Also, having slots nearer the wing tip could increase the moment arm increasing the performance of the operation. As the flow over the wings is unaffected by using both upper and lower jets simultaneously, one would expect that the load increment can be determined by linear combinations of each slot using an equation similar to equation 4.1 for each of the slots. The increments to the other loads were either negligible except where the vortex interaction becomes significant; lift, rolling and pitching moment, or depend linearly on the blowing coefficient in a similar fashion to the yawing moment; drag and side force. At low Mach numbers the CC is able to trim sideslip angles of 10° at relatively low blowing coefficients. Therefore, the CFD is only needed to ensure there are no interference effects at high angles of attack or at high blowing coefficients, otherwise, the loads can be predicted using equations like equation 4.1.

The rolling moment operation presents more of a challenge to incorporate into a flight mechanics model. Ideally, control engineers would like to be able to completely decouple the roll and yaw moment operations. Alternatively, a small positive coupling is also acceptable, i.e. $\frac{dC_l}{dC_n} > 0$. This is because when an aircraft is attempting to turn it will roll and yaw in the same direction and pitch up. The controls are then used to maintain a new trim state with the appropriate (α, β, ϕ) while the turn is performed. Secondly the investigation of the rolling moment operation was restricted to anti-symmetrical operations, using the same NPR on both wings. Using a different NPR on each wing can increase the drag for one of the wings to simultaneously create a yawing moment. The number of slots and size of the gap between them also plays a crucial role for this operation. As long as the gap between the slots is large enough so that the vortex travelling along the lower surface can merge with the freestream and dissipate, it may be possible to obtain the total load increment by linear combinations of each of the slots. However, the results suggest that increasing the number of slots increases the efficiency of this operation. For each additional slot an additional table is also required, assuming there are no interference effects between the slots. This is because the change in wing thickness and camber effect the performance of the CC

resulting in a different $\frac{\Delta C_l}{\Delta C_\mu}$ for each slot. Also as we have seen from the static SACCON results, the performance depends significantly on the angle of attack. Therefore, the control parameters for each of the slots would have to be coupled with the angle of attack.

Chapter 6

Conclusions

CFD has been used to evaluate the efficacy of using circulation control as a manoeuvre effector for unmanned aircraft and to evaluate the performance of tabular methods for predicting the unsteady aerodynamics. Two validation cases have been simulated to assess the adequacy of CFD methods to predict the performance of circulation control aerofoils and unmanned aircraft. The CC-E0020EJ test case demonstrated that the PMB code can predict the separation point of the coanda jet and pressure distribution over the coanda surface with accuracy. There were discrepancies between the two turbulence models tested, the Wilcox k-ω model and Menter's SST model. Menter's SST model predicted a lower ratio of turbulent eddy viscosity to molecular viscosity in the shear layer between the jet and the freestream flow and as a result overpredicted the location of the separation point. There are a few discrepancies with regards to the experimental results such as the location of the leading edge stagnation point and the strength of the suction peak. However, wind tunnel wall effects and angle of attack corrections account for these discrepancies. For the SACCON slight discrepancies with both the loads and surface pressures occur at the low angles of attack. However these have been shown, in other work, to be caused by not modelling the sting and the wind tunnel walls in the CFD simulations. In the non-linear regime of the flow the RANS methods fail to capture the behaviour of the vortices accurately. Higher fidelity turbulence modelling and use of the URANS equations can improve the agreement at the high angles of attack. However, for the purpose of predicting the integrated loads the increase in computational cost is

not worth the increase in accuracy, especially with regards to generating a tabular model.

A 2D study to determine the sizing of the CC device has been performed on an aerofoil section taken from the root of the SACCON's wing. A coanda radius of 0.5% of the chord has been shown to be able to provide similar lift augmentation to a blended flap at a 20° deflection. Both methods have similar effects on the aerodynamic loads across the angle of attack range with some slight differences. The flap generates less drag at the low angles of attack, however the flow separates behind the flap at about 4° creating more drag than the CC at the high angles of attack. Unsteady simulations were also performed using this aerofoil section to determine if manoeuvres may interfere with the performance of the jet. Two key issues were identified from these results. Firstly, if the jet separates and the NPR is increased it does not reattach, suggesting it would have to be turrned off and then turned back on for attachment to occur. Secondly, that when the aerofoil goes into deep stall the recirculation zone behind the aerofoil entrains the coanda jet causing it to separate and does not reattach as the aerofoil recovers from stall.

Modifications were made to the SACCON UCAV to replace the conventional control surfaces with the CC device. This included truncating the wing to obtain the required trailing edge thickness and altering the trailing edge of the body to match the geometry of the coanda surface. Two configurations were constructed one with a single upper and lower slot along each wing and the other with three slots of equal width. Operations to generate a yawing moment, using both upper and lower slots on one wing simultaneously, and a rolling moment, using the upper slot on one wing and the lower slot on the other, were investigated. It was shown that at low blowing coefficients the performance of the yawing moment operation could be predicted by assuming it was generated purely as a result of the momentum ejected from the slot. It was also able to perform at high angles of attack with no reduction in performance. The rolling moment operation was able to generate similar rolling moments to conventional control surfaces at low angles of attack where the flow is attached. However, at high angles of attack where flow separation occurs at the trailing edge the CC becomes completely ineffective as it relies upon the upper surface to generate the rolling moment. The key difference between the single slot and three slot configurations is in

the size of the vortex travelling over the surface opposite the active jet. Leaving a gap between the slots allows this vortex to travel in the direction of the freestream flow and dissipate. This and the increased number of sections where there is a spillover effect increase the efficiency of the CC.

A tabular model was generated for the aerofoil section used in the 2D study to investigate the effects of decoupling the NPR and AoA parameters within the tables. The performance of the jet depends significantly on the AoA as the pressure around the slot increases causing a decrease in the speed of the jet. Also, the stall angle decreases as the NPR is increased. Therefore, these two parameters must be coupled for accurate prediction of the integrated loads. Overall the model was able to predict the lift and pitching moment coefficients accurately. However, there was significant hysteresis in the drag coefficient which these type of models are unable to predict. A discussion of how a flight mechanics model could be constructed for the full SACCON was conducted. Also, the implication possible future design improvements could have on generating a tabular model and its efficacy for such applications was considered.

There are a few areas on which future work could be performed on CC and related flow control devices. The first step would be to obtain a better understanding of the changes in the effectiveness of the CC as a result of geometric changes. This could involve parametric studies and optimisation to determine the ideal geometry (coanda surface, aerofoil section, sweep angle etc.), the number, size and location of the slots and the sizing of the gaps. There is also interest in using similar methods at the leading edge of the wing to delay flow separation until higher angles of attack. This could potentially extend the operational envelope of the CC and there would likely be coupling effects between the leading and trailing edge devices which would need to be investigated.

Another area which needs further exploration is the unsteady performance of the coanda jet. The results from chapter 4 show that the potential for the jet to separate exists. This occured outside the flight envelope for the particular case, however, the behaviour needs to be fully understood before the CC devices can be used on aircraft as manoeuvre effectors. The potential for jet separation also needs to be

investigated for three dimensional geometries. There could be significant differences in the mechanisms that cause the jet to separate as it seems to depend on the flow topology around the trailing edge.

The operations that were investigated in this thesis were limited to symmetric and anti-symmetric operations for yaw and roll control. This could be extended to search for particular combinations of active slots with independently chosen NPRs which generate moments around only one of the axes. These types of operations would make it possible to completely decouple control about the pitch, roll and yaw axes.

Lastly, the construction of reduced order models for predicting unsteady manoeuvres and stability and control characteristics need further examination. Depending on the number of slots and the coupling effects between them this could present a significant challenge in generating a lookup table. The different slots will have different values for $\frac{\Delta C_l}{\Delta C_\mu}$, $\frac{\Delta C_m}{\Delta C_\mu}$ and $\frac{\Delta C_n}{\Delta C_\mu}$ depending on the geometry and the AoA. The work from chapter 5 demonstrates that the coupling effects between the NPR and the AoA are significant and need to be taken into account for accurate prediction of the integrated loads. Assuming there are no coupling effects between the slot this would only increase the number of tables required causing a linear increase in the number of calculations required to generate the ROM. However, any coupling effects would increase the dimension of each table causing an increase in the order of magnitude of the required calculations needed to generate the ROM. Once these interactions and effects have been understood it would be possible to generate a ROM to predict the stability and control characteristics of an aircraft employing CC. This would then allow a complete comparison against conventional control surfaces to determine whether they are a viable replacement for them.

Bibliography

[1] SC Asbury and FJ Capone. High-Alpha Vectoring Characteristics of the F-18/HARV. *Journal of Propulsion and Power*, 10(1):116–121, 1994.

[2] C Henri. Device for Deflecting a Stream of Elastic Fluid Projected into an Elastic Fluid, September 1 1936. US Patent 2,052,869.

[3] KA Deere. Summary of Fluidic Thrust Vecotring Research Conducted at NASA Langley Research Center. In *The 21st AIAA Applied Aerodynamics Conference, Orlando, Florida*, 23-26 June, 2003.

[4] KA Deere, BL Berrier, JD Flamm, and SK Johnson. Computational Stuy of Fluidic Thrust Vectoring Using Separation Control in a Nozzle. In *The 21st Applied Aerodynamics Conference, Orlando, Florida*, 23-26 June, 2003.

[5] KA Deere. PAB3D Simulations of a Nozzle with Fluidic Injection for Yaw Thrust-Vector Control. In *34th AIAA/ASME/SAE/ASEE Joint Propulsion Conference & Exhibit, Cleveland, Ohio*, 13-15 July, 1998.

[6] KA Deere, BL Berrier, and JD Flamm. A Computational Study of a New Dual Throat Fluidic Thrust Vectoring Nozzle Concept. In *41st AIAA/ASME/SAE/ASEE Joint Propulsion Conference & Exhibit, Tucson, Arizona*, 10-13 July, 2005.

[7] JD Flamm, KA Deere, ML Mason, BL Berrier, and SK Johnson. Experimental Study of an Axisymmetric Dual Throat Fluidic Thrust Vectoring Nozzle for Supersonic Aircraft Application. In

43rd AIAA/ASME/SAE/ASEE Joint Propulsion Conference & Exhibit, Cincinnati, Ohio, 8-11 July, 2007.

[8] KA Deere, JD Flamm, BL Berrier, and SK Johnson. Computational Study of an Axisymmetric Dual Throat Fluidic Thrust Vectoring Nozzle for a Supersonic Aircraft Application. In *43rd AIAA/ASME/SAE/ASEE Joint Propulsion Conference & Exhibit, Cincinnati, Ohio*, 8-11 July, 2007.

[9] CS Shin, HD Kim, T Setoguchi, and S Matsuo. A Computational Study of Thrust Vectoring Control Using Dual Throat Nozzle. *Journal of Thermal Science*, 19(6):486–490, 2010.

[10] DJ Wing and VJ Giuliano. Fluidic Thrust Vectoring of an Axisymmetric Exhaust Nozzle at Static Conditions. In *1997 ASME Fluids Engineering Division Summer Meeting*, 1997.

[11] E Mohammadi and A Toloei. Analysis of Dual Secondary Injection for Thrust Vectoring. *Aircraft Engineering and Aerospace Technology*, 83:213–220, 2011.

[12] KA Deere. Computational Investigation of the Aerodyamic Effects on Fluidic Thrust Vectoring. In *36th AIAA/ASME/SAE/ASEE Joint Propulsion Conference & Exhibit, Las Vegas, Nevada*, 2000.

[13] JD Flamm. Experimental Study of a Nozzle Using Fluidic Counterflow for Thrust Vectoring. In *34th AIAA/ASME/SAE/ASEE Joint Propulsion Conference & Exhibit, Cleveland, Ohio*, 13-15 July, 1998.

[14] CA Hunter and KA Deere. Computational Investigation of Fluidic Counterflow Thrust Vectoring. In *35th AIAA/ASME/SAE/ASEE Joint Propulsion Conference & Exhibit, Los Angeles, California*, 20-23 June, 1999.

[15] MS Mason and WJ Crowther. Fluidic Thrust Vecotring of Low Observable Aircraft. In *CEAS Aerospace Aerodynamic Research Conference*, 10-12 June, 2002.

[16] JP Fielding, CP Lawson, R Pire, and G Monterzino. Development of the Demon Technology Demonstrator UAV. In *27th International Congress of the Aeronautical Sciences, Nice, France*, 19-24 September, 2010.

[17] A Buonanno, D Drikakis, C Papachristou, A Savvaris, C Vamvakoulas, and C Warsop. Computational Investigation of the DEMON Unmanned Air Vehicle Thrust Vectoring System. *Proceedings of the Institution of Mechanical Engineers, Part G: Journal of Aerospace Engineering*, 224(4):387–394, 2010.

[18] P Jiang, Z Wang, and I Gursul. Effects of Unsteady Trailing-Edge Blowing on Delta Wing Aerodynamics. *Journal of Aircraft*, 47(2):591–602, 2010.

[19] Z Wang, P Jiang, and I Gursul. Effects of Thrust-Vectoring of Delta Wing Aerodynamics. *Journal of Aircraft*, 44(6):1877–1888, 2007.

[20] RJ Englar. Circulation Control for High Lift and Drag Generation on STOL Aircraft. *Journal of Aircraft*, 12(5):457–463, 1975.

[21] RJ Englar. Design of the Circulation Control Wind STOL Demonstrator Aircraft. *Journal of Aircraft*, 18(1):51–58, 1981.

[22] JL Loth and JB Fanucci. Flight Performance of a Circulation Controlled STOL Aircraft. *Journal of Aircraft*, 13(3):169–173, 1976.

[23] RJ Englar. Development of the A-6/Circulation Control Wing Flight Demonstrator Configuration. Technical report, (No. DTNSRDC/ASED-79/01) David W Taylor Naval Ship Research and Development Center, Bethesda MD Aviation and Surface Effects Department., 1979.

[24] JL Loth and M Boasson. Circulation Controlled STOL Wing Optimisation. *Journal of Aircraft*, 21(2):128–134, 1984.

[25] GS Jones, SA Viken, AE Washburn, LN Jenkins, and CM Cagle. An Active Flow Circulation Controlled Flap Concept for General Aviation Aircraft Applications. In *1st Flow Control Conference, St. Louis, Missouri*, 24-26 June, 2002.

[26] CM Cagle and GS Jones. A Wind Tunnel Model to Explore Unsteady Circulation Control for General Aviation Applications. In *The 22nd AIAA Applied Aerodynamics Conference, St. Louis, Missouri*, 24-26 June, 2002.

[27] RC Swanson and CL Rumsey. Numerical Issues for Circulation Control Calculations. In *3rd AIAA Flow Control Conference, San Francisco, California*, 5-8 June, 2006.

[28] WJ Crowther. Towards Integrated Design of Fluidic Flight Controls for a Flapless Aircraft. *The Aeronautical Journal*, 113(1149):699–713, 2009.

[29] MV Cook, A Buonanno, and SD Erbsloh. A Circulation Control Actuator for Flapless Flight Control. *The Aeronautical Journal*, 112(1134):483–489, 2008.

[30] PIA Wilde, WJ Crowther, and CD Harley. Application of Circulation Control for Three-Axis Control of a Tailless Flight Vehicle. *Proceedings of the Institution of Mechanical Engineers, Part G: Journal of Aerospace Engineering*, 224(4):373–386, 2010.

[31] GS Jones, JC Lin, BG Allan, WE Milholen, CL Rumsey, and RC Swanson. Overview of CFD Validation Experiments for Circulation Control Applications at NASA. In *2008 International Powered Lift Conference, London, United Kingdom*, 22-24 July, 2008.

[32] GS Jones and RD Joslin. Proceedings of the 2004 NASA/ONR Circulation Control Workshop, 16-17 March, 2004.

[33] BG Allan, GS Jones, and JC Lin. Reynolds-Average Navier-Stokes Simulation of a 2D Circulation Control Wind Tunnel Experiment. *AIAA Paper*, 25:2011, 2011.

[34] CL Rumsey and T Nishino. Numerical Study Comparing RANS and LES Approaches on a Circulation Control Airfoil. *International Journal of Heat and Fluid Flow*, 32(5):847–864, 2011.

[35] RJ Englar, GS Jones, BG Allan, and JC Lin. 2-D Circulation Control Airfoil Benchmark Experiments Intended for CFD Code Validation. In *47th AIAA Aerospace Sciences Meeting Including The New Horizons Forum and Aerospace Exposition, Orlando, Florida*, 5-8 January, 2009.

[36] KB Paschal, D Neuhart, G Beeler, and BG Allan. Circulation Control Model Experimental Database for CFD Validation. In *50th AIAA Aerospace Sciences Meeting, Nashville, Tennessee*, 9-12 January, 2012.

[37] T Nishino, S Hahn, and K Shariff. Large-Eddy Simulations of a Turbulent Coanda Jet on a Circulation Control Airfoil. *Physics of Fluids*, 22(12):125105, 2010.

[38] NJ Wood. Section Characteristics of a Finite, Swept Circulation Control Airfoil. *Journal of Aircraft*, 24(1):38–44, 1987.

[39] KJ Badcock, BE Richards, and MA Woodgate. Elements of Computational Fluid Dynamics on Block Structured Grids Using Implicit Solvers. *Progress in Aerospace Sciences*, 36(5):351–392, 2000.

[40] GN Barakos. *Study of Unsteady Aerodynamic Phenomena Using Advanced Turbulence Closures*. PhD thesis, University of Manchester Institute of Science and Technolody, 1999.

[41] DC Wilcox. *Turbulence Modelling for CFD*. DCW industries La Canada, CA, 1998.

[42] FJ Brandsma, A Elsenaar, and JC Kok. Leading Edge Vortex Flow Computations and Comparisons with DNW-HST Wind Tunnel Data. Technical report, NATO Research and Technology Organization Neuilly-Sur-Seine (France), 2003.

[43] FR Menter. Two-Equation Eddy-Viscosity Turbulence Models for Engineering Applications. *AIAA journal*, 32(8):1598–1605, 1994.

[44] A Jameson. Time Dependent Calculations Using Multigrid, with Applications to Unsteady Flows Past Airfoils and Wings. In *AIAA 10th Computational Fluid Dynamics Conference, Honolulu, Hawai*, 24-26 June, 1991.

[45] RM Cummings and A Schutte. An Integrated Computational/Experimental Approach to UCAV Stability & Control Estimation: Overview of NATO RTO AVT-161. In *28th AIAA Applied Aerodynamics Conference, Chicago, Illinois*, 28 June - 1 July, 2010.

[46] TD Loeser and DD Vicroy. SACCON Static Wind Tunnel Tests at DNW-NWB and 14'x22' NASA LaRC. In *28th AIAA Applied Aerodynamics Conference, Chicago, Illinois*, 28 June - 1 July, 2010.

[47] DD Vicroy and TD Loeser. SACCON Forced Oscillation Tests at DNW-NWB and NASA Langley 14x22-foot Tunnel. In *28th AIAA Applied Aerodynamics Conference, Chicago, Illinois*, 28 June - 1 July, 2010.

[48] A Gilliot and S Morgand. Static and Dynamic SACCON PIV tests Part i: Forward Flowfield. In *28th AIAA Applied Aerodynamics Conference, Chicago, Illinois*, 28 June - 1 July, 2010.

[49] R Konrath, EWM Roosenboom, A Schroder, D Pallek, and D Otter. Static and Dynamic SACCON PIV Tests Part ii: Aft Flow Field. In *28th AIAA Applied Aerodynamics Conference, Chicago, Illinois*, 28 June - 1 July, 2010.

[50] D Vallespin, A Da Ronch, and KJ Badcock. Validation of Vortical Flow Predictions for a UCAV Wind Tunnel Model. In *28th AIAA Applied Aerodynamics Conference, Chicago, Illinois*, 28 June - 1 July, 2010.

[51] A Jirásek and RM Cummings. SACCON Static and Dynamic Motion Flow Physics Simulations Using COBALT. In *29th AIAA Applied Aerodynamics Conference, Honolulu, Hawaii*, 27-30 June, 2010.

[52] RM Cummings and A Schutte. The NATO STO Task Group AVT-201 on 'Extended Assessment of Stability and Control Prediction Methods for NATO Air Vehicles'. In *32nd AIAA Applied Aerodynamics Conference, Atlanta, Georgia*, 16-20 June, 2014.

[53] KC Huber, DD Vicroy, A Schutte, and A Huebner. UCAV Model Design and Static Experimental Investigations to Estimate Control Device Effectiveness and S&C Capabilities. In *32nd AIAA Applied Aerodynamics Conference, Atlanta, Georgia*, 2014.

[54] AM Rampurawala. *Aeroelastic Analysis of Aircraft with Control Surfaces Using CFD*. PhD thesis, University of Glasgow, 2006.

[55] DJ Kennett, G Hoholis, and KJ Badcock. Numerical Simulation of Control Surface Deflections over a Generic UCAV configuration at Off-design Flow Conditions. In *32nd AIAA Applied Aerodynamics Conference, Atlanta, Georgia*, 16-20 June, 2014.

[56] D Vallespin. *Development of a Process and Toolset to Study UCAV Flight Mechanics using Computational Fluid Dynamics*. PhD thesis, University of Liverpool, 2011.

[57] J Jeong and F Hussain. On the Identification of a Vortex. *Journal of Fluid Mechanics*, 285:69–94, 1995.

[58] SN Michie. *A Design Methodology for Circulation Control Manoeuvre Effectors*. PhD thesis, University of Manchester, 2008.

[59] SN Lophaven, HB Nielsen, and J Søndergaard. DACE-A Matlab Kriging toolbox, version 2.0. Technical report, 2002.

[60] A Da Ronch, AJ McCracken, KJ Badcock, M Widhalm, and MS Campobasso. Linear Frequency Domain and Harmonic Balance Predictions of Dynamic Derivatives. *Journal of Aircraft*, 50(3):694–707, 2013.

[61] AJ McCracken, DJ Kennett, KJ Badcock, and A Da Ronch. Assessment of Tabular Models Using CFD. In *AIAA Atmospheric Flight Mechanics Conference, Boston, Massachusetts*, 19-22 August, 2013.

[62] M Forster, M Biava, and R Steijl. Optimisation of Coanda Surfaces for Transonic Circulation Control. In *6th European Conference for Aerospace Sciences, Krakow, Poland*, 29 June - 3 July, 2015.

[63] M Forster and R Steijl. Numerical Study of Transonic Circulation Control. In *53rd AIAA Aerospace Sciences Meeting, Kissimmee, Florida*, 5-9 January, 2014.